

AFRL-IF-RS-TR-2002-241
Final Technical Report
September 2002



POLYMEMS ACTUATOR: A POLYMER-BASED MICROELECTROMECHANICAL (MEMS) ACTUATOR WITH MACROSCOPIC ACTION

Honeywell International, Incorporated

Sponsored by
Defense Advanced Research Projects Agency
DARPA Order No. E117

APPROVED FOR PUBLIC RELEASE; DISTRIBUTION UNLIMITED.

The views and conclusions contained in this document are those of the authors and should not be interpreted as necessarily representing the official policies, either expressed or implied, of the Defense Advanced Research Projects Agency or the U.S. Government.

AIR FORCE RESEARCH LABORATORY
INFORMATION DIRECTORATE
ROME RESEARCH SITE
ROME, NEW YORK

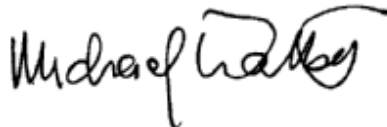
This report has been reviewed by the Air Force Research Laboratory, Information Directorate, Public Affairs Office (IFOIPA) and is releasable to the National Technical Information Service (NTIS). At NTIS it will be releasable to the general public, including foreign nations.

AFRL-IF-RS-TR-2002-241 has been reviewed and is approved for publication

APPROVED:

A handwritten signature in black ink, appearing to read "Duane Gilmour". The signature is fluid and cursive, with the first name "Duane" being more prominent than the last name "Gilmour".

DUANE GILMOUR
Project Engineer

A handwritten signature in black ink, appearing to read "Michael L. Talbert". The signature is fluid and cursive, with the first name "Michael" being more prominent than the last name "Talbert".

FOR THE DIRECTOR:

MICHAEL L. TALBERT, Maj., USAF
Technical Advisor, Information Technology Division
Information Directorate

REPORT DOCUMENTATION PAGE			<i>Form Approved</i> <i>OMB No. 074-0188</i>	
Public reporting burden for this collection of information is estimated to average 1 hour per response, including the time for reviewing instructions, searching existing data sources, gathering and maintaining the data needed, and completing and reviewing this collection of information. Send comments regarding this burden estimate or any other aspect of this collection of information, including suggestions for reducing this burden to Washington Headquarters Services, Directorate for Information Operations and Reports, 1215 Jefferson Davis Highway, Suite 1204, Arlington, VA 22202-4302, and to the Office of Management and Budget, Paperwork Reduction Project (0704-0188), Washington, DC 20503				
1. AGENCY USE ONLY (Leave blank)		2. REPORT DATE SEPTEMBER 2002	3. REPORT TYPE AND DATES COVERED Final Jul 98 – May 02	
4. TITLE AND SUBTITLE POLYMEMS ACTUATOR: A POLYMER-BASED MICROELECTROMECHANICAL (MEMS) ACTUATOR WITH MACROSCOPIC ACTION			5. FUNDING NUMBERS C - F30602-98-C-0217 PE - 63739E PR - E117 TA - 00 WU - 39	
6. AUTHOR(S) Robert Horning				
7. PERFORMING ORGANIZATION NAME(S) AND ADDRESS(ES) Honeywell International, Incorporated 12001 State Highway 55 Plymouth MN 55441			8. PERFORMING ORGANIZATION REPORT NUMBER	
9. SPONSORING / MONITORING AGENCY NAME(S) AND ADDRESS(ES) Defense Advanced Research Projects Agency AFRL/IFTC 3701 North Fairfax Drive 26 Electronic Parkway Arlington Virginia 22203-1714 Rome New York 13441-4514			10. SPONSORING / MONITORING AGENCY REPORT NUMBER AFRL-IF-RS-TR-2002-241	
11. SUPPLEMENTARY NOTES AFRL Project Engineer: Duane Gilmour/IFTC/(315) 330-3550/ Duane.Gilmour@rl.af.mil				
12a. DISTRIBUTION / AVAILABILITY STATEMENT APPROVED FOR PUBLIC RELEASE; DISTRIBUTION UNLIMITED.				12b. DISTRIBUTION CODE
13. ABSTRACT (Maximum 200 Words) A polymer-based MEMS actuator, consisting of small unit cells in a macroscopic array, was developed and demonstrated. Models were developed which predicted the performance, and actuators were fabricated which matched the theoretical predictions. Deformation due to imperfect assembly resulted in imperfect performance. Further work is required to develop a reliable assembly process. Numerous polymer-based fabrication procedures were developed. Many of them borrow from either silicon or flexible printed circuit manufacturing, but modifications were necessary in order to adapt the processes to MEMS. The actuator is very efficient and uses very little power, making it suitable for autonomous applications such as robots.				
14. SUBJECT TERMS Microelectromechanical, MEMS, Polymers, Actuators, PolyMEMS				15. NUMBER OF PAGES 83
				16. PRICE CODE
17. SECURITY CLASSIFICATION OF REPORT UNCLASSIFIED	18. SECURITY CLASSIFICATION OF THIS PAGE UNCLASSIFIED	19. SECURITY CLASSIFICATION OF ABSTRACT UNCLASSIFIED	20. LIMITATION OF ABSTRACT UL	

Table of Contents

1.0 EXECUTIVE SUMMARY	1
2.0 INTRODUCTION.....	1
3.0 METHODS, ASSUMPTIONS AND PROCEDURES	4
3.1 THE POLYMEMS ACTUATOR CONCEPT	4
3.1.1 <i>Unit Cells and Arrays</i>	<i>4</i>
3.1.2 <i>The Unit Cell Operation</i>	<i>6</i>
3.1.3 <i>The Unit Cell and Array Configuration.....</i>	<i>8</i>
3.2 MODELING	9
3.2.1 <i>Finite Element Modeling</i>	<i>9</i>
3.2.2 <i>The Analytical Model.....</i>	<i>12</i>
3.2.3 <i>Comparison with FEM</i>	<i>17</i>
3.2.4 <i>Comparison of Unit Cell Configurations.....</i>	<i>17</i>
3.2.5 <i>Unit Cell With an Extra Gap</i>	<i>20</i>
3.2.6 <i>Circular Unit Cell.....</i>	<i>23</i>
3.2.7 <i>Linear Unit Cell With a Spring-Like Load</i>	<i>26</i>
3.3 PROCESS DEVELOPMENT AND FABRICATION	30
3.3.1 <i>Process Flow and Requirements</i>	<i>30</i>
3.3.2 <i>Substrate Materials.....</i>	<i>33</i>
3.3.3 <i>Metal, Dielectrics, and Self-Healing</i>	<i>35</i>
3.3.4 <i>Stiction.....</i>	<i>41</i>
3.3.5 <i>Stiction Due to Dielectric Surface Layers</i>	<i>43</i>
3.3.6 <i>Stiction Due to the Substrate</i>	<i>51</i>
3.3.7 <i>Cutting Structures Out of the Substrate.....</i>	<i>54</i>
3.3.8 <i>Assembly and Bonding.....</i>	<i>55</i>
3.3.9 <i>Actuator Characterization</i>	<i>59</i>
4.0 RESULTS AND DISCUSSION.....	60
4.1 1ST AND 2ND GENERATION DEVICES	60
4.2 ACTUATION TEST RESULTS.....	61
4.3 POWER CONSUMPTION	66
4.3.1 <i>Energy and Efficiency.....</i>	<i>66</i>
4.3.2 <i>Power Consumption Estimate.....</i>	<i>69</i>
5.0 CONCLUSIONS.....	70
6.0 RECOMMENDATIONS	71
7.0 PUBLICATIONS.....	74
8.0 PATENTS.....	74

List of Figures

Figure 1. Concept drawings of the PolyMEMS electrostatic actuator unit cell and fully packaged actuator. The stack of metalized polymer sheets and their electrical connections are attached to a circuit board end cap and contained in a flexible hermetically sealed bellows. The mechanical linkage to the load resides on the end cap.	2
Figure 2. Diagrams showing the basic construction and operation of microscopic or mesoscopic unit cells, and the incorporation of multiple unit cells into a 3-D array that is capable of generating a macroscopic force and displacement.	4
Figure 3. Various modes of operation of the PolyMEMS actuator. The array on the left has no voltage applied and is fully extended by an applied load. The extension is a function of the magnitude of the load. The center drawing shows an array that has been fully collapsed by applying a sufficiently high voltage to all layers of the array. The drawing on the right shows an array in which voltage has been applied to only selected layers in the stack.	5
Figure 4. A detailed cross-section of a unit cell.	6
Figure 5. Zipping behavior of the unit cell at pull-in.	7
Figure 6. Possible unit cell configurations. In each case, the metal/dielectric electrodes can be present on all surfaces or only on a subset of the surfaces.	8
Figure 7. FEM results for actuator force per unit actuator area (Pressure) as a function of actuator displacement, for several voltages. The Kapton sheet is 12.5 μm thick and its length between the attachment point and the point of maximum vertical displacement is 300 μm . The load force is applied to a 40 μm length of the actuator near the point of maximum displacement. The dielectric thickness is 0.3 μm on each electrode and the dielectric constant is 3.0. A uniform two-dimensional mesh of 50 x 3 finite element quadrilaterals was used to perform the calculations.	10
Figure 8. FEM results showing the effect of changing the constraint on the horizontal distance between Kapton attachment points. The nominal distance between attachment points is 400 μm . Pull-in occurs at the minima of the 80 V curves.	11
Figure 9. FEM results showing hysteresis in actuator force per unit area as a function of displacement, when the dielectric surfaces of the electrodes are separated by 0.3 μm at the Kapton attachment points. The distance between attachment points is constrained to be fixed at 600 μm	12
Figure 10. Model parameters for the PolyMEMS Actuator unit cell, showing two alternate constructions.	13
Figure 11. Force versus displacement from equations 5 and 10.	16
Figure 12. Displacement versus voltage.	16
Figure 13. A comparison between the analytical model and finite element calculations. The blue markers in A. are finite element calculations of the actuator force (normalized to the actuator area and plotted as pressure) as a function of the displacement. The black lines are from the analytical model. B shows displacement as a function of applied voltage.	17
Figure 14. Unit cells with electrodes on only one side of each sheet (A) or both sides (B). The electrodes are the red lines.	19
Figure 15. Parameters for the model with double sided electrodes.	19

Figure 16a. Parameters in the analytical model of the actuator with the nonzero-thickness joint. This view shows the device at $V < V_{PI}$.	21
Figure 16b. Parameters in the analytical model of the actuator with the nonzero-thickness joint. This view shows the device at $V = V_{PI}$. As soon as the gap is closed, the rest of the actuator zips closed as well.	21
Figure 17. Comparison of the improved analytical model with FEM calculations. The agreement is excellent.	23
Figure 18. Force-displacement behavior of a circular unit cell.	25
Figure 19. The key parameters of the model. The external spring, k_s , can represent either a real spring-like load or an internal deformation. A constant force F_{ext} is pulling upwards on the actuator. The actuator is pulling down as a spring with spring constant $k_A = Ebt^3/2l^3$, when $V=0$, or as an electromechanical structure when $V>0$. In addition, there is a spring, with spring constant k_S , pulling up on the actuator. The external spring (which really represents the internal deformation) has a rest length L_0 .	27
Figure 20. Force versus displacement with an external spring or internal deformation.	28
Figure 21. Displacement versus voltage for the case where there is an external spring or internal deformation.	29
Figure 22. A basic process flow for the PolyMEMS actuator.	31
Figure 23. A 6" Kapton "wafer" containing patterned unit cells.	33
Figure 24. A. A typical AFM image of commercial Kapton. The average roughness is 700 Å (250 Å RMS) with a peak-to-peak well over 2000 Å. B. After planarizing with ~1 μm of polyimide. The average roughness is 60 Å (42 Å RMS) with a peak-to-peak 270 Å.	34
Figure 25. Electrostatic force vs. voltage, for planarized and unplanarized substrates.	35
Figure 26. The first two burn-in sweeps on a typical structure. Beginning with a low voltage sweep on the left, self-healing events appear as small current spikes and disappear after one or two sweeps. The maximum is slowly raised until the typical operating voltage is reached or exceeded. After the current spikes disappear, the capacitor has been fully burned-in up to that voltage.	36
Figure 27. The optical micrograph on the left shows a discharge crater from a self-healing event. The ~100 Å Al has been completely vaporized, eliminating the short. The electron micrograph on the right shows a similar crater. In this case, the ~300 Å Al was not completely burned away, and the short did not fully disappear.	37
Figure 28. Progressive "domino breakdown" on a device.	37
Figure 29. The photo at left shows the aluminum peeling off the Kapton substrate at the bond pad. On the right, a gold reinforcement layer has been added on top of the Al, creating a more robust bond. These held up well to handling and use.	38
Figure 30. As-deposited aluminum is smooth. Annealing at 400°C creates nodules. A 1 hr anneal (not shown) creates some nodules. A 3 hr anneal creates more and larger ones; and a 15 hr anneal creates even more and larger nodules.	39
Figure 31. Resistance of a 1 cm ² capacitor area having polyimide dielectric. The higher temperature bake results in significantly better resistance and lower leakage.	40
Figure 32. Face-to-face C-V measurements. The electrostatic force pulls the two surfaces close together, causing the capacitance to increase with increasing voltage.	42

Figure 33. C-V curves showing normal behavior and stiction.	42
Figure 34. AFM image and C-V curve showing high stiction on a relatively smooth surface, as might be expected for an optical contact.	44
Figure 35. AFM image and C-V curve showing high stiction on a relatively rough surface, opposite of what might be expected for an optical contact.....	44
Figure 36. C-V curves before and after removing ~ 1000 Å of the PMGI surface in an O ₂ plasma. Removal of the surface layer reduces the stiction, but creates a charged surface layer which can be removed by heating.....	45
Figure 37. C-V curves before and after removing ~ 1000 Å of the PMGI surface in photoresist developer. Removal of the surface layer reduces the stiction.....	45
Figure 38. A series of C-V measurements on a PVdF-dielectric device. The initial high stiction was reduced by a 10 minute oxygen plasma, but with reversed hysteresis. A 126°C bake reduced the hysteresis. A 198°C bake yielded high stiction again.	46
Figure 39. a. A resistivity diagram of a simple capacitor. The capacitor, in our case is formed from the two sheets of Kapton, with the thin aluminum film and the thicker dielectric layer. The interface between the two dielectrics is in the middle of the capacitor. b. A resistivity diagram for a dielectric with a high resistivity surface layer. This configuration produces stiction. c. A resistivity diagram for a dielectric with a low resistivity surface layer. This configuration produces low or no force.....	47
Figure 40. A resistivity diagram for the dielectric after O ₂ plasma etching. Plasma etching thins the high resistivity layer, reducing stiction, but creates a very thin, low resistivity layer on the surface. The combination requires an understanding of the time constants involved in the total structure.	50
Figure 41. An equivalent circuit for the resistivity diagram of Figure 40.....	50
Figure 42. A diagram showing the metal, the dielectric with a surface layer, and the substrate. When the metal is connected	52
Figure 43. Two types of pinholes that would allow an electric field from the substrate charge to penetrate into the capacitor. A is actual pinholes in the metal (Alternately, this could be areas of oxidized metal. Other than a different ϵ in that region, the effect will be the same). B shows metallic islands which are electrically isolated from the surrounding metal by nonconducting, oxidized grain boundaries.	52
Figure 44. The base molecule of polyimide. Assuming that current passes long the chain and charge is trapped on side groups may explain our substrate charging observations.	53
Figure 45. Long slits cut in a polymer sheet, showing the distortion near the slit edges. Rows of laser-cut holes eliminate the distortion. These devices were assembled using the technique shown in Figure 47A, appropriate for single layer actuators.....	54
Figure 46. Conceptual sketch of the two bond regions.....	56
Figure 47. Three different bonding methods. A. Tape or glue extruded through slots in one sheet bonds with the opposite sheet. In B, adhesive is deposited in a trench to guarantee that no extra gap results from this step. In C, a central, adhesive layer is exposed locally for bonding.	56

Figure 48. Photographs of a trench, with photoresist adhesive, before and after bonding. Excellent alignment between sheets was achieved. The PR flowed to fill the majority of the trench without spreading beyond the edges.....	57
Figure 49. The top drawing shows the structure as laid out on the wafer. Two adjacent units form a layer of unit cells. After folding in an alignment fixture, heat and pressure are applied to activate the adhesive. The result is the folded structure in the bottom drawing. Only one set of interconnects is required.....	57
Figure 50. A sequence of photos showing the assembly process of the folded actuator. 1. Actuator features, including the adhesive, are patterned onto a Kapton “wafer.” The features are cut out of the wafer using a UV laser cutting system, but small bridges hold the structure in the wafer. 2. The bridges are cut, releasing the actuator from the wafer. 3. Alignment holes in the structure are threaded onto pins in a specially built alignment jig. 4. A top cover plate is added to the stack, followed by the top block in the jig. 5&6. The jig is installed in a heated press which melts the adhesive allowing it to reflow and bond all surfaces together simultaneously.....	58
Figure 51. Schematic of the PolyMEMS Test Station.....	60
Figure 52. Generation 1 mask layout.....	60
Figure 53. A. An early Generation 2 mask layout, containing 1, 2, and 3-layer arrays. B. Later Generation 2 layout of the 13-layer array, shown as it is after cutting the structure out of the wafer.	61
Figure 54. Pull-in voltages for early Generation 1 actuators.....	62
Figure 55. Displacement as a function of the applied voltage for various applied forces. Pull-in was soft, but was occurring at approximately the predicted value (the shaded areas). This soft pull-in was seen very commonly on Gen. 1 actuators.	62
Figure 56. An example of stepwise pull-in. This actuator consisted of three unit cells lying side-by-side in a single layer. Each of the three cells had a fairly sharp pull-in, but each one at different voltages, producing the stepwise behavior. With careful viewing we could see the individual cells pulling in.	62
Figure 57. The desired sharp pull-in. Very careful alignment and assembly was required to get this behavior.....	63
Figure 58. Typical force-displacement (left) and pull-in voltage vs. force (right) plots for small unit cells from Gen. 1. The purely mechanical behavior agreed well with the model predictions, but the pull-in voltage was larger than predicted. Hand assembly is not precise enough to avoid the deformations that lead to this.	64
Figure 59. Typical data from a Generation 2 actuator with a small number of layers	65
Figure 60. Pull-in voltage vs. applied force for the data in Fig. 59. The measured data agrees well with the predictions of the analytical model.....	65
Figure 61. Force-displacement data from a 13-layer Gen. 2 actuator. The straight-line behavior is as expected, but the slope is approximately a factor of 2 off.....	66
Figure 62. A representative control circuit for powering a PolyMEMS actuator from a battery. The DC-DC converter (lower left corner) uses the most power in this circuit.....	70
Figure 63. An artists rendition of muscle myofibril, an array “unit cells” configured side by side to generate large forces, and stacked end to end to generate large displacements.	72

Figure 64. The Robolobster of Northeastern University.	72
Figure 65. Analytical model calculations show that the increased force required for a Robolobster robot can be achieved in a PolyMEMS actuator if the Kapton thickness is increased to ~75 mm.	74

List of Tables

Table 1. A comparison of artificial muscle requirements for biomimetic robots with the various available technologies. PolyMEMS is the only technology that can meet all requirements	73
--	----

PolyMEMS Actuator: A Polymer-Based MEMS Actuator with Macroscopic Action

1.0 Executive Summary

A polymer-based MEMS actuator, consisting of small unit cells in a macroscopic array, was developed and demonstrated. The actuator consists of small unit cells built into a 3-D array. Each unit cell is pulled open by the application of an external load, and is electrostatically actuated closed by applying a voltage above a threshold pull-in voltage. The addition of unit cells in a single plane of the array increases the force of the total array, while the cells stacked in the direction of motion increase the total displacement of the array. Throughout the program we developed and refined models describing the actuator behavior, both in ideal and nonideal cases. An analytical model was very useful and provided insight into the primary design dependencies. Finite element modeling verified the analytical predictions. A fabrication process was also developed for building PolyMEMS actuators. The initial procedures, which required hand assembly of the unit cells and arrays were improved to achieve batch fabrication of the entire array. Deformations in the structure, either due to imperfect assembly or to stresses in the materials, resulted in imperfect performance. Further work is required to develop a reliable assembly process. Polymers were used throughout the program, instead of the more traditional silicon material. The fabrication processes required for this actuator cannot be done in silicon, but work well in polymers. Numerous polymer-based fabrication procedures were developed. Many of them borrow from either silicon or flexible printed circuit manufacturing, but modifications were necessary in order to adapt the processes to MEMS. The actuator is very efficient and uses very little power, making it suitable for autonomous applications such as robots.

2.0 Introduction

The PolyMEMS program had a two-fold objective:

- To develop a MEMS technology based on polymers; in this program we focused on materials and processes similar to those used for flexible printed circuits
- To apply this PolyMEMS technology to a family of lightweight, low-power electrostatic actuator arrays capable of generating large forces and displacements. Target goals for the PolyMEMS actuator were 3 mm displacement from a 10 mm actuator (30% strain) and 1 N of force per cm² of actuator area.

The second objective was driven by the continuing need for smaller, lighter-weight, lower-power actuators in existing and emerging military and commercial systems. The first objective was driven by the need for these actuators to have outputs - forces and displacements - on a macroscopic, rather than a microscopic, scale. Silicon-based MEMS typically cannot meet these requirements, so MEMS based on other materials are needed.

The PolyMEMS actuator consists of a stack of a large number of laminated polymer sheets. The lamination occurs only in local areas, so when the two ends of the stack are pulled apart it opens like an accordion or bellows. Each unit cell of this structure has a thin metal film and a thin dielectric film on both polymer surfaces. When a sufficient voltage is applied between the two facing surfaces, the resultant electrostatic force pulls the cell closed. The total force is the sum of the forces of all the cells on a single sheet of polymer. The total displacement is the sum of the displacements from all the sheets. Thus, both large forces and large displacements are possible from the device. Figure 1 shows artists conceptions of a unit cell and a fully packaged actuator.

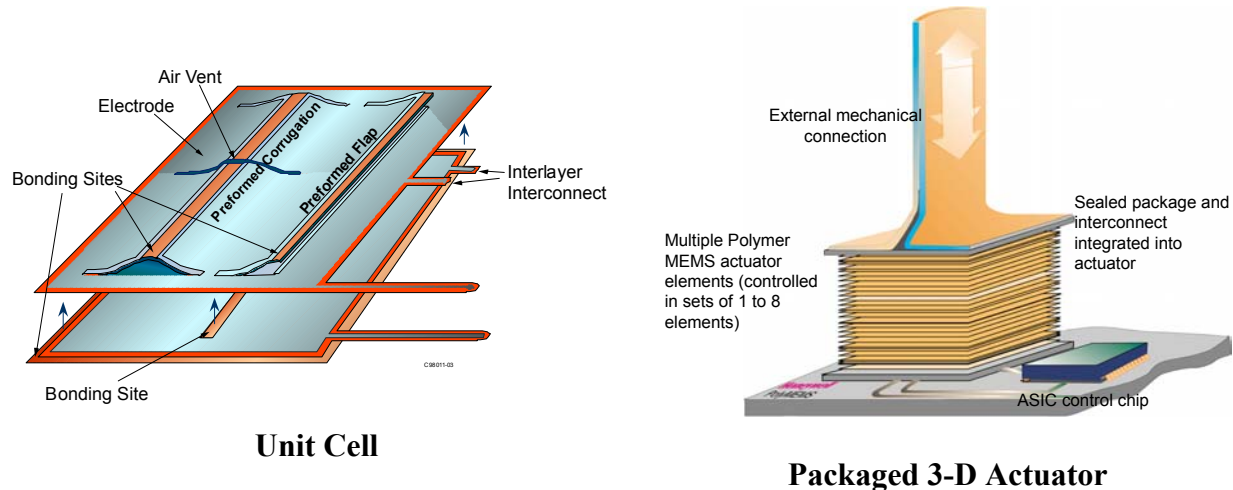


Figure 1. Concept drawings of the PolyMEMS electrostatic actuator unit cell and fully packaged actuator. The stack of metalized polymer sheets and their electrical connections are attached to a circuit board end cap and contained in a flexible hermetically sealed bellows. The mechanical linkage to the load resides on the end cap.

PolyMEMS actuators have many attractive characteristics. They are fabricated in polymers, not silicon. Fabrication techniques similar to those used in silicon-based MEMS can be used, but many more possibilities exist. These come from the huge variety of polymer fabrication techniques available. Polymer fabrication can be very low cost and can be done quickly. Therefore, “batch fabrication” may not look the same in plastics as it does in silicon, but similar cost savings are realized. Since most polymers have densities ranging from less than 1 g/cm^3 to $\sim 1.5 \text{ g/cm}^3$, PolyMEMS devices will be light weight. The electrostatic actuation is efficient and requires very small amounts of power. Modest voltages of ~ 50 to $\sim 250 \text{ V}$ are required. These can be obtained from a battery and a commercially available DC-DC step-up voltage converter. Macroscopic outputs can be obtained, yet with high resolution of both force and position. Finally, the “package” of a polymer-based device can be monolithic with the device itself. Packaging of silicon based MEMS requires putting the silicon device into something else, often a polymer package. With polymer devices, the package can be built simultaneously and in the same substrate as the device.

The PolyMEMS program was a 45 month effort, beginning 2 July 1998, divided into four stages of device development. The first stage was the initial design and process development. Stage two was the first cycle of fabrication, focusing on building and testing individual unit cells. Stage three was the second fabrication cycle, focused on the 3-D arrays of unit cells. The final stage was the third fabrication cycle, where actuators were to be designed, built and packaged for demonstration.

The PolyMEMS program was divided into six technical tasks and one program management task. The tasks were: 1. Actuator Design; 2. Process Development; 3. Actuator Fabrication; 4. Control System Development; 5. Actuator Characterization; 6. Program Management, and 7. Application Development.

3.0 Methods, Assumptions and Procedures

This section will cover the theoretical modeling, design, process development and fabrication of the actuators. Test results and discussion will be in Section 4.0.

3.1 The PolyMEMS Actuator Concept

3.1.1 Unit Cells and Arrays

Figure 2 illustrates the concept of the PolyMEMS actuator. Two sheets of a suitable polymer substrate (lower left) are patterned with metal and dielectric films. The sheets are bonded together at localized spots forming a planar array of “unit cells.” The unit cell is the basic unit of actuation. When an external load is applied to the upper and lower surface of the actuator, the cells open up. The polymer structure has some non-zero stiffness, so it acts like a spring. The rest state of the spring is fully closed, and the displacement is a linear function of the applied load. The interior surfaces of the cells have a metal electrode covered by a thin dielectric. These films form a capacitor between the upper and lower sheet. When a large enough voltage is applied across this capacitor, the electrostatic force causes the cell to “zip” or “roll” shut, starting from the edges (the bond sites) and moving toward the center.

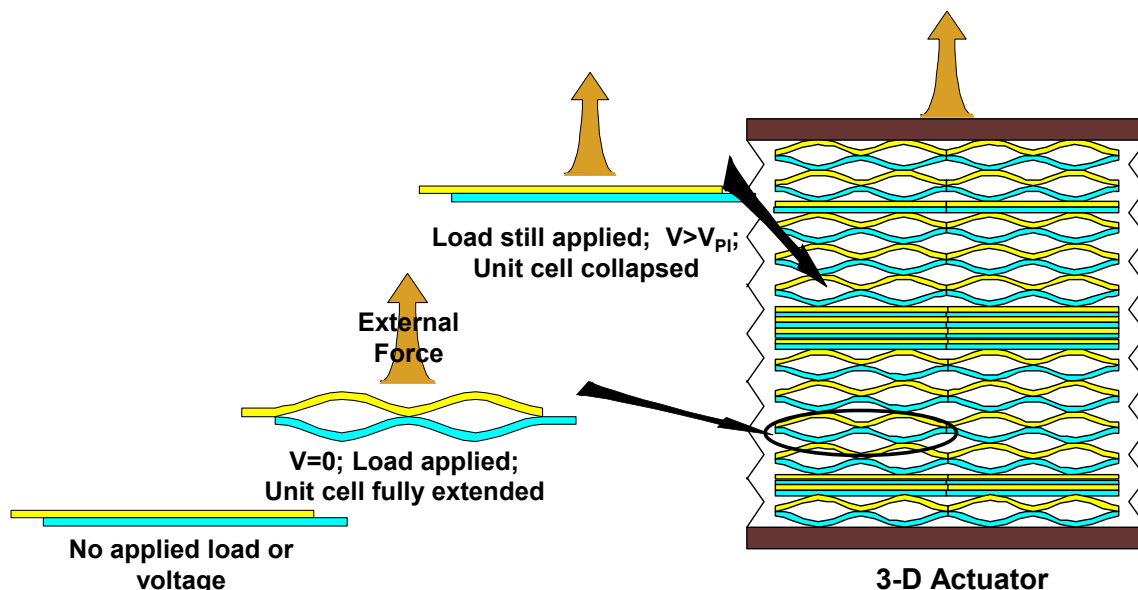


Figure 2. Diagrams showing the basic construction and operation of microscopic or mesoscopic unit cells, and the incorporation of multiple unit cells into a 3-D array that is capable of generating a macroscopic force and displacement.

If one unit cell can produce a given force, then N unit cells, all fabricated in the same two polymer sheets, can produce N times the force of the one cell. Hence, the planar array of cells can be designed to produce forces that are macroscopic in magnitude. Typical MEMS actuators

are capable of producing microNewtons and milliNewtons of force. The PolyMEMS actuator should be capable of producing Newtons of force. The unit cell dimensions are microscopic or mesoscopic (typically a few μm or less). The planar array will have macroscopic dimensions, on the order of a square centimeter. Similarly, if one planar array deflects a given amount under a given external load, then N planar arrays stacked on top of each other will deflect N times that amount. Thus, although the deflection of one plane may be microscopic, the deflection of the 3-D array can be macroscopic. For example, our initial estimates, which became the program goals, were that we could achieve a 1 N force from a 1 cm^2 array, and a deflection of 3 mm.

If voltage is applied to all layers simultaneously, the entire actuator will suddenly move from fully open to fully closed. However, if the voltage is applied only to selected layers (see Fig. 3), then only those layers will close. Thus, some level of proportional control – with small but discrete levels – can be achieved. Instead of varying a voltage to get proportional control, you vary the number of layers being actuated. This requires separate electrical connections to each layer or group of layers. An efficient way to configure this would be to operate some layers individually. Others would be connected in groups of two layers, others in groups of four layers, others in groups of eight, and so on. Any number of layers can be actuated by addressing the appropriate combination of groups. The position resolution would be equal to the displacement of a single layer.

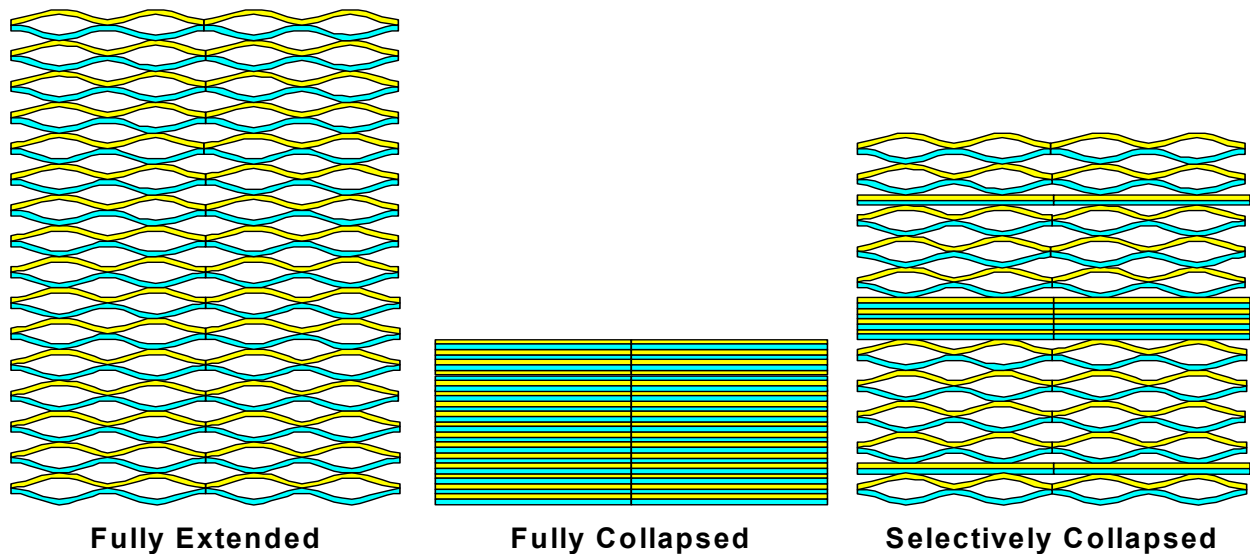


Figure 3. Various modes of operation of the PolyMEMS actuator. The array on the left has no voltage applied and is fully extended by an applied load. The extension is a function of the magnitude of the load. The center drawing shows an array that has been fully collapsed by applying a sufficiently high voltage to all layers of the array. The drawing on the right shows an array in which voltage has been applied to only selected layers in the stack.

Since the electrostatic forces are only attractive, the PolyMEMS actuator is active in only one direction. That is, it can only pull and not push. In order to get bidirectional actuation, two

“antagonistic” actuators are required – one to pull in one direction and the other to pull in the opposite direction. Biological muscle works the same way. It supplies force only in tension and an antagonistic pair is required for bidirectional motion (for example at the elbow or knee). This observation already points to one potential application – robotics – for PolyMEMS.

3.1.2 The Unit Cell Operation

Figure 4 shows a unit cell in more detail. The plastic “backbone” of the cell has some stiffness and, therefore, a spring constant. With no voltage applied it behaves like a spring. Boundary conditions due to assembling the flexible layers with a rigid upper and lower plate create some nonlinearities in this spring-like behavior, but these are typically not significant.

The metal layer is very thin for two reasons. First, it is preferable that the metal layer not add any mechanical stiffness to the structure. Second, a phenomenon known as self-healing, which will be discussed in detail later, plays a key role in the device operation, and this requires a thin metal layer.

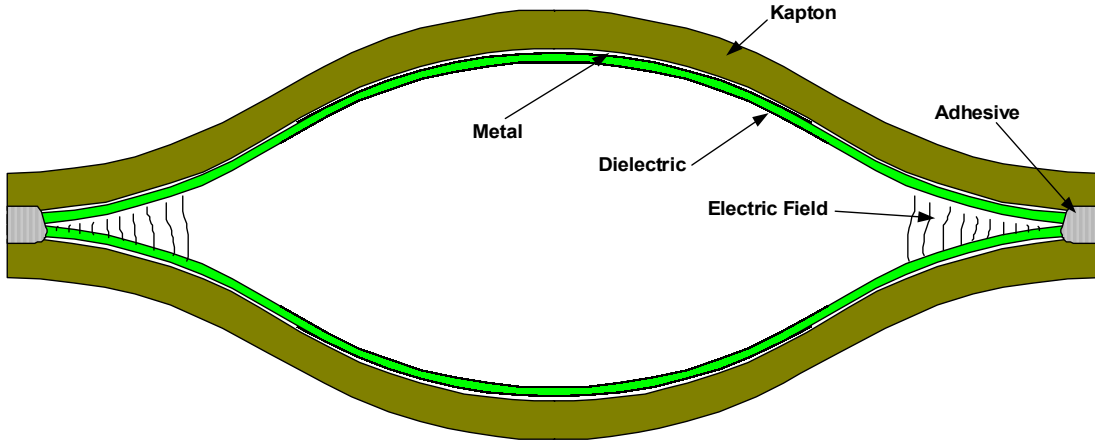


Figure 4. A detailed cross-section of a unit cell.

The dielectric layer prevents the two metal layers from shorting together. It should be as thin as possible so that the electric field drops primarily across the air gap and not the dielectric, and results in a high force. For the same reason, the dielectric should have a high dielectric constant. Intuitively, it would seem that if the dielectric constant is high, the capacitance of the collapsed unit cell will be large, and the power source would need to supply more charge, an undesirable feature. However, it can be shown that this is not the case. The power input P is proportional to the dielectric constant, $\epsilon_o\epsilon$, the dielectric thickness d , and the voltage V as

$$P \propto \frac{\epsilon_o\epsilon}{2d} V^2 .$$

It will be shown later that the voltage required to pull an external load F is

$$V \propto F \sqrt{\frac{2d}{\epsilon_o \epsilon}}$$

Thus, for a given load, the power goes as

$$P \propto \left(\frac{\epsilon_o \epsilon}{2d} \right) \left(\frac{2d}{\epsilon_o \epsilon} \right) F^2 = F^2$$

which is independent of the dielectric constant. The increased capacitance due to a large dielectric constant is cancelled by the decreased voltage requirement, leaving the input power unchanged. Therefore, the largest possible dielectric constant is desired.

Lastly, the adhesive needs to be applied in such a way that it introduces no additional distance between the two opposing surfaces. If it did, the available force would be quickly reduced.

When a voltage is applied across the unit cell, the field is very high at the edge, where the spacing between surfaces is smallest. The field, and the electrostatic force, drops off very quickly as the air gap increases. Therefore, only a small region near the contact point actually contributes to the actuation. This high field region zips in along with the contact point as the unit cell zips shut. Figure 5 schematically shows this behavior.

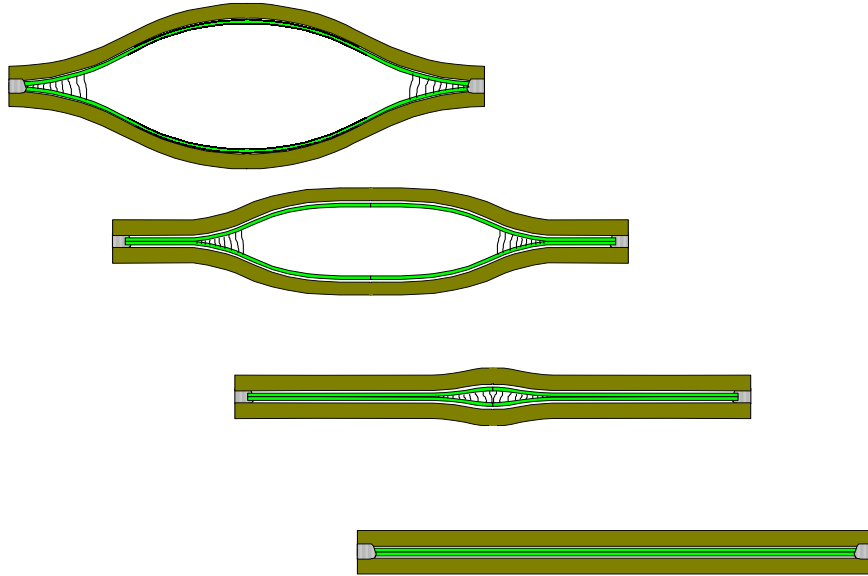


Figure 5. Zipping behavior of the unit cell at pull-in.

3.1.3 The Unit Cell and Array Configuration

Many potential unit cell shapes and array configurations can be envisioned. The simplest shape is the “standard” unit cell that has been described so far. Alternate shapes would include a circular or rectangular unit cell where the edge is bonded all the way around. Figure 6 shows several other possibilities of interest. Our initial approach was the corrugated design with the rigid centerplanes. By inserting the planar layer between the flexible layers, the distance between electrodes is reduced. It was expected that this would greatly increase the force that could be generated, as compared to the corrugated design without the rigid centerplanes. It will be shown below that this is not true. In addition, the rigid centerplanes proved very difficult to make. Therefore, this design was abandoned in favor of the design without the centerplanes. The S-shaped flexure is an alternative that avoids nonlinearities due to stretching. In the corrugated versions, the flexible layers cannot bend far before stretching energy dominates. This is because the distance between the two ends of the unit cell is fixed. This is true for all layers when centerplanes are present, and for the topmost and bottommost layers, near a rigid top and bottom cap layer, when centerplanes are absent. The S-shaped flexure avoids this completely. On this contract, the nonlinearity was never enough of a problem to make it worth pursuing the S-shaped flexure.

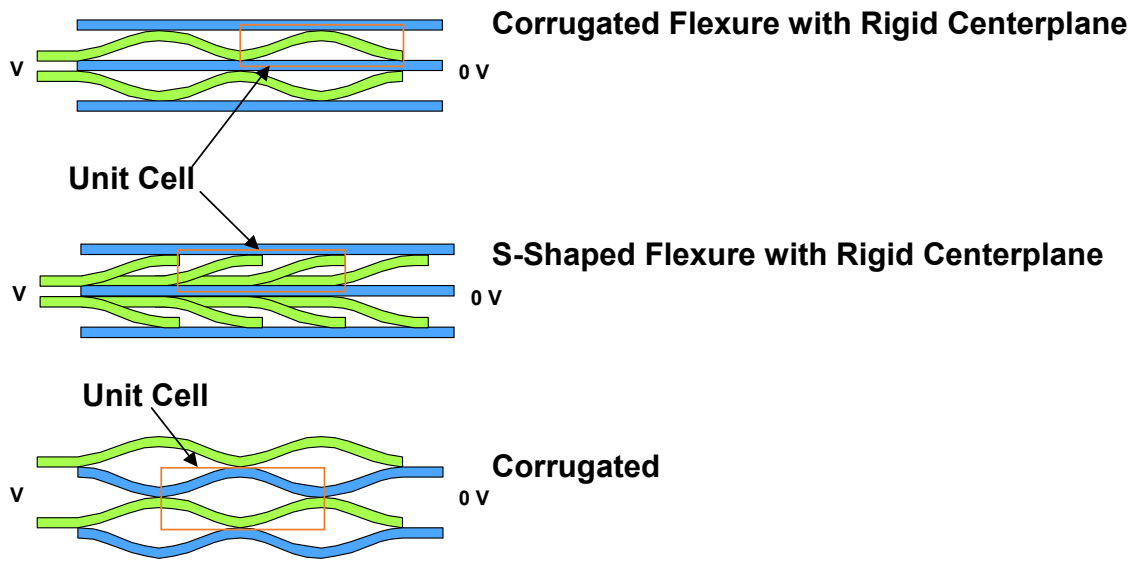


Figure 6. Possible unit cell configurations. In each case, the metal/dielectric electrodes can be present on all surfaces or only on a subset of the surfaces.

The simplest array configuration would be several standard unit cells placed side by side in a linear array within one layer, with identical copies of this layer stacked on top of each other. Obviously, more complicated configurations are possible, but only make sense if there is a compelling reason.

3.2 Modeling

Both finite element (FEM) and analytical models were developed for the PolyMEMS actuator. While FEM allows modeling of detailed geometries and non-ideal parameters, it requires considerable time. Coupling between the electrostatic domain and the mechanical domain is challenging in FEM. At the time this contract started, commercially available FEM packages were not adequate so we wrote our own iterative code in ANSYS. Today's commercially available software should be capable of doing this simulation much better.

For most of our design and proof-of-concept work, detailed FEM was not required and an analytical model was sufficient. This matched very well with the FEM, so the analytical model was used throughout the program for design changes and analysis. The advantage of the analytical model is that geometry changes can be very quickly made, so that an extremely wide design space can be explored. The discussion below will focus primarily on the analytical model, with FEM results used to demonstrate the accuracy of the analytical model. The FEM is described first to provide the basis for the comparison.

3.2.1 Finite Element Modeling

Finite Element Modeling

The goal of the finite element modeling (FEM) calculations was to estimate force and displacement for an actuator unit cell as functions of the actuator dimensions, mechanical properties, dielectric properties, and voltage. The modeling approach was performed for a single sheet of Kapton with an electrode on its lower surface which is attracted electrostatically toward a flat, rigid ground plane having a thin layer of dielectric (similar to Figure 10A). The Kapton sheet has one edge anchored to the ground plane, and the opposite edge free to move only in the vertical direction (except as noted below). This model represents one quarter of a unit cell. The unit cell would be an extrusion out of the page of Figure 10A, and would have mirror symmetry across the x and y axes of Figure 10A.

Several unique challenges were encountered. The most important was the extremely wide range of critical dimensions. Both thickness and length of the Kapton sheet are critical to its bending stiffness. Yet the thickness is only $\sim 25\text{ }\mu\text{m}$ while the length is $1,000 - 10,000\text{ }\mu\text{m}$. The region over which the electric field varies is only a few 10s of microns long and only a micron or so high. And the dielectric can be as thin as a few tenths of a micron. Thus the mesh size for the model had to contend with a dynamic range of 10^5 in dimension. Failure to deal with this led to hysteresis in the model results depending on the initial conditions of the actuator (e.g., open or closed). This was especially true when the dielectric thickness was $0.1\text{ }\mu\text{m}$. Finite element modeling results with the dielectric thickness of $0.3\text{ }\mu\text{m}$ or above show negligible hysteresis in force vs. displacement even when a uniform mesh size is used.

The example FEM results in Figure 7 show actuator force vs. displacement for several voltages, with an actuator unit cell having $600\text{ }\mu\text{m}$ horizontal distance between Kapton attachment points, a Kapton sheet thickness of $12.5\text{ }\mu\text{m}$, a dielectric thickness on each electrode of $0.3\text{ }\mu\text{m}$, and a dielectric constant of 3.0. This actuator design can pull a constant load of

1 N/cm², through a displacement of 7-8 μm between each layer of Kapton in the array, at an applied voltage of ~ 70 V (interpolate between the minima of the 60 V and 80 V curves to see this). The program goals of 1 N/cm² force and 3 mm displacement could be achieved with this unit cell geometry. Since the cells are 600 μm across by 1 cm long, there would be ~ 17 cells in a 1 cm² sheet. And if each sheet of cells moves 8 μm at this force, then 375 layers of cells would have to be stacked on top of each other. While this may be feasible, the large number of layers is undesirable and other dimensions are better suited for meeting the program goals.

The FEM results described in the previous paragraph assumed that the horizontal distance between Kapton attachment points does not change as the actuator vertical displacement changes. This assumption is not usually true in an array of actuators, where expansion in the vertical direction is expected to cause contraction in the horizontal direction. The mechanical boundary conditions on a unit cell of such an array are in general quite complex, and will not be the same for all cells in the array. In order to establish bounds on the performance of a unit cell actuator in such an array, FEM calculations have been carried out assuming the distance between attachment points remains either fixed, or is free to vary, as the actuator vertical displacement changes. Figure 8 shows that the two cases are different by only about 10% in the actuator force and displacement at pull-in. Note that when the distance between the attachment points is constrained, the actuator is stiffer than without the constraint, but only at large displacements.

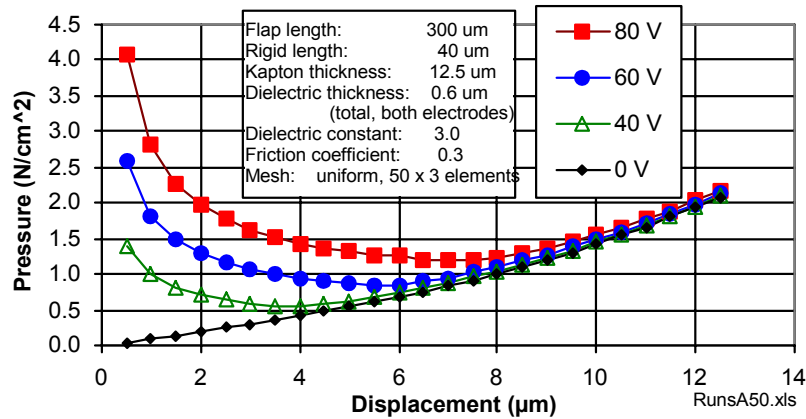


Figure 7. FEM results for actuator force per unit actuator area (Pressure) as a function of actuator displacement, for several voltages. The Kapton sheet is 12.5 μm thick and its length between the attachment point and the point of maximum vertical displacement is 300 μm . The load force is applied to a 40 μm length of the actuator near the point of maximum displacement. The dielectric thickness is 0.3 μm on each electrode and the dielectric constant is 3.0. A uniform two-dimensional mesh of 50 x 3 finite element quadrilaterals was used to perform the calculations.

It is desirable to have one or more points where the dielectric surfaces of the electrodes are initially in contact before voltage is applied. At these points, the electrostatic pressure will be high, even at low voltage, so that the “rolling contact” motion of the actuator can be easily initiated as the voltage is ramped up. During assembly of the actuators, the adhesive could create a nonzero separation between the dielectric surfaces of the electrodes at the attachment

points, thus making it difficult to initiate the rolling contact motion. Finite element modeling was performed to determine the importance of this undesired effect. As shown in Figure 9, an adhesive layer thickness of only $0.3\text{ }\mu\text{m}$ can produce substantial hysteresis in the force vs. displacement at a constant voltage. We believe this is a real, physical hysteresis, due to difficulty of initiating the rolling and unrolling motions of the actuator. It is not an artifact of the FEM calculation. For a “digital” actuator, designed to be either completely open or completely closed, this hysteresis may not be a problem, as long as the adhesive is thin enough. However, Figure 9 illustrates that it is highly desirable to bond the Kapton sheets so the dielectric surfaces of the electrodes are touching near the attachment points.

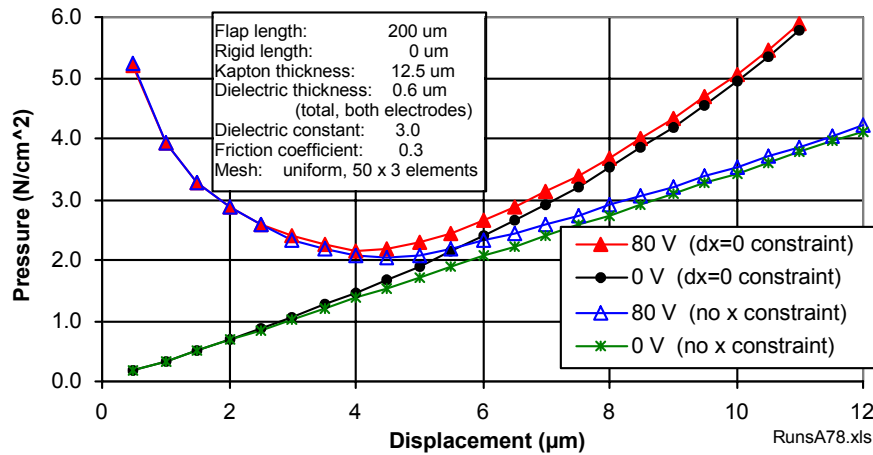


Figure 8. FEM results showing the effect of changing the constraint on the horizontal distance between Kapton attachment points. The nominal distance between attachment points is $400\text{ }\mu\text{m}$. Pull-in occurs at the minima of the 80 V curves.

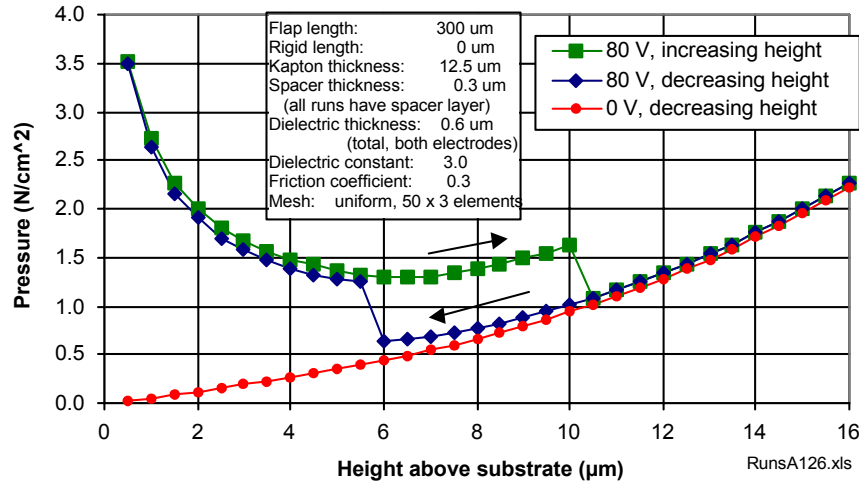


Figure 9. FEM results showing hysteresis in actuator force per unit area as a function of displacement, when the dielectric surfaces of the electrodes are separated by 0.3 μm at the Kapton attachment points. The distance between attachment points is constrained to be fixed at 600 μm .

3.2.2 The Analytical Model

A basic version of the analytical model was derived first. This was modified to explore the effects of non-zero gaps at the bond sites, a circular unit cell shape, off-center bond locations, and built-in deformations or spring loads.

Figure 10 shows the parameters used in the basic model. Both of the basic designs – with and without the rigid (flat) centerplane – are shown. Only half of the unit cell is shown. The other half is identical, by symmetry. The distance from the center of the cell to the edge is l . When no voltage is applied, the surfaces are separated at all points except the end point at l . The drawings show the cell with a voltage applied, where the contact point has moved to a distance c from the center of the cell. Obviously, c can never be larger than l .

The model uses energy minimization to derive equations for deflection with and without applied voltage, and an equation for the pull-in voltage. The “system,” in this case, is the actuator plus its power source. The total energy of the system has four terms:

1. electrostatic energy, U_E , stored in the electric field of the capacitor formed by the metal films;
2. electrical work, U_P , done by the power source;
3. bending energy, U_B , of the actuator (i.e., the spring energy of the polymer structure);
4. work, $W = F_{ext}\delta$, done on the actuator by the external force, F_{ext} , moving the actuator through a distance δ .

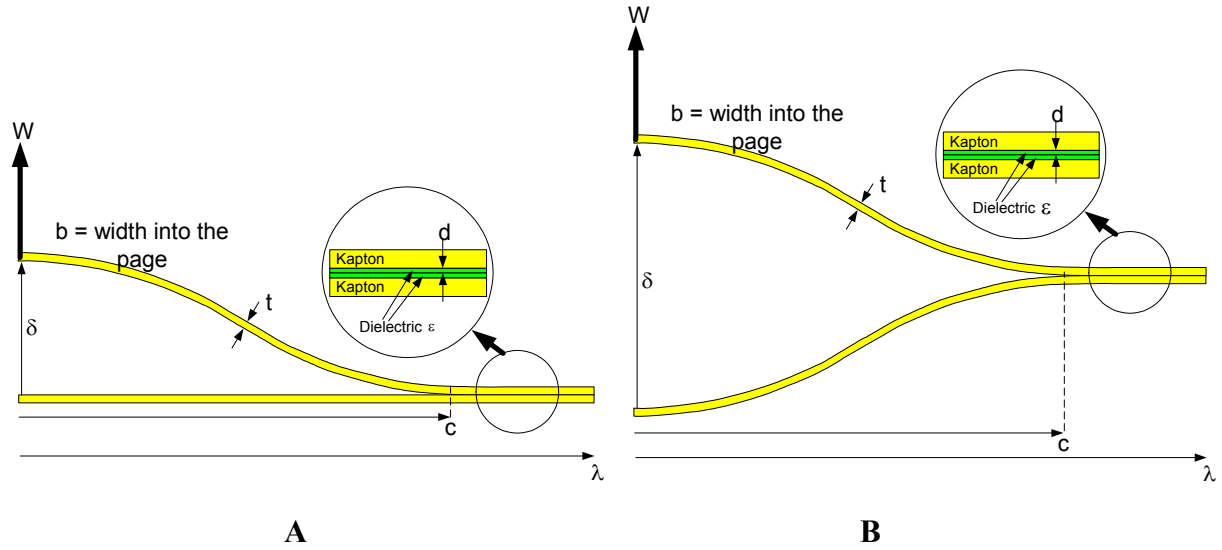


Figure 10. Model parameters for the PolyMEMS Actuator unit cell, showing two alternate constructions.

The electrostatic field (and therefore the electrostatic energy) drops off very rapidly as the separation between the sheets increases. Simple estimates and finite element models show that the field is negligible when the gap is a little over $1\text{ }\mu\text{m}$. This occurs over a distance along the x -axis on the order of 10 microns, which is small compared to the total length of the cell. Therefore, we can assume, with little loss in accuracy, that the electrostatic energy is constant where the gap is zero, and the energy is zero everywhere the gap is nonzero. The gap is nonzero from the left hand edge (in Figure 10) to the contact point c , and is zero beyond that. The electrostatic energy, U_E , is then simply that of the parallel plate capacitor in the contacted region. The work done by the power source is $U_P = -QV$ where Q is the amount of charge that has had to move through the potential V . The sign is negative because the potential energy of the source decreases as it charges the capacitor. Since the actuator is a capacitor, $Q = CV$, and $U_P = -CV^2$. Therefore,

$$U_E + U_P = \frac{1}{2}CV^2 - CV^2 = -\frac{\epsilon_0 \epsilon b(l-c)V^2}{4d} \quad (1)$$

The bending energy is derived from the curvature of the sheet. Since the electrostatic force falls off so quickly, it has negligible influence on the profile of the curved sheet. This profile is that of a beam with a load F_{ext} at the end, and can be found in standard texts and reference books on stress and strain in materials.¹ The bending energy is given by

¹ For example, Roark and Young, *Formulas for Stress and Strain*, gives the profile as

$$y = \frac{F_{ext}}{Ebt^3}l^3 - \frac{3F_{ext}c}{Ebt^3}x^2 + \frac{2F_{ext}}{Ebt^3}x^3$$

$$U_B = \frac{Ebt^3}{24} \int \left(\frac{\partial^2 y}{\partial x^2} \right)^2 dx = \begin{cases} \frac{1}{2} k \left(\frac{l}{c} \right)^3 \delta^2 & c < l \\ \frac{1}{2} k \delta^2 & c = l \end{cases} \quad (2)$$

where k is the “spring constant” of the bent sheet, defined as

$$k \equiv \frac{F_{ext}}{\delta} = \frac{Ebt^3}{nl^3} \quad (3)$$

$n=1$ if the structure has flat centerplanes, as in Figure 10A, and $n=2$ if the flat planes are missing, as in Figure 10B.

The total energy is then

$$U_T = \frac{1}{2} k_A \frac{l^3}{c^3} \delta^2 - \frac{\epsilon_0 \epsilon b (l-c) V^2}{4d} + F_{ext} \delta, \quad (4)$$

First, consider the simple cases when $V=0$. Equilibrium is found by minimizing the energy with respect to δ .

$$\frac{\partial U_T}{\partial \delta} = k_A \delta + F_{ext} = 0 \quad \text{or} \quad F_{ext} = -k_A \delta, \quad (5)$$

the standard expression of Hooke’s Law for a spring. Note that if $V=0$, then $c=l$ since there is no electrostatic force to pull the contact point in.

To solve for the behavior with nonzero voltage, we first need to find the value of c for a given force and voltage. This is done by minimizing the energy with respect to c while holding all other dimensions fixed.

$$\frac{\partial U_T}{\partial c} = -\frac{3}{2} k_A \frac{l^3}{c^4} \delta^2 + \frac{\epsilon_0 \epsilon b V^2}{4d} = 0 \quad (6)$$

Solving for c gives

$$c^4 = \frac{6dk_A l^3 \delta^2}{\epsilon_0 \epsilon b V^2} \quad (7)$$

Plugging this back in gives the total energy, when c is at equilibrium, as

$$U_T = 2(k_A l^3)^{1/4} \left(\frac{\epsilon_0 \epsilon b V^2}{6d} \right)^{3/4} \delta^{1/2} - \frac{\epsilon_0 \epsilon b l V^2}{4d} + F_{ext} \delta. \quad (8)$$

Finally, as in the $V=0$ case, the equilibrium displacement is found by minimizing the energy with respect to δ .

$$\frac{\partial U_T}{\partial \delta} = (k_A l^3)^{1/4} \left(\frac{\epsilon_0 \epsilon b V^2}{6d} \right)^{3/4} \frac{1}{\delta^{1/2}} - \frac{\epsilon_0 \epsilon b l V^2}{4d} + F_{ext} = 0 \quad (9)$$

which rearranges to give an expression relating the external force, the displacement, and the applied voltage.

$$F_{ext} = - \left(\frac{\epsilon_0 \epsilon b k_A l}{6d} \right)^{3/4} \frac{V^{3/2}}{(k_A \delta)^{1/2}}. \quad (10)$$

The right hand side of (10) is the combined electromechanical force, F_{em} , produced by the actuator at displacement d and voltage V . The negative sign indicates the direction of the force (i.e., opposite to the direction of the external force). The sign can be dropped if we are just considering the magnitude of the force. Note that this expression is valid only for $c < l$. If $c = l$, there is no surface length in contact, and the electrostatic energy term is identically zero. Therefore, for $c = l$ the purely mechanical equation (5) is the correct expression.

To see that this results in a pull-in behavior, compare the two lines in Figure 11. Initially, with no external force applied and no voltage, the actuator has zero displacement. For illustration, suppose a 1 mN force is applied (red arrow #1). With the voltage still off, the actuator behaves like a spring, and displacement travels up the blue line (red arrow #2) until it reaches red arrow #3, the displacement at 1 mN force ($\sim 485 \mu\text{m}$). When the voltage is now turned on, the green curves represent the combined electromechanical behavior. The electromechanical force generated by the actuator at 10 V (the bottom green line) at $485 \mu\text{m}$ is small compared to the external force and the spring-like (i.e., mechanical only) actuator force. Therefore, the actuator still behaves like a spring, and the displacement does not move from position 3. The same is true at 20 V, 30 V, and 40 V. When the voltage reaches 47 V, the electromechanical curve intersects the mechanical curve at $485 \mu\text{m}$, causing the displacement to begin to get smaller (along red arrow #4). As it does, the electromechanical force increases even more, pulling the displacement in faster and faster until the actuator is fully closed. The deflection as a function of voltage, showing the classic pull-in behavior, is plotted in Figure 12. The deflection is approximately constant, and $c = l$, for V less than some threshold, or pull-in, voltage.

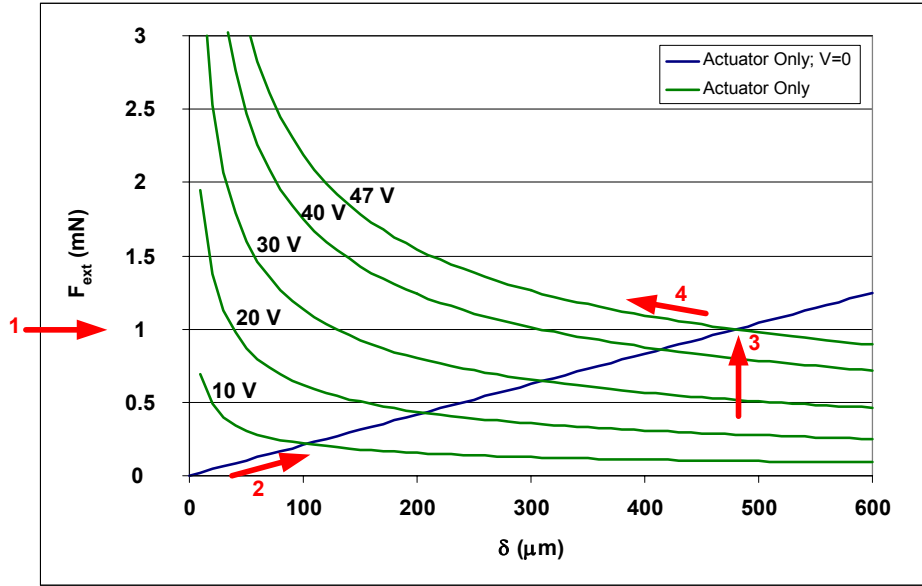


Figure 11. Force versus displacement from equations 5 and 10.

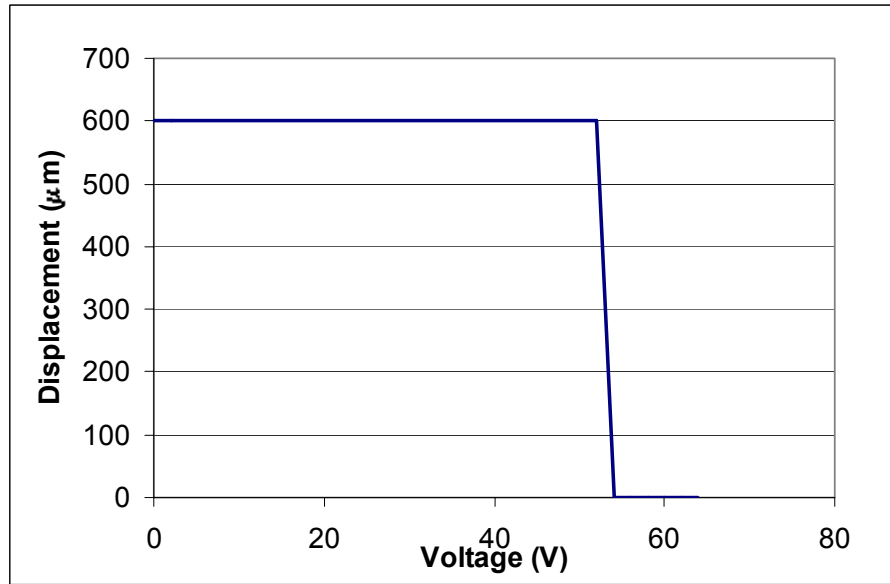


Figure 12. Displacement versus voltage.

The pull-in voltage, V_{PI} , is therefore the voltage at which equation (5), the purely mechanical response, equals equation (10), the combined electromechanical response. This yields one of the most useful equations for designing and assessing the actuator performance:

$$V_{PI} = \left(\frac{6d}{\epsilon_0 \epsilon b k_A l} \right)^{1/2} F_{ext} \quad (11)$$

3.2.3 Comparison with FEM

Figure 13A is a comparison of the analytical model with the finite element model. This graph should be interpreted the same as Figure 11. The dots represent FEM results while the lines are from the analytical model. The excellent agreement is obvious. Figure 13B compares displacement versus voltage calculated by the analytical model and FEM, also showing a good match. Although individual cases will vary, the analytical model can overestimate the displacement and/or the pull-in voltage by a small amount, typically no more than 10-15%. Figure 13 shows good agreement between the analytical model and FEM pull-in voltages, but the analytical model displacement is larger than the FEM prediction (Fig. 13B).

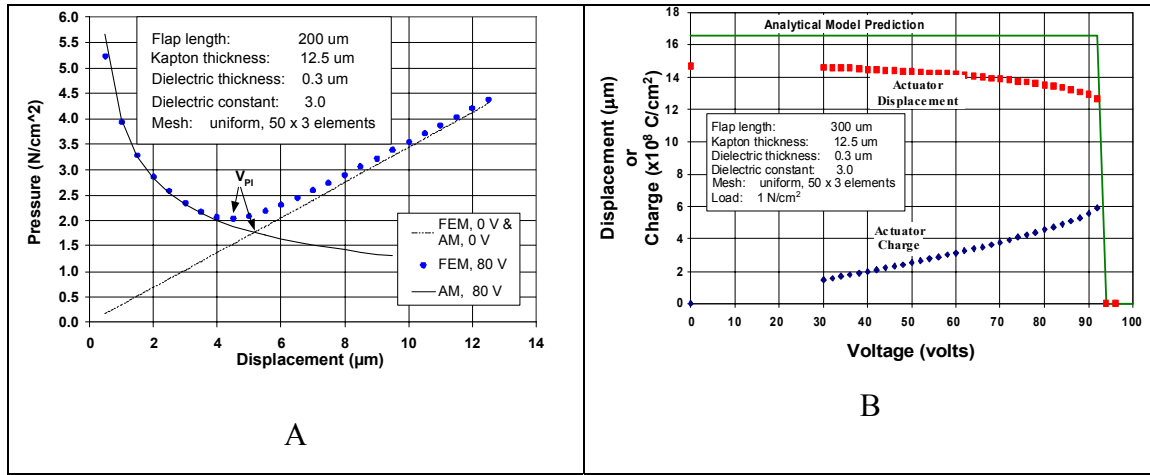


Figure 13. A comparison between the analytical model and finite element calculations. The blue markers in A. are finite element calculations of the actuator force (normalized to the actuator area and plotted as pressure) as a function of the displacement. The black lines are from the analytical model. B shows displacement as a function of applied voltage.

3.2.4 Comparison of Unit Cell Configurations

Two examples illustrate the power of this model. Equation (11) allows us to compare the various unit cell and array configurations described above. Referring to Figures 6 and 10, consider the unit cell with rigid centerplanes (referred to as the CP design) and the unit cell without rigid centerplanes (the NP design). The only difference between these two is that the NP spring constant, k_A , without centerplanes is half that of the CP cell with centerplanes (equation 3). Equation (11) then says that, for a given external force, the pull-in voltage for CP is 71% of the voltage required for the NP. Alternately, for a given voltage, the CP force is 41% larger than

the NP force. Despite these two advantages, there are also penalties for the CP design. First, the CP displacement per unit cell is half the NP displacement. Therefore, twice as many cells are needed for the same displacement, requiring twice the amount of plastic, doubling the material cost, and increasing the processing cost. Even worse, the work that can be done is

$$W = F_{ext} \delta = \frac{F_{ext}^2}{k_A} = \left(\frac{\epsilon_0 \epsilon b l}{6d} \right) V_{PI}^2 \quad (12)$$

which is independent of the spring constant. Therefore, for a given voltage, the NP design can accomplish the *same amount of work* as the CP design; the CP design has no advantage when viewed this way. In addition, the CP design, having twice as many layers, has twice the capacitance of the NP design. This means twice as much charge is required to charge it up, and twice as much power will be consumed. In other words, the same amount of work will be done, but at the cost of double the power consumption. Finally, in building mockups of the various unit cells, we discovered that the compressive in-plane stress on the centerplanes (when the external force is opening the cell) almost always exceeds the buckling stress of the centerplane. The plane buckles and becomes useless. As a result of all these negatives, the CP design was abandoned.

Another consideration is whether to put electrodes on both surfaces of each sheet or only on one surface of each sheet. Figure 14 illustrates the difference. The electrodes, represented by the red lines, are exaggerated so they can be seen easily. Initially it was expected that having twice the number of electrodes would produce twice the force. The model shows this is not the case. For double sided electrodes, the model is modified slightly, as shown in Fig. 15. In this case, pull-in occurs from both sides of the unit cell. We use a rather than c as the distance that has been pulled in. The electrostatic and bending energy terms become

$$U_E + U_P = -\frac{\epsilon_0 \epsilon b 2a V^2}{4d} \quad (13)$$

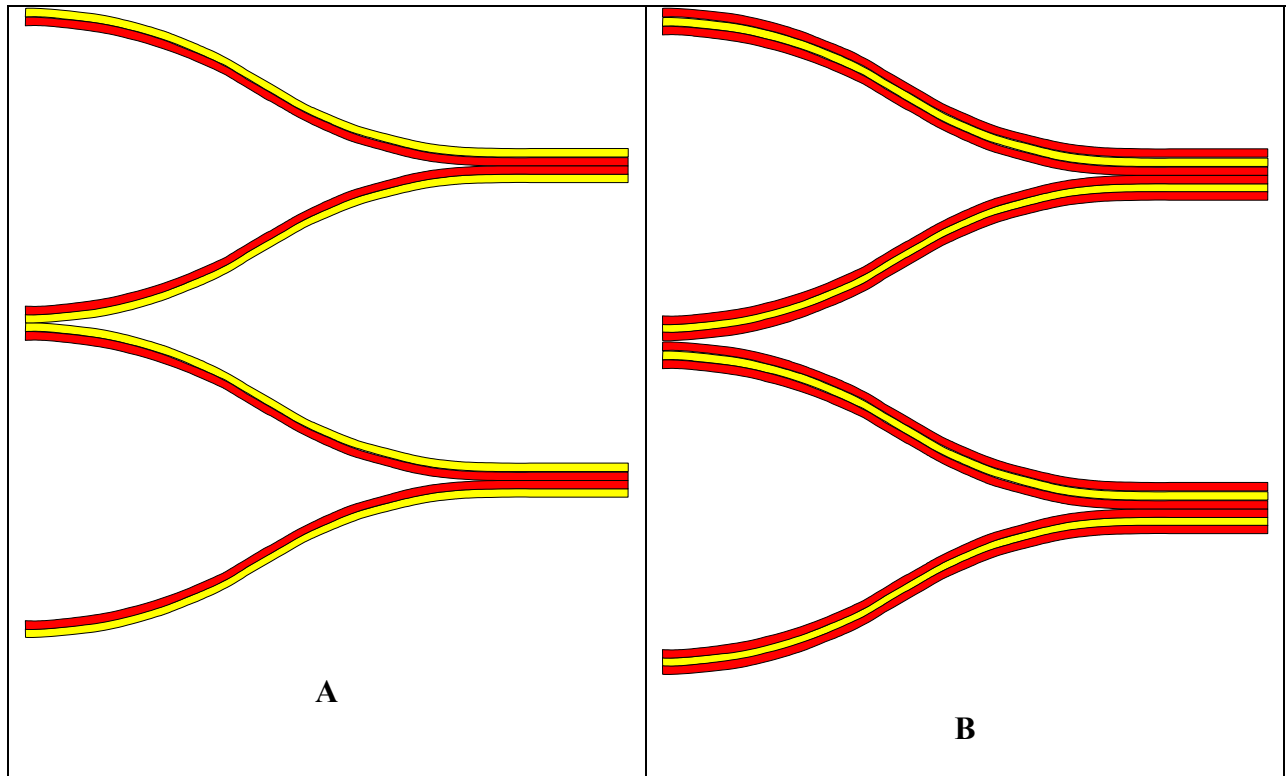


Figure 14. Unit cells with electrodes on only one side of each sheet (A) or both sides (B). The electrodes are the red lines.

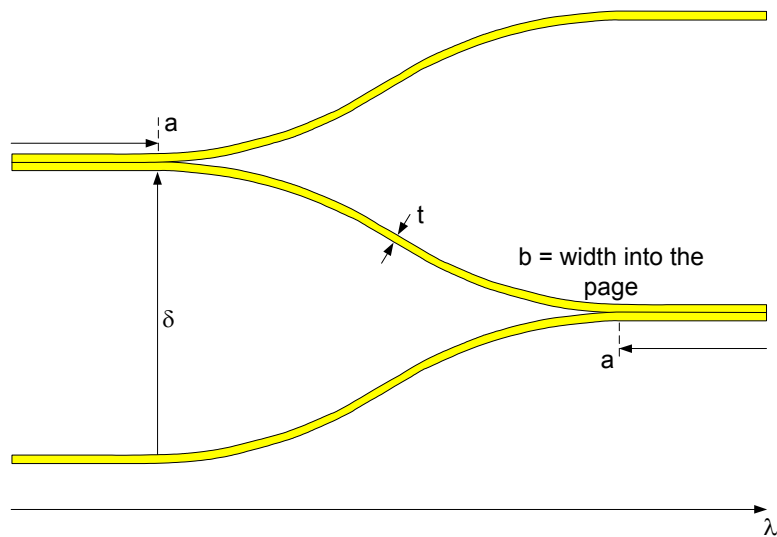


Figure 15. Parameters for the model with double sided electrodes.

and

$$U_B = \begin{cases} \frac{1}{2} k_A \left(\frac{l}{l-2a} \right)^3 \delta^2 & a > 0 \\ \frac{1}{2} k_A \delta^2 & a = 0 \end{cases} \quad (14)$$

Using the same approach as above, we find the force, displacement, and pull-in voltage equations to be identical to the original equations. The reason is that the balance between electrostatic and bending energy stays the same in both cases. Therefore, a is half of c . Since there is a distance $2a=c$ in contact on the double sided configuration, the results end up being identical. The penalty is that the double sided configuration requires double sided processing (nearly doubling the fabrication cost) and has twice the capacitance, consuming twice the power, yet produces no more force displacement or work. Therefore, the analytical model shows that the single sided electrode configuration is preferred over the double sided configuration.

3.2.5 Unit Cell With an Extra Gap

Since the electric field drops off quickly with distance it is important that the surfaces of the plastic sheets come into contact at the edge of the unit cell. If there is an extra gap, such as would be caused by a thick adhesive at the bond, the electrostatic force will be reduced and the pull-in voltage will be increased. The baseline model can be modified to show the effect of a nonzero gap, and this gives us insight into how much gap can be tolerated. Figure 16 shows the model parameters for this case.

We use basically the same approach as before. The electrostatic energy has to be modified. Previously, the electrostatic field (and energy) was assumed to be significant only in the clamped region of the actuator. If the gap, g , is small, we now make the assumption that the field is significant in a region from the boundary to a point, c , where the sheet separation is a minimum, and some distance beyond this point. Neither c nor this extra distance are known; c will be determined from the analysis, and the added distance will be accounted for using an adjustable parameter that can be determined from fitting to finite element modeling results. Initially, the minimum gap is at the boundary. As the voltage is increased, the minimum gap moves monotonically away from the boundary, allowing c to be used as the variable against which the total energy will be minimized. The electrostatic energy within this region is assumed to be equal to that of a parallel plate capacitor with separation g . This is also a simplification from the true situation since the two sheets are not truly parallel throughout the region. However, it is probably a good assumption for the following reason. In the original model (no gap) the energy was calculated as a function of the contact point. The energy was then minimized as a function of this point. It was found that the contact point stayed at the boundary until the pull-in voltage was reached, when the contact point suddenly zipped all the way to the center of the unit cell.

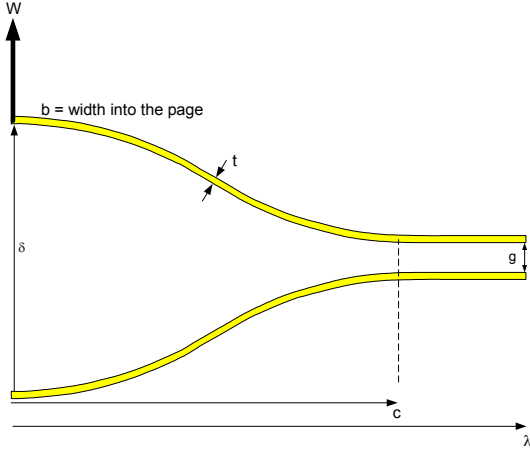


Figure 16a. Parameters in the analytical model of the actuator with the nonzero-thickness joint. This view shows the device at $V < V_{PI}$.

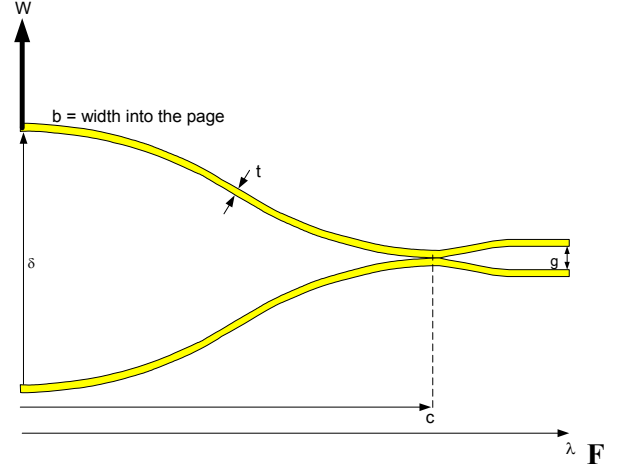


Figure 16b. Parameters in the analytical model of the actuator with the nonzero-thickness joint. This view shows the device at $V = V_{PI}$. As soon as the gap is closed, the rest of the actuator zips closed as well.

The FEM results showed that this was fairly accurate. We assume that the minimum gap point has a similar behavior in the nonzero gap model. That is, it does not move beyond the boundary until pull-in and, therefore, has a more or less static shape until pull-in. If the shape is static, then the energy can be approximated by that of a parallel plate capacitor with some effective gap which can be accounted for by another adjustable parameter. The work done by the power source follows the same line of reasoning as before. Therefore, the electrostatic and power source energy terms, $U_E + U_P$ are:

$$U_E + U_P = -\frac{b\epsilon_o\epsilon(l - Ac)}{4d(1 + Bg\epsilon/2d)}V^2 \quad (15)$$

where A and B are the adjustable parameters.

The bending energy, U_B , is derived from the curvature of the sheet as before. Note that if the minimum gap point is nearly at the boundary until $V = V_{PI}$, then the bending energy will be nearly the same as in the previous model. Prior to pull-in, the bending occurs over a distance equal to the total displacement, δ , minus the gap, g , and is evenly split between the top and bottom sheet. Therefore, the bending energy is

$$U_B = \frac{bk}{2}\left(\frac{l}{c}\right)^3(\delta - g)^2 \quad (16)$$

The total energy, U_T , is then

$$U_T = U_B + U_E + U_P + F_{ext}\delta = \frac{1}{2}k\left(\frac{l}{c}\right)^3(\delta - g)^2 - \frac{b\varepsilon_o\varepsilon(l - Ac)}{4d(1 + Bg\varepsilon/2d)}V^2 + F_{ext}\delta. \quad (17)$$

Using the same procedure as before, we arrive at

$$F_{ext} = \begin{cases} -k(\delta - g) & V < V_{PI} \\ -\frac{k^{1/4}}{(\delta - g)^{1/2}}\left(\frac{Al\varepsilon_o\varepsilon V^2}{6d(1 + Bg\varepsilon/2d)}\right)^{3/4} & V > V_{PI} \end{cases} \quad (18)$$

or, equivalently,

$$\delta - g = \begin{cases} -\frac{F_{ext}}{k} & V < V_{PI} \\ -\frac{k^{1/2}}{F_{ext}^2}\left(\frac{Al\varepsilon_o\varepsilon V^2}{6d(1 + Bg\varepsilon/2d)}\right)^{3/2} & V > V_{PI} \end{cases} \quad (19)$$

When a load is applied at $V=0$, the displacement is purely mechanical and is given by the upper expression in Equation 19. As the voltage is increased, the lower expression becomes nonzero, but the force is much smaller than the purely mechanical force of the upper expression.

However, when the voltage gets large enough, the force in the lower expression becomes larger than the upper one, and the actuator zips shut, just as before. Therefore, the pull-in voltage, V_{PI} , is where the two expressions are equal:

$$V_{PI} = \left(\frac{6d\left(1 + Bg\varepsilon/2d\right)}{Akl\varepsilon_o\varepsilon}\right)^{1/2} \frac{W}{b} \quad (20)$$

When $g \rightarrow 0$, Equation 20 reduces to the original equation derived earlier. Figure 17 shows a comparison of Equation 20 with finite element calculations.

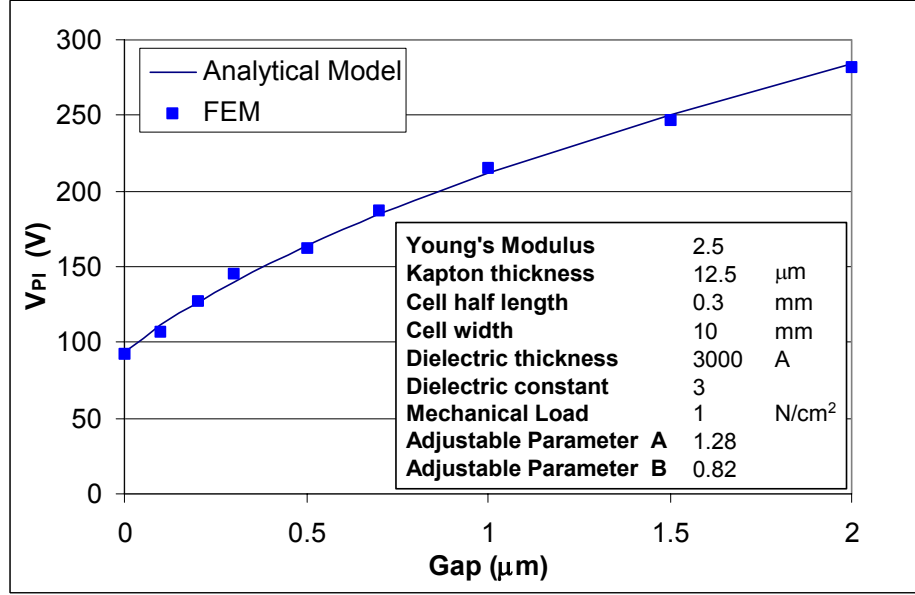


Figure 17. Comparison of the improved analytical model with FEM calculations. The agreement is excellent.

The key parameter caused by the gap is the extra term $Bg\epsilon/2d$ in equation (20). It is desirable that this term be kept to no more than ~ 0.2 , so that the overall effect of the gap is no more than $\sim 10\%$. Therefore, we want $g < 0.2(2d/B\epsilon)$. Taking $B=0.82$ from the fit to the finite element data, and $\epsilon=3$, which is typical for the polymer dielectrics we used, we find that g should be less than 16% of the thickness of the dielectric layer on each sheet. Since typical dielectric thicknesses are ~ 1 μm or less, the gap must be kept below about 1000 Å. For all practical purposes, this means the gap should be kept to zero.

3.2.6 Circular Unit Cell

Another modification that can be made is to consider another unit cell shape. The unit cell could be a circle or square with the sheets bonded together all around the perimeter. Leak holes would have to be placed in this type of cell to allow air to flow in and out as the cell opens and closes. Since there is more length with zero gap, this cell may be stronger. The model is derived the same as before, with the bending and electrostatic terms modified to account for the new geometry. Figure 10B can still be used to describe the cell, but now the profile is swept into a circle of radius l rather than extruded into the page. A small length, r_o , is defined as an area over which the external force is applied. The deflection profile for a circular plate unit cell (two individual plates) is given by (again from Roark and Young, reference 1)

$$\delta = 2z = -\frac{3F_{ext}(1-\nu^2)}{2\pi Et^3} \left[l^2 - r^2 \left(1 + 2 \ln \left(\frac{l}{r} \right) \right) \right] \quad (21)$$

The bending energy for a single plate is

$$dU_B = \frac{Et^3}{24(1-\nu^2)} \left[\left(\frac{\partial^2 z}{\partial r^2} + \frac{1}{r} \frac{\partial z}{\partial r} \right)^2 + 2(1-\nu) \left(\frac{1}{r} \frac{\partial z}{\partial r} \frac{\partial^2 z}{\partial r^2} \right) \right] 2\pi r dr \quad (22)$$

Calculating the derivatives from Eq. (21), plugging into Eq. (22) and integrating from r_o to l yields the total bending energy:

$$U_B = \frac{\pi}{3} \frac{Et^3}{(1-\nu^2)} \frac{\left\{ c^2 - r_o^2 - (6-2\nu)r_o^2 \left(\ln \frac{r_o}{c} \right)^2 \right\}}{\left\{ c^2 - r^2 \left(1 + 2 \ln \frac{c}{r} \right) \right\}^2} \delta^2$$

Assuming $r_o \ll c$, and replacing l with the variable parameter c , this simplifies to a more manageable form

$$U_B \approx \frac{\pi}{3} \frac{Et^3}{(1-\nu^2)c^2} \delta^2 \quad (23)$$

The electrostatic energy is based on the same assumptions as the basic model. For the circular geometry, this becomes

$$U_E + U_P = -\frac{\epsilon_o \epsilon \pi (l^2 - c^2)}{4d} V^2 \quad (24)$$

so that

$$U_T = \frac{\pi}{3} \frac{Et^3}{(1-\nu^2)c^2} \delta^2 - \frac{\epsilon_o \epsilon \pi (l^2 - c^2)}{4d} V^2 + F_{ext} \delta. \quad (25)$$

Following the same procedure as before, we take the derivative with respect to c , solve for c , plug that value back into the total energy, and finally set $\partial U_T / \partial \delta = 0$, with the result

$$F_{ext} = -\frac{\pi \sqrt{3}}{4} \left(\frac{Et^3}{(1-\nu^2)} \frac{\epsilon_o \epsilon}{4d} \right)^{1/2} V. \quad (26)$$

This is analogous to the basic model equation (10), and is valid for $c < l$. The interesting feature of equation (26) is that there is no dependence on δ . Figure 18 shows the force-displacement graph for the circular cell, analogous to Figure 11 for the linear cell. When the external force is applied, the cell opens up to some displacement. As the voltage is turned on and increased a combined electromechanical response is generated which is flat as a function of δ . Initially, the electromechanical force is less than the external force, and nothing happens. However, when the voltage is large enough, the actuator pulls in. The pull-in is different than before, however. In the model of the linear unit cell, as the cell pulled in slightly, the electromechanical force got even larger, producing a runaway pull-in. In the circular unit cell, the electromechanical and external forces are equal, resulting in no pull-in until the voltage just exceeds V_{PI} . Pull-in occurs, but it is not a runaway pull-in. Another way to express this is that in the linear model, kinetic energy is produced and increases as the cell pulls in. In the circular model, the cell pulls in at a constant velocity, and there is no increase in kinetic energy. This will have consequences when we consider power consumption later on. The pull-in voltage comes from rearranging eq. (26)

$$V = \frac{4}{\pi\sqrt{3}} \left(\frac{(1-\nu^2)}{Et^3} \frac{4d}{\epsilon_o\epsilon} \right)^{1/2} F_{ext}. \quad (27)$$

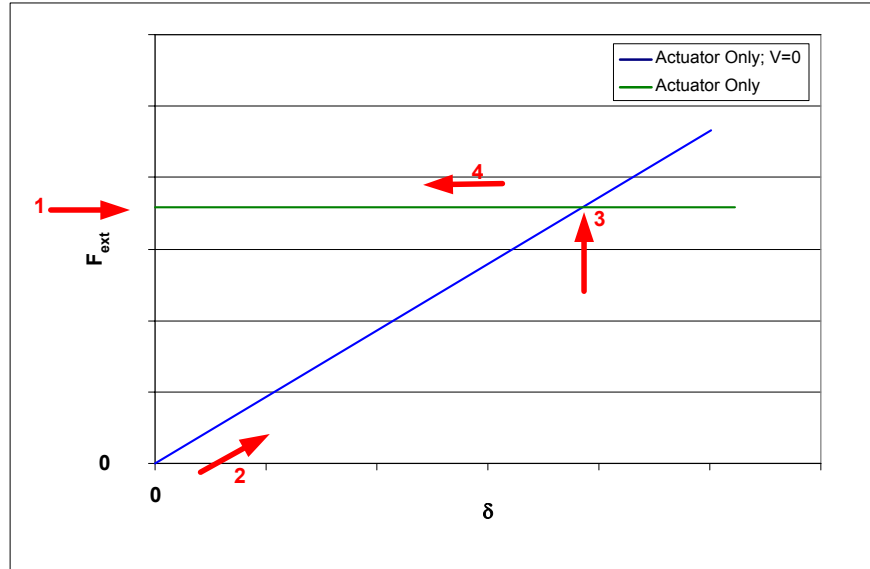


Figure 18. Force-displacement behavior of a circular unit cell.

3.2.7 Linear Unit Cell With a Spring-Like Load

A final modification is to consider a load that has a spring-like behavior rather than a simple constant force. Many (if not most) applications will have this sort of behavior. For example, if two PolyMEMS actuators are used as an antagonistic pair, then one actuator will have to pull against the spring of the other. It turns out that this model can also explain the behavior of the actuator if there are deformations built in to the polymer structure (for example, from the assembly process). Therefore, this model was critical in understanding some of the nonideal behavior we observed throughout the contract. To make the model as general as possible (this is needed for consideration of deformations) we have both a spring and an external force pulling on the actuator. Figure 19 shows the model used here.

The total energy for the system now has an additional term, the potential energy of the external spring. k_A is the spring constant of the actuator, given by equation (3), and k_S is the spring constant of the external spring.

$$U_T = \frac{1}{2}k_A \frac{l^3}{c^3} \delta^2 - \frac{\epsilon_0 \epsilon b(l-c)V^2}{4d} + \frac{1}{2}k_S(L-L_0-\delta)^2 + F_{ext}\delta, \quad (28)$$

Note that both the 3rd and 4th terms are independent of c , the contact point. Following the same procedure as before, the total energy at the equilibrium value of c becomes

$$\begin{aligned} U_T &= \frac{1}{2}k_A l^3 \delta^2 \left(\frac{\epsilon_0 \epsilon b V^2}{6d k_A l^3 \delta^2} \right)^{3/4} - \frac{\epsilon_0 \epsilon b V^2}{4d} \left(l - \left(\frac{6d k_A l^3 \delta^2}{\epsilon_0 \epsilon b V^2} \right)^{1/4} \right) + \frac{1}{2}k_S(L-L_0-\delta)^2 + F_{ext}\delta \\ &= 2(k_A l^3)^{1/4} \left(\frac{\epsilon_0 \epsilon b V^2}{6d} \right)^{3/4} \delta^{1/2} - \frac{\epsilon_0 \epsilon b l V^2}{4d} + \frac{1}{2}k_S(L-L_0-\delta)^2 + F_{ext}\delta, \end{aligned}$$

and minimizing with respect to δ yields an equation analogous to eq. (10)

$$F_{ext} - k_S(L-L_0-\delta) = - \left(\frac{\epsilon_0 \epsilon b k_A l}{6d} \right)^{3/4} \frac{V^{3/2}}{(k_A \delta)^{1/2}}. \quad (29)$$

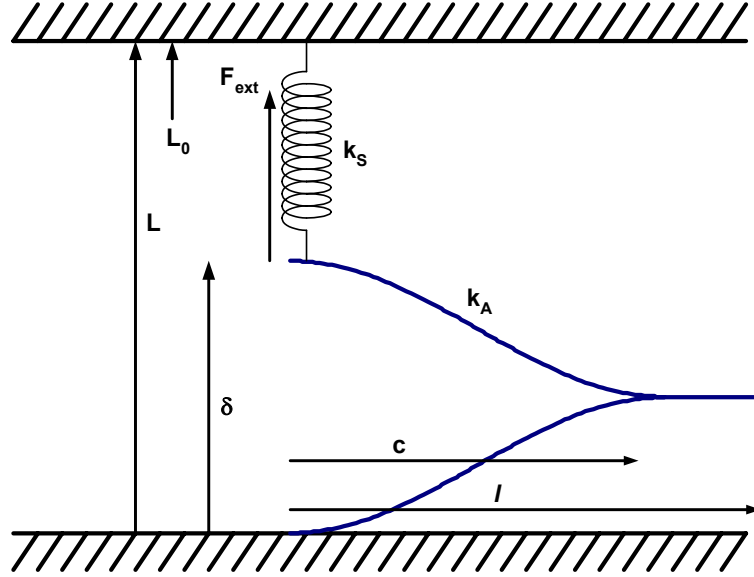


Figure 19. The key parameters of the model. The external spring, k_s , can represent either a real spring-like load or an internal deformation. A constant force F_{ext} is pulling upwards on the actuator. The actuator is pulling down as a spring with spring constant $k_A = Ebt^3/2l^3$, when $V=0$, or as an electromechanical structure when $V>0$. In addition, there is a spring, with spring constant k_S , pulling up on the actuator. The external spring (which really represents the internal deformation) has a rest length L_0 .

The similarity to eq. (10) is obvious and, as always, this reduces to the non-spring solution when $k_s=0$. The external spring term has been kept on the left side of the equation along with the external force.² Since two terms now have a δ dependence, the curve will not look the same as the standard solution. Figure 20 is the new force-displacement graph.³ In contrast to the non-spring solution, the displacement is not zero when the voltage and external force are zero. In this example, the deformation (spring) pulls the resting displacement up to $\sim 150 \mu\text{m}$ (red arrow #1). When the external force is applied (red arrow #2), the displacement increases along the blue line (red arrow #3) to red arrow #4. Note that the slope of the line is larger than the slope of the line in the non-spring case, because there are now two springs acting on the displacement. When the voltage is turned on to a low value, the electromechanical force is again smaller than the mechanical force. Therefore, as before, the displacement is controlled by the purely mechanical behavior and nothing happens. When V reaches 26 V (in this example) the electromechanical

² If the spring represents an internal deformation, then the spring term actually belongs on the right hand side of the equation along with the rest of the electromechanical behavior of the actuator

$$F_{ext} = -\left(\frac{\epsilon_0 \epsilon b k_A l}{6d}\right)^{3/4} \frac{V^{3/2}}{(k_A \delta)^{1/2}} + k_{Deformation} (L - L_0 - \delta) \quad (29a)$$

³ This example assumes an external spring whose spring constant is three times larger than the actuator spring constant. The same behavior is seen for other choices of spring constant, but this one was convenient for the illustration.

and mechanical curves intersect at arrow #4. However, the slope of the electromechanical curve is positive, unlike the curve in the non-spring case. Therefore, if the displacement pulls in a little, the electromechanical force falls back below the external force, and a snap-in does not occur. If the voltage is increased a bit more, the electromechanical curve rises. The displacement begins to decrease along red arrow #5, but it has a stable position at each voltage rather than an unstable snap in. Finally, when the minimum of the electromechanical curve is equal to the external force (at 38 V here) an unstable snap-in occurs along red arrow #6. The displacement vs. voltage is shown in Figure 21. Note that the pull-in begins at a lower voltage than the pull-in without the spring. This is because the total displacement is smaller with the spring than without it.

The external spring results in a soft pull-in. That is, the pull-in occurs gradually up to some final pull-in voltage. The gradual pull-in occurs over a larger voltage range as the external spring constant increases, and pull-in gets sharper as the external spring constant goes to zero. This makes sense intuitively. Note that FEM predicted a slight roll-off of the displacement as the voltage approached V_{PI} , while the original model did not. We can assume the same is true here, so that the real pull-in is even softer than indicated by this model.

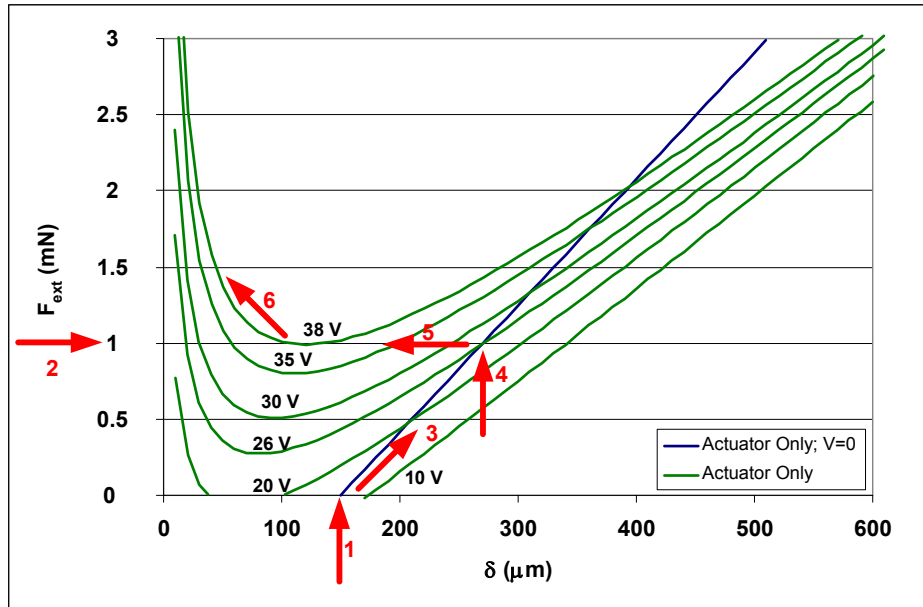


Figure 20. Force versus displacement with an external spring or internal deformation.

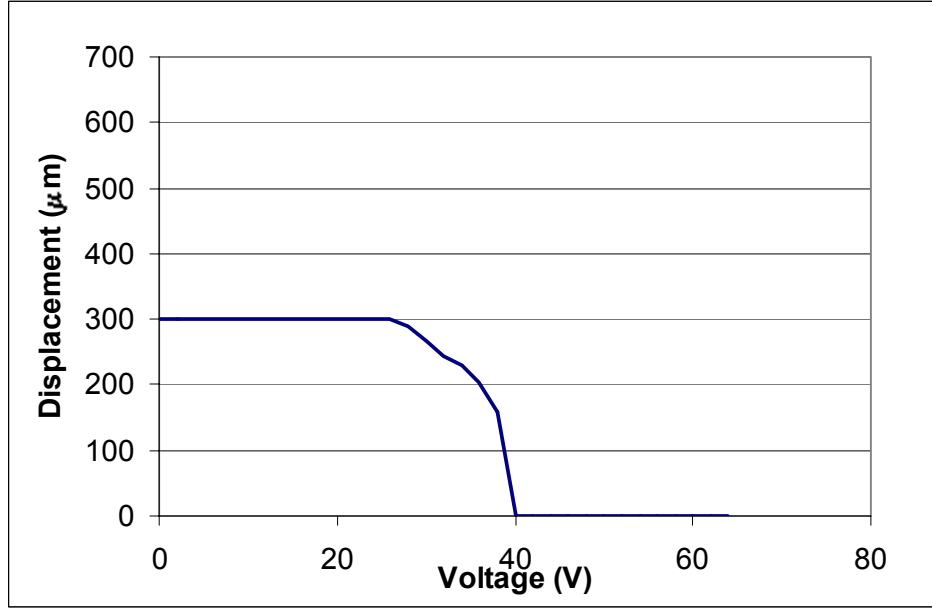


Figure 21. Displacement versus voltage for the case where there is an external spring or internal deformation.

The minimum of the electromechanical curve is at $\partial F / \partial \delta = 0$, which is at

$$\delta_{\min} = \left(\frac{\epsilon_0 \epsilon b k_A l}{6d} \right)^{1/2} \frac{V}{(2k_S^2 k_A)^{1/3}}. \quad (30)$$

If this is plugged back into the force equation, we have the equation for the minimum of the electromechanical curves as a function of voltage.

$$F_{\min} = -\frac{3}{2^{2/3}} \left(\frac{\epsilon_0 \epsilon b k_A l}{6d} \right)^{1/2} \left(\frac{k_S}{k_A} \right)^{1/3} V + k_S (L - L_0) \quad (31)$$

The final, unstable pull-in occurs when $F_{\min} = F_{\text{ext}}$.

$$V_{PI} = (F_{\text{ext}} - k_S (L - L_0)) \frac{2^{2/3}}{3} \left(\frac{6d}{\epsilon_0 \epsilon b k_A l} \right)^{1/2} \left(\frac{k_A}{k_S} \right)^{1/3}. \quad (32)$$

3.3 Process Development and Fabrication

3.3.1 Process Flow and Requirements

This section contains an overview of the process flow. Detailed discussions are contained in the following sections.

The process for making a PolyMEMS actuator is illustrated in Figure 22. A thin polymer sheet is used as the substrate. A planarization step may be required to achieve a smooth enough surface. A thin aluminum film and a thin polymer dielectric are deposited on one surface. These films are patterned, forming the electrodes and leads. Thicker metal is required, in some areas, for robustness and for bonding to an external connection. Next, trenches are etched into the substrate. A polymer adhesive is patterned into the trenches. Finally the structure is cut out of the substrate, folded over onto itself, and bonded together by activating the adhesive (i.e., heating).

Polyimides, such as Kapton (a DuPont trade name) were chosen as the preferred substrate material. The single largest factor in this choice was that polyimide is the most common substrate material used in flexible printed circuit (FPC) manufacturing. It is therefore easily available at a reasonable cost, there is a well developed infrastructure for handling it and fabricating on it, and FPC manufacturers (potential manufacturers of PolyMEMS actuators) are comfortable using it. Polyimide is known for its excellent mechanical properties over a very large temperature range. The primary drawback is its relatively high moisture absorption (typically 3-4%) and surface roughness. The surface roughness is due to the specific chemical formulation and manufacturing methods used and can be partially reduced by an appropriate choice of material. AFM images show widely differing roughness for different Kapton formulations. Surface roughness effectively increases the gap between surfaces, reducing the electrostatic force. As demonstrated by the analytical model, the performance degrades very quickly with this gap.

Aluminum is the preferred electrode metal, due to a property called “self healing.” With a desired thickness of only ~ 100 Å, the importance of a relatively smooth substrate surface is reemphasized.

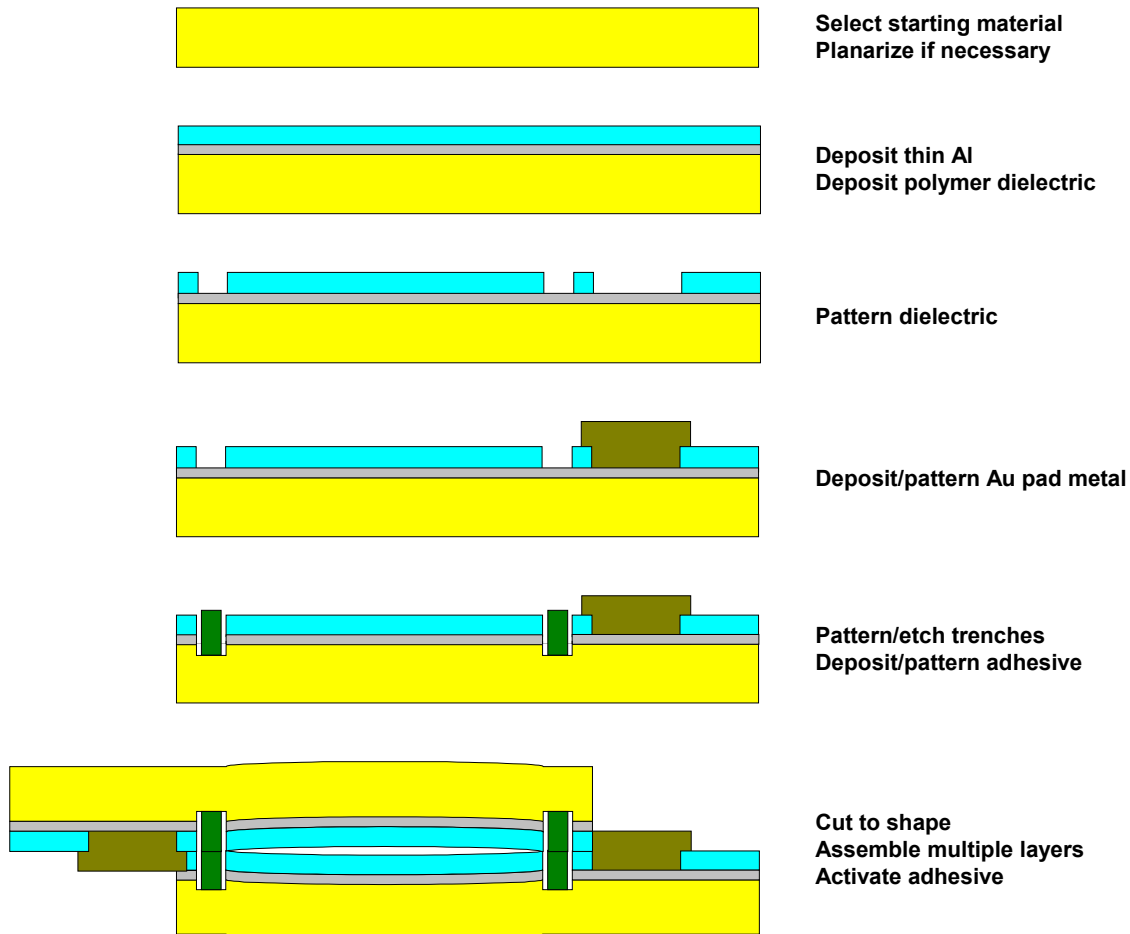


Figure 22. A basic process flow for the PolyMEMS actuator.

The dielectric over the aluminum must be a polymer. Ceramic dielectrics (e.g., Al_2O_3) have Young's moduli so much larger than polymers that even very thin layers will exceed the stiffness of the substrate. Cracking of the brittle ceramic will occur quickly. Thermal expansion mismatches between polymers and ceramics will also result in cracking. The thickness will typically be 0.5-1 μm . Thinner dielectrics require substrate planarization, but films in this range are typically alright without planarization. Although this is not difficult to achieve on silicon wafers, it is not so easy on large polymer sheets where spin coating is not an option. Most techniques for depositing films on polymers involve coating the surface with a liquid. A few ten-thousandths of an inch (2-10 μm) is considered "very thin", and uniform films of this thickness are difficult. Thinner films can be obtained by vapor coating techniques, but the choice of materials is then drastically reduced. On this program we used spin coating techniques, but large area deposition will be required for reasonable manufacturing. To support voltages up to ~ 250 V, the dielectric should have a breakdown strength ≥ 2 MV/cm. It is

desirable to have as high a dielectric constant as possible. Most polymers have dielectric constants less than about 3. A few (Poly Vinylidene diFluoride – PVdF – for example) have higher ϵ , but introduce processing restrictions such as temperature limits. All of the polymer substrates and dielectrics that we investigated could be patterned with an oxygen plasma.

The bonding process was one of the more difficult steps. As shown previously, the process cannot add any gap between the surfaces. The adhesive must be a thin polymer which can be deposited and patterned (without affecting the other polymer layers already on the surface). The polymer preferably should be a thermoplastic material so that it can be activated by heating.⁴ The melting temperature must be low enough that the other polymers are not affected. Finally, the adhesive must be strong, since the highest stresses in the entire structure are concentrated at these joints.

The goal of fabricating PolyMEMS actuators on a flexible circuit line was never realized. During initial preparations for this, it was learned that trace amounts of aluminum – the metal we needed to use for self-healing – is poisonous to the copper plating baths used in flex circuit manufacturing. The flex circuit vendor we were working with was unwilling to risk processing our devices without setting up a dedicated line for all wet chemical steps. Although there is nothing difficult about this, it was beyond the scope of the contract. Therefore, we opted to do all fabrication in our silicon lab, even though that limited the size of the sheet we could process. Our fabrication was done by clamping a Kapton sheet between two stainless steel rings, forming a ~six inch “wafer” (Figure 23). This wafer could be treated just like a silicon wafer. Photolithography on flex circuits uses large Mylar sheets with a high resolution black/clear pattern. These serve the same function as the glass photomasks used in silicon fabrication. Resolution down to about 2 μm can be achieved. The masks can be laid out on a PC using ordinary drawing or CAD software, compared with the more sophisticated software required for silicon masks. The cost of the Mylar masks is only 10-20% of the cost of the glass plates for silicon fabrication.

⁴ Polymers can be divided into two broad classes: thermoplastics and thermosets. Thermoplastics are not crosslinked, so they can melt and reflow repeatedly when heated. Thermosets are crosslinked. Once they cure (i.e., crosslink) they will not melt. They will soften at higher temperatures, but not fully melt.

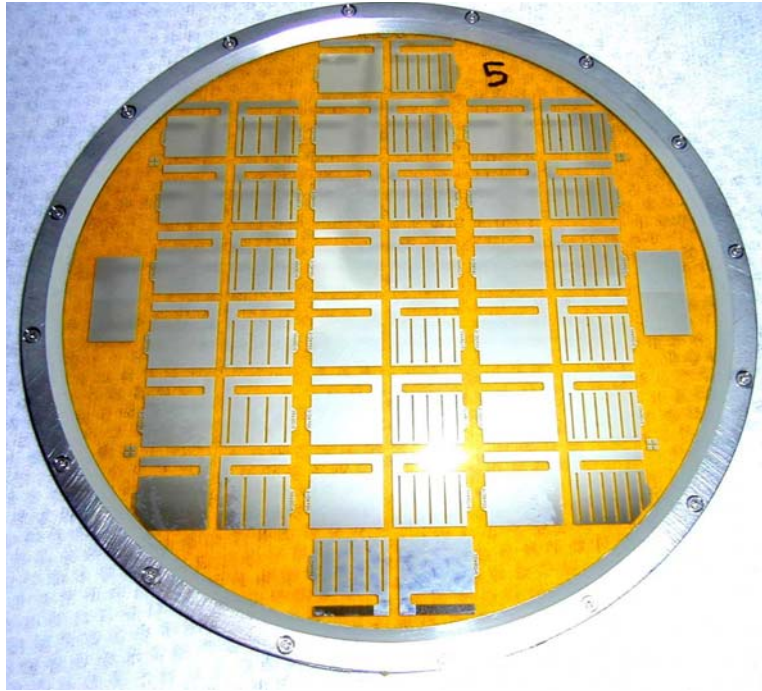


Figure 23. A 6" Kapton "wafer" containing patterned unit cells.

3.3.2 Substrate Materials

The two most commonly used flex circuit materials are polyimide and Mylar. Polyimide was selected because of its high temperature properties, giving us more flexibility in the choice of other materials. DuPont Kapton is available in many varieties (variations in the chemistry, and the thermal and mechanical properties) and in standard thicknesses from 0.3 mil ($\sim 7\ \mu\text{m}$) to 5 mils ($127\ \mu\text{m}$). We typically used 1 mil. All Kapton has surface texture resulting from the drum on which it was cast or from a crystalline additive used to improve handling and rolling, or both. Additional roughness is added intentionally for lamination of copper in FPC manufacturing, but we used the smoother, unlaminated material. The texture is detrimental to electrostatic actuators because it reduces the available force (by increasing the sheet separation) and promotes pinholes and shorts. Figure 24A is an AFM image of a $50\ \mu\text{m}$ square of Kapton HN in its as-received condition. The roughness is obvious. Figure 24B shows the improved smoothness (over an order of magnitude) after coating with a spun-on polyimide film $\sim 1\ \mu\text{m}$ thick. Several other materials (e.g., BCB from Dow Chemical, Avatrel from BFGoodrich, etc.) are available for planarization as well. Planarization was found to be critical when the dielectric thickness was less than about $0.5\ \mu\text{m}$. Above that thickness, the dielectric tended to sufficiently planarize the surface. Figure 25 shows that with a $\sim 0.3\ \mu\text{m}$ dielectric on an unplanarized substrate, the force (calculated from the measured capacitance) is greatly reduced from the expected force. With planarization on the substrate, the force increases.

The substrate is important in two ways. First, it is the mechanical backbone of the actuator. The spring constant of the structure is primarily determined by the substrate dimensions and properties. The analytical model allows us to use this to our advantage. The substrate also can have a detrimental effect if uncompensated charge gets trapped in the material. Trapped charge is common in polymers, and it can generate strong electrostatic fields. The most common manifestation of these fields is stiction, where the two sheets in the unit cell stick strongly even with low or no applied voltage. Since stiction is also strongly influenced by the dielectric, a detailed discussion appears after the section on dielectrics.

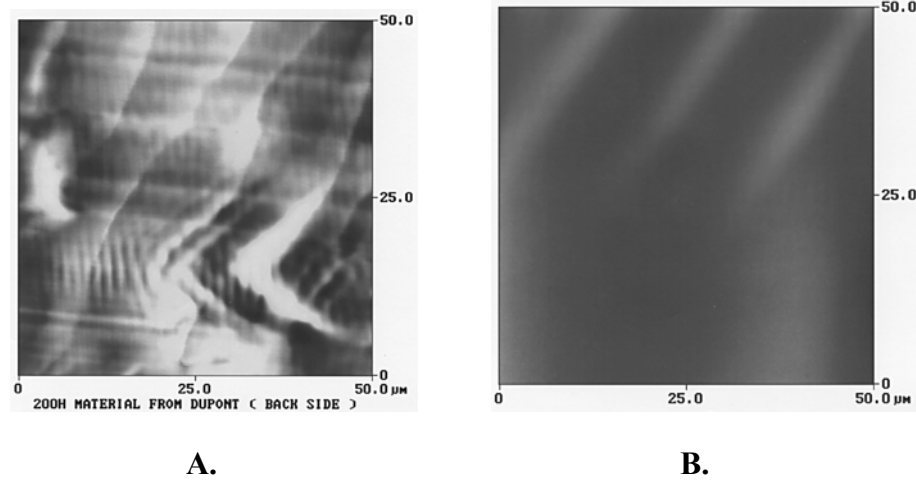


Figure 24. A. A typical AFM image of commercial Kapton. The average roughness is 700 Å (250 Å RMS) with a peak-to-peak well over 2000 Å. B. After planarizing with ~1 μm of polyimide. The average roughness is 60 Å (42 Å RMS) with a peak-to-peak 270 Å.

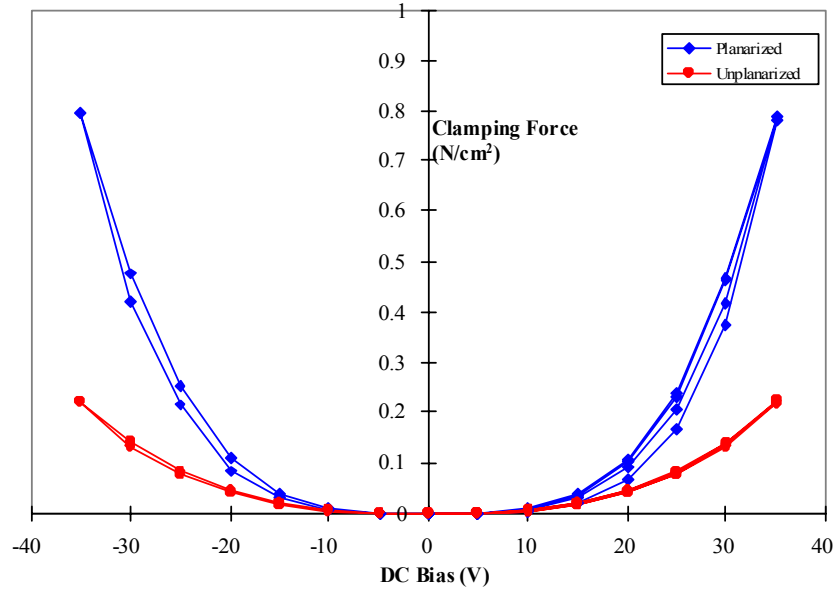


Figure 25. Electrostatic force vs. voltage, for planarized and unplanarized substrates.

3.3.3 Metal, Dielectrics, and Self-Healing

Aluminum is the preferred metal due to a phenomenon known as “self-healing.” A small short, a pinhole for example, between opposing sheets in a unit cell will neutralize that cell. A small discharge will occur when they get very close together. If the metal and thickness are chosen properly, the discharge vaporizes the aluminum in a small area and oxidizes the exposed surface, effectively eliminating the short. This self-healing has been known and used for many years by makers of thin film capacitors. The metal must have a low melting point, must oxidize easily, and the oxide must be nonconductive. Al, Zr, or their alloys are the only metals that fulfill these requirements. Thickness is also critical. If the metal is too thin, the resistance will be too high to sustain the discharge. The short will not vaporize or oxidize completely, leaving a partial short and a useless unit cell. If the metal is too thick, heat from the discharge will be quickly dissipated and the short will again fail to completely burn out. Approximately 100 Å of Al, having a sheet resistance of $\sim 10\text{-}50^\circ\Omega/\text{square}$, is the best combination of material and thickness.

Figures 26 and 27 show the effects of self-healing. To produce the traces in Figure 26, two sheets (substrate, metal, and dielectric) were placed face to face with a voltage applied between the metals. The voltage was swept from 0 V to ~ 30 V several times. In the first few sweeps, current spikes were observed. These are the electrical signature of self-healing discharges. After the discharges stopped, the voltage could be increased. This was repeated until the maximum desired voltage was reached or exceeded. Thin dielectrics ($\sim 0.3\text{ }\mu\text{m}$) typically required a more extensive burn-in than thicker dielectrics ($1\text{ }\mu\text{m}$), most likely because there are more pinholes in the thinner films.

Successful self-healing also requires careful selection of the dielectric. Since the dielectric is a polymer, it burns upon exposure to the discharge. If the burn track leaves carbonized material, a moderate resistance remains between the sheets and the short is not eliminated. Polyimides, varieties of PMMA, and PVdF worked well.

At times we observed a short that did not self heal. One discharge triggered another, leading to a traveling short circuit. Figure 28 shows the final result. This effect has been reported in literature on capacitors. It is claimed that, if too much energy is dissipated through a small self-healing site, damage is done to the adjacent material making it susceptible to further breakdown. The breakdown becomes progressive, culminating in the observed domino effect. Elimination of this problem requires either limiting the amount of energy that is dissipated through any given site, or eliminating the initial discharge. Some capacitors use segmented electrodes, connected by fusible links to accomplish this. Others use careful control of the aluminum thickness and resistivity to slow the rate of energy dissipation. Thicker dielectrics helped the most, by reducing the probability of the initial breakdown.

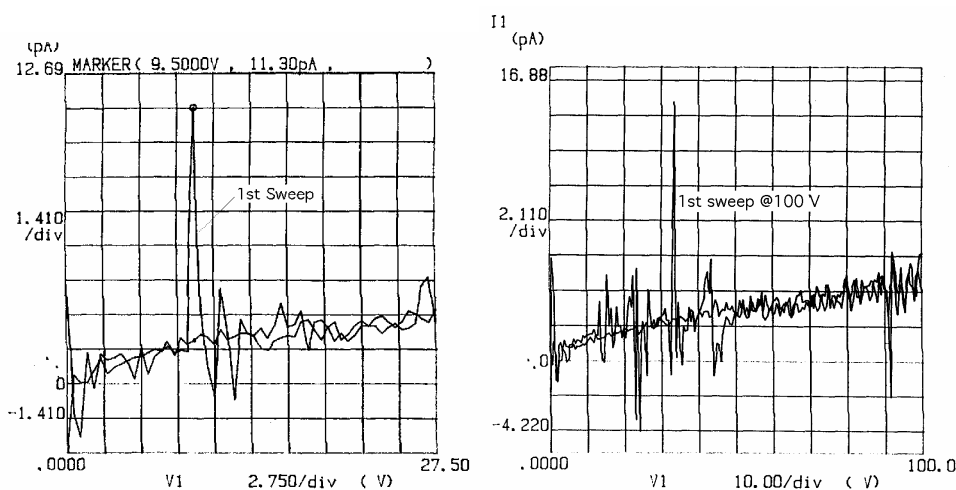


Figure 26. The first two burn-in sweeps on a typical structure. Beginning with a low voltage sweep on the left, self-healing events appear as small current spikes and disappear after one or two sweeps. The maximum is slowly raised until the typical operating voltage is reached or exceeded. After the current spikes disappear, the capacitor has been fully burned-in up to that voltage.

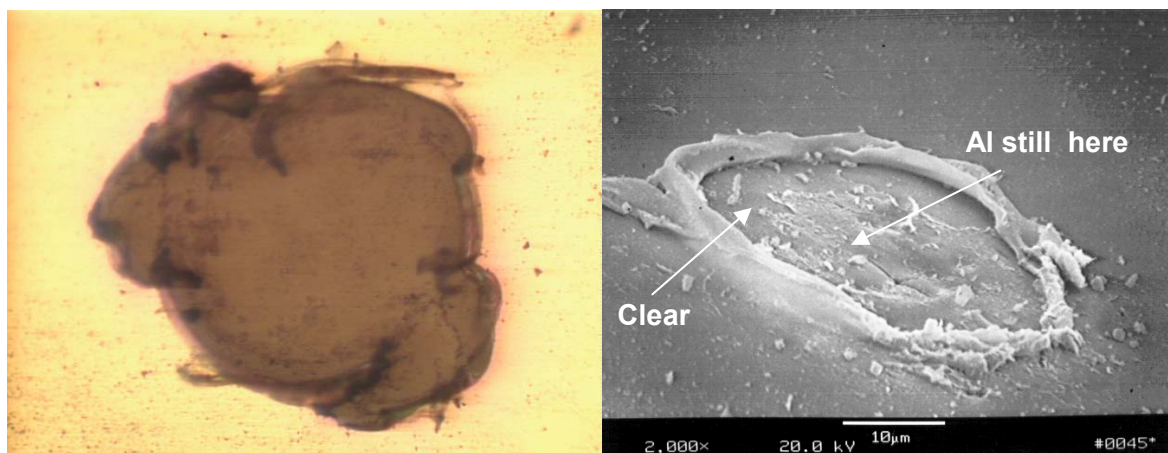


Figure 27. The optical micrograph on the left shows a discharge crater from a self-healing event. The ~ 100 Å Al has been completely vaporized, eliminating the short. The electron micrograph on the right shows a similar crater. In this case, the ~ 300 Å Al was not completely burned away, and the short did not fully disappear.

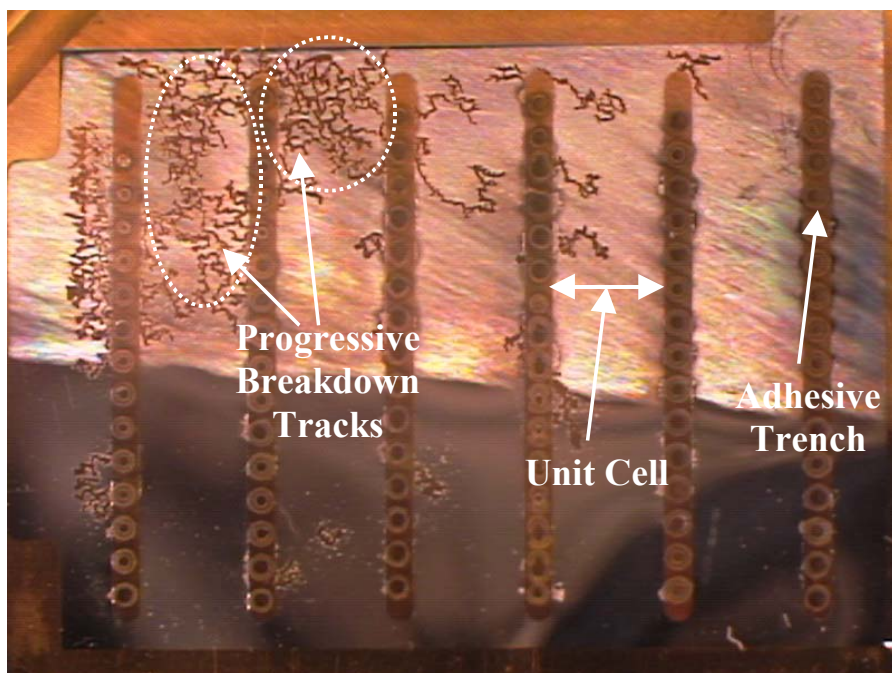


Figure 28. Progressive “domino breakdown” on a device.

Two metalization problems were encountered that were not related to self-healing. The first was delamination of metal at the contact pads. Contact was made to the aluminum using a conductive epoxy. As seen in Figure 29 the epoxy bonds typically peeled off of the Kapton substrate after a small amount of handling. Presumably, the adhesion was poor due to the native oxide on the aluminum film. The contact resistance was high. In addition, discharges often

occurred near the edges of the epoxy, burning out the aluminum and cutting off contact to the rest of the electrode. These problems were solved by adding a $\sim 0.5\text{-}1\text{ }\mu\text{m}$ gold layer above the bond pad. The thicker film resists peeling, has very low contact resistance, and can be soldered.

The second problem was the observation of higher than expected leakage through the dielectric, or breakdown at unusually low voltages. We found that the leaky dielectric appeared only on devices using a polyimide dielectric layer. If two leaky films are placed face to face, the leakage disappears. This indicated that the leakage results from localized defects that do not line up between the two films. The polyimide required a high cure temperature (400°C) compared to the lower temperature (250°C) cure of other dielectrics such as PMGI and PVdF. We have observed the formation of nodules (localized defects) in the thin aluminum films during cures above 350°C . Longer cure times lead to larger nodules and higher leakage, as shown in Figure 30. Thicker dielectrics are helpful, but do not completely eliminate the problem. The simplest solution to this is to use the lower cure dielectrics. Low breakdown occurred in dielectrics of all materials (Polyimide, PMGI, etc.) when they were thin ($0.3\text{-}0.5\text{ }\mu\text{m}$). It was not a problem with thicker films ($>1\text{ }\mu\text{m}$).

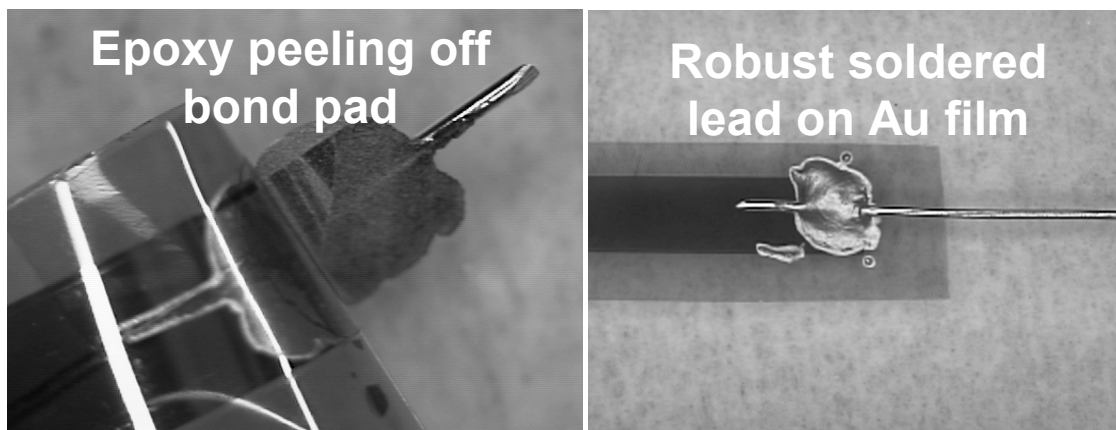


Figure 29. The photo at left shows the aluminum peeling off the Kapton substrate at the bond pad. On the right, a gold reinforcement layer has been added on top of the Al, creating a more robust bond. These held up well to handling and use.

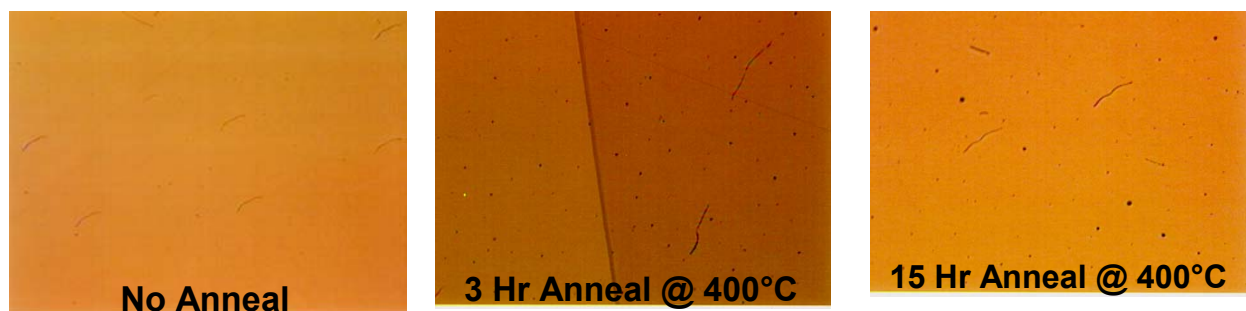


Figure 30. As-deposited aluminum is smooth. Annealing at 400°C creates nodules. A 1 hr anneal (not shown) creates some nodules. A 3 hr anneal creates more and larger ones; and a 15 hr anneal creates even more and larger nodules.

A number of dielectric materials were investigated. The preferred dielectric had to be flexible and have a high breakdown strength. Sputtered Al_2O_3 has been used successfully, on other programs at Honeywell, when the substrate is fairly rigid. In our case, the substrates are quite flexible and Al_2O_3 was not as promising. The ceramic film caused curling of the substrate, cracked, and shorted easily due to the cracking. Polyimide films as thin as 2000 Å - 3000 Å (Dupont PI2613) could be used. The dielectric constant of the polyimide was about 3.5, and loss tangents were low, typically 0.001-0.003. With a proper burn-in procedure the breakdown strength was also found to be very high. Thicker films – on the order of 1 μm – were more robust and were typically used. As with the polyimide substrates, polyimide dielectrics are susceptible to moisture absorption. Polyimide requires a cure temperature of $\sim 400^\circ\text{C}$. As shown in Figure 31, a lower temperature cure results in films with a slight conductance (i.e., non-zero resistance) through their thickness. Thus leakage current is high enough that shorts usually did not self-heal. After a 400°C anneal, the resistance is 10-100 times higher, leakage is lower, and self-healing works well.

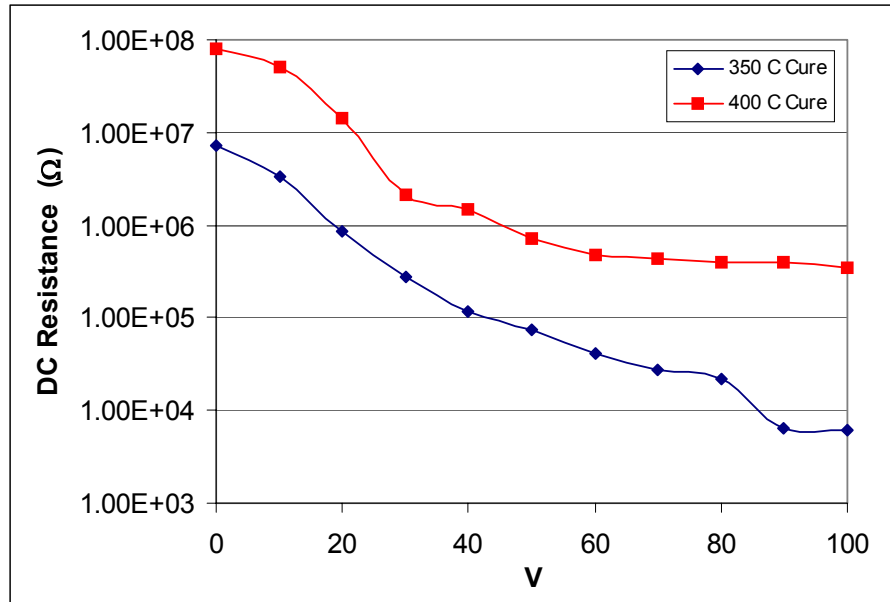


Figure 31. Resistance of a 1 cm² capacitor area having polyimide dielectric. The higher temperature bake results in significantly better resistance and lower leakage.

Acrylate-based polymers are used by some thin-film capacitor manufacturers. **Throughout most of this contract we used PMGI, a semiconductor grade interlevel dielectric which is a variant of poly methyl methacrylate (PMMA).** PMGI has a lower dielectric constant – about 3 – than polyimide, but is less sensitive to humidity and appeared to be less susceptible to charge trapping.

Acrylate-based polymers are also available using a patented “Polymer Multi Layer (PML)” process. PML has been used to make multilayer capacitors (it was originally developed by GE for this purpose), but is most commonly used to create metal/polymer moisture barriers that extend the shelf life of packaged food (e.g., potato chip bags). Acrylate monomers are evaporated onto a rapidly moving web (a “web” is a large roll of polymer sheet that is processed in a roll-to-roll fashion) in a vacuum chamber. The monomer is polymerized by passing through an electron beam curing stage. Film thickness is controlled by the monomer flux and the web speed. Aluminum can be evaporated onto the web in this same process, making it very attractive for PolyMEMS. Unfortunately, in trials with a commercial PML vendor, this process worked poorly with Kapton and not much better with a polyester substrate. Moisture absorbed near the surface of the substrate is rapidly released upon exposure to the electron beam. The sudden vaporization of this moisture creates defects and delamination.

Poly Vinylidene diFluoride (PVdF) is another promising polymer. PVdF is most commonly known for the fact that it can be made piezoelectric by going through a specific treatment. We were not interested in the piezoelectric properties, but in the fact that PVdF-related materials has

a very high dielectric constant – 10 to 12 – compared to other polymers. This high dielectric constant is extremely beneficial for generating large forces at reduced voltages. PVdF is also very cheap. A dielectric constant greater than 10 was easily achieved in our trials. For our purposes it is purchased as a powder. The powder can be dissolved in commonly used solvents like acetone or NMP, and then spun or sprayed onto a polymer sheet. We typically used spinning on this contract. We conducted spraying trials with a manufacturer of spraying equipment and were able to demonstrate deposition of films with the desired thickness. Uniformity of the sprayed coating was poor (local variations of ~10-25% of the thickness), but this could most likely be improved with more development. PVdF is also a fluorine-based polymer and is insensitive to moisture. The biggest disadvantage of PVdF is its low melting temperature. It decomposes (giving off hydrofluoric acid vapor) at ~250°C, and softens enough at ~100°C that two contacting surfaces will fuse together. Thus processing and operation temperatures are limited. This is more of a problem for processing than it is for operation.

3.3.4 Stiction

Throughout the contract, the most frequently observed failure mode was stiction. This is where an actuator would close upon application of the voltage, but would not open back up when the voltage was removed. Visually, the plastic sheets are observed to be tightly held together; small air pockets can be seen very easily. By applying a large external force, the actuator could be pulled back open, but the same thing would happen when it was closed again. Stiction can last for a few minutes, in some cases, but appeared to be more-or-less permanent in most cases. An actuator with stiction is of no value.

The opposite problem is where the actuator will not close, even when the voltage greatly exceeds the pull-in voltage, or it closes but then quickly opens back up. Both of these have been reported by others studying electrostatic actuators, and the problem is known to be related to uncompensated charges on or near the surfaces. For this reason these problems are often related to humidity in the operating environment. An old, but excellent, review of the physics of contact electrification is given by Lowell and Rose-Innes,⁵ and a more recent treatment, more specific to polymer-based MEMS is given by Cabuz, et al.⁶

Because this was observed frequently on fully fabricated actuators, we developed techniques for measuring stiction prior to fabrication. This allowed us to study the phenomenon, and to screen out material that would not produce good actuators.

A simple measurement approach is to place two sheets face to face, as illustrated in Figure 32, and measure capacitance vs. voltage. Initially, the surfaces are only loosely in contact, so the gap is relatively large and the capacitance is small. When a voltage is applied, the electrostatic

⁵ J. Lowell and A. C. Rose-Innes, "Contact Electrification" in *Advances in Physics*, **29**, 947-1023 (1980).

⁶ C. Cabuz, E. I. Cabuz, T. R. Ohnstein, and J. Neus, "High Reliability Touch-Mode Electrostatic Actuators" in the *Proceedings of the Solid State Sensor and Actuator Workshop (Hilton Head '98)*, 8-11 June 1998, p.p. 296-299. Also, Cabuz et al., *Sensors and Actuators*, **A79**, 245-250, (2000).

force pulls the two surfaces into close contact, causing the capacitance to increase as the voltage is increased. At a sufficiently high voltage, the surfaces cannot get any closer and the capacitance stops increasing. This is shown in Figure 33. Normally, when the voltage is decreased, the force decreases and the contact between surfaces decreases. Thus, the capacitance goes back down to its low, starting value. The curve generally shows hysteresis. When V is increasing, the surfaces are separated and the capacitance is low. After the surfaces are pulled together, the force is strong even as the voltage is reduced, due to the close proximity of the surfaces. Therefore, the capacitance does not follow the same path for voltage increasing and voltage decreasing. When stiction is present, the capacitance stays near the highest value. The minimum of the curve is often shifted, indicating the presence of trapped charge somewhere in the system. A nonzero voltage is required to compensate or neutralize the trapped charge. Thus, the minimum field, force, and capacitance occur at a nonzero voltage.

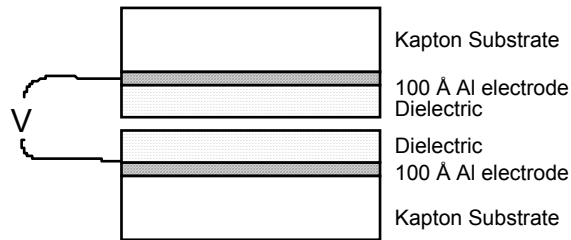


Figure 32. Face-to-face C-V measurements. The electrostatic force pulls the two surfaces close together, causing the capacitance to increase with increasing voltage.

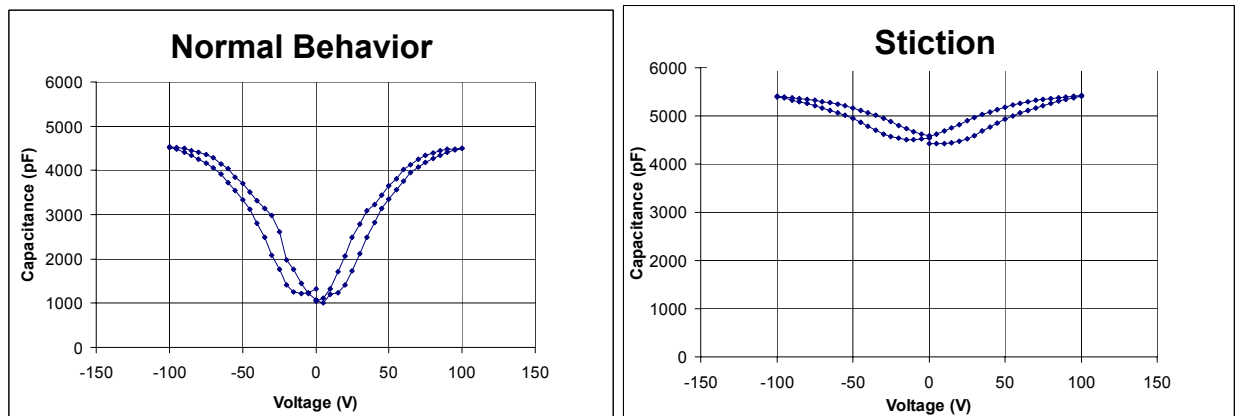


Figure 33. C-V curves showing normal behavior and stiction.

Potential causes of stiction are surface smoothness (i.e., an optical contact), trapped charge in the dielectric layer, trapped charge in the substrate, or any combination of these. By comparing Atomic Force Microscope (AFM) images of various surfaces with their stiction properties, we were able to rule out smoothness as a source of stiction. Examples are shown in Figure 34,

where a moderately smooth surface has high stiction, and Figure 35, where a rough surface still has high stiction.

Since both the substrate and the dielectric are polymers, it is possible for charge to be trapped in both places. This is, in fact, what we observed. The sources and trap locations of the charges differed between substrate and dielectric. Therefore, solutions were found for both types of trapped charge. We will first deal with the charge in the dielectric, and then the charge in the substrate.

3.3.5 Stiction Due to Dielectric Surface Layers

It was found that stiction could be reduced by removing a thin layer of material from the dielectric surface. Figure 36 is a sequence of C-V measurements with a PMGI dielectric before oxygen plasma etching, after plasma etching, and after several heat treatments. The initial test, immediately after fabrication, found very strong stiction. A 10 minute plasma treatment removed ~ 1000 Å from the surface. The C-V curve appears to show complete elimination of the stiction. However, the curve has an odd feature. The normal hysteresis that is seen in these curves is reversed: the curve for increasing voltage is *above* the curve for decreasing voltage. This implies that some kind of residual charging effects are still left at the surface. This is most likely a high density of dangling bonds and/or bound surface charges remaining from the plasma exposure. After baking at the low temperature of 126°C the two curves lie almost on top of each other. A higher temperature bake, at 198°C, restored the normal hysteresis without generating any more stiction. Figure 37 shows C-V measurements before and after removal of ~ 1000 Å of the PMGI surface in photoresist developer. This process is simpler than the plasma and does not require heat treatment. The initial test showed modest stiction, while the final test showed reduced stiction. Note that the stiction was not quite completely removed. AFM measurements did not detect any change in roughness.

Wet etching of PVdF was difficult, and plasma etching was only partially successful. Figure 38 shows a series of C-V curves for PVdF. As before, stiction was reduced after plasma etching and the hysteresis was reversed. The stiction reduction was less dramatic than with PMGI. After the 126°C bake, the hysteresis was less, but was still reversed. Even after the 198°C bake, the hysteresis was still reversed, but the stiction had gotten worse. The implication is that some kind of new surface layer was formed by baking, rather than annealing the material homogeneously through its thickness.

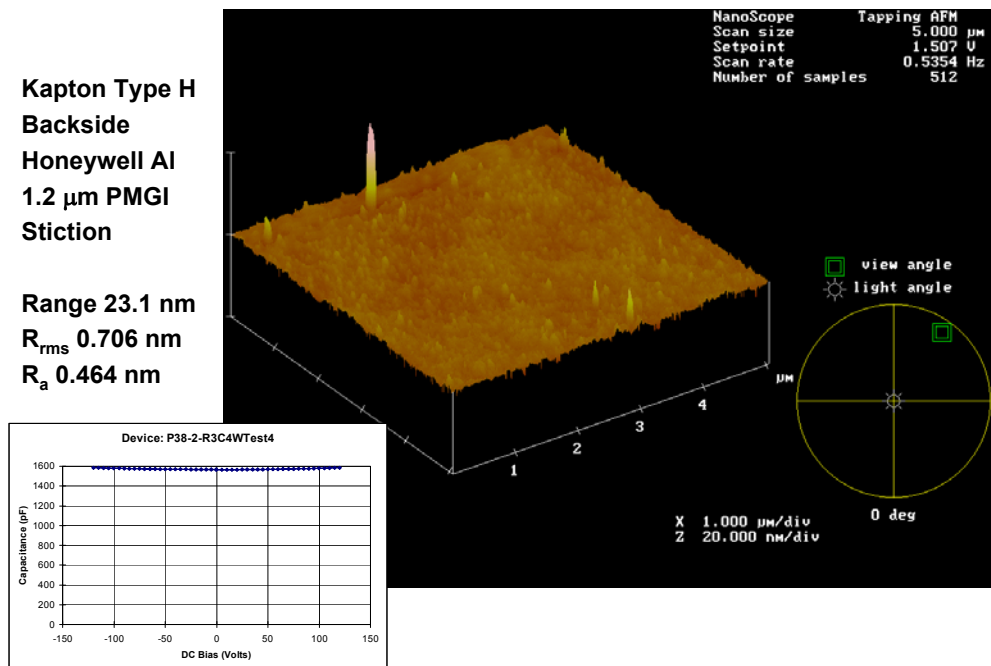


Figure 34. AFM image and C-V curve showing high stiction on a relatively smooth surface, as might be expected for an optical contact.

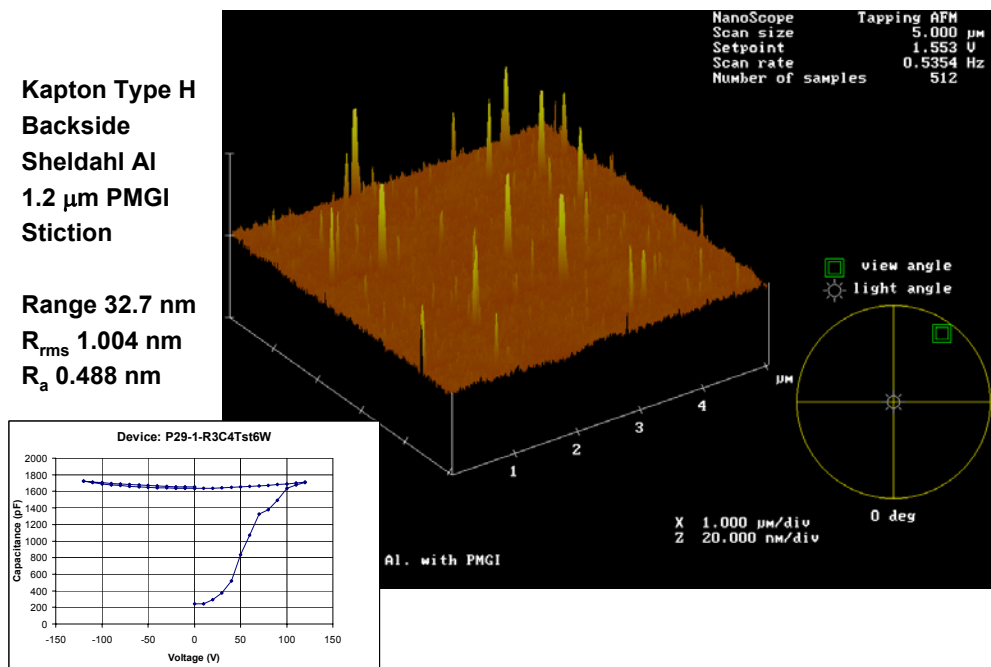


Figure 35. AFM image and C-V curve showing high stiction on a relatively rough surface, opposite of what might be expected for an optical contact.

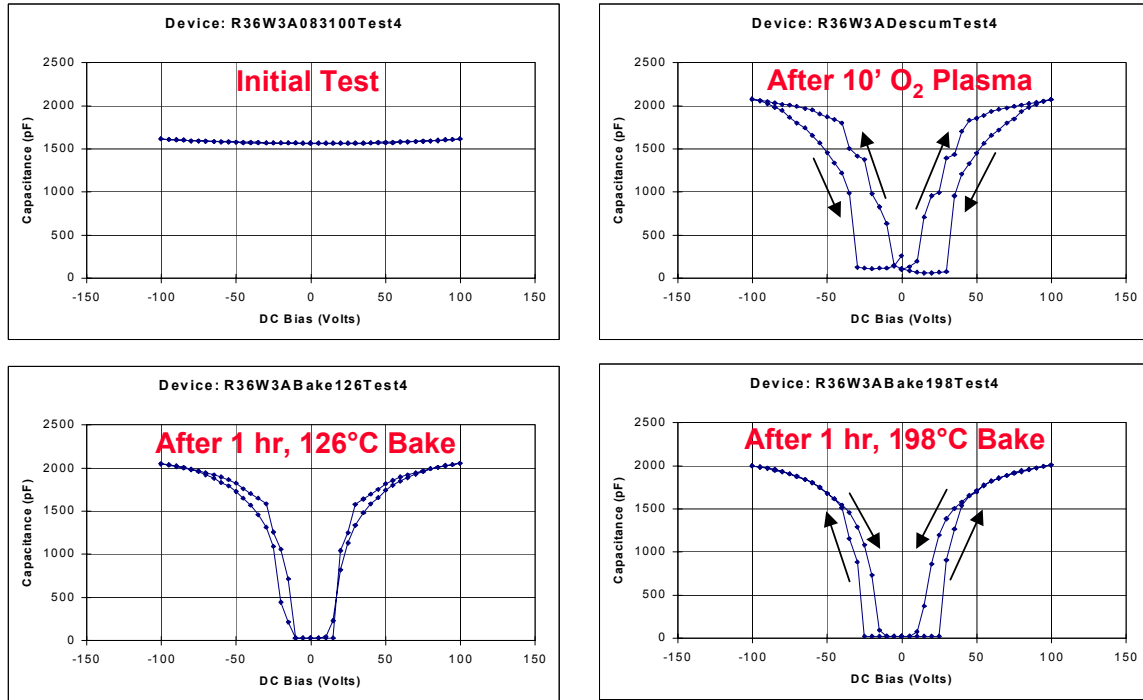


Figure 36. C-V curves before and after removing $\sim 1000 \text{ \AA}$ of the PMGI surface in an O₂ plasma. Removal of the surface layer reduces the stiction, but creates a charged surface layer which can be removed by heating.

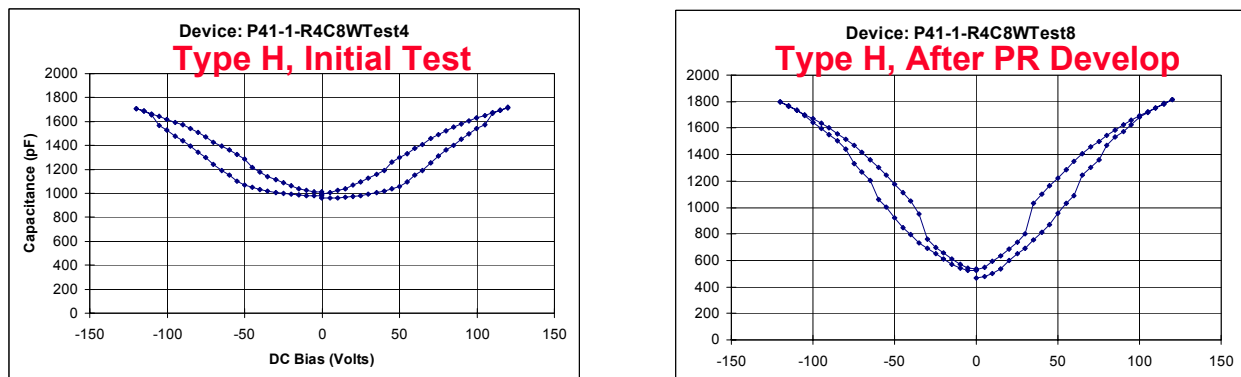


Figure 37. C-V curves before and after removing $\sim 1000 \text{ \AA}$ of the PMGI surface in photoresist developer. Removal of the surface layer reduces the stiction.

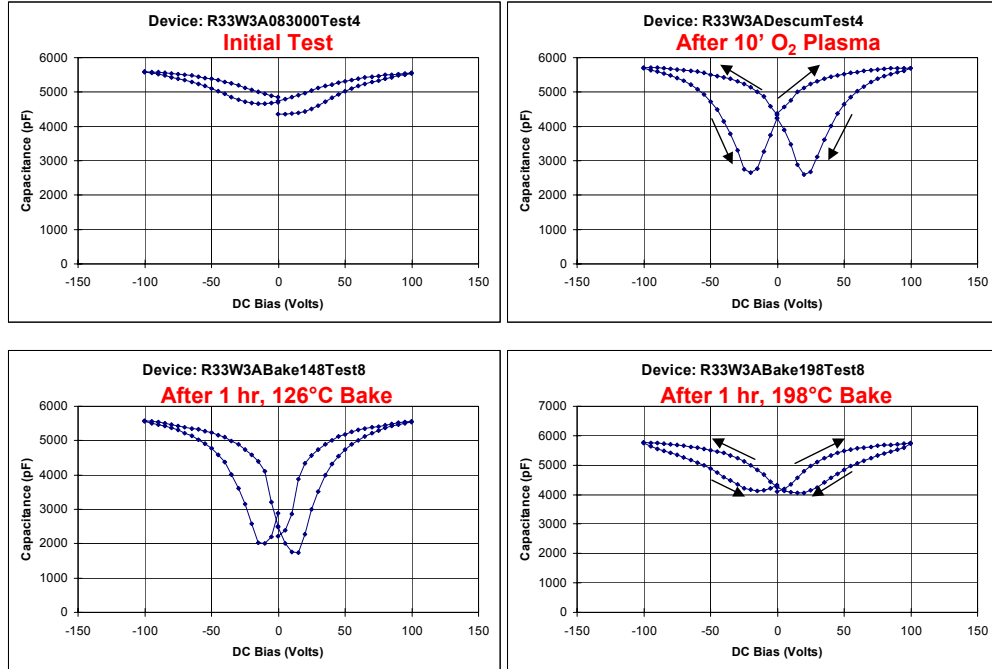


Figure 38. A series of C-V measurements on a PVdF-dielectric device. The initial high stiction was reduced by a 10 minute oxygen plasma, but with reversed hysteresis. A 126°C bake reduced the hysteresis. A 198°C bake yielded high stiction again.

In addition to demonstrating an effective way to eliminate dielectric-related stiction, these experiments helped understand the mechanism behind it. Our model is based on the effects of space charge or dielectric absorption, and surface layers in thin film dielectrics. Space charge, dielectric absorption and soakage are terms commonly used in the capacitor industry to describe the transient buildup and slow release of charge in a dielectric (a very good description, in layman's terms, can be found at www.national.com/rap/Application/0,1570,28,00.html). Our model qualitatively describes equilibrium conditions, where times are long compared to the time constants. Transient effects (times less than or about equal to the time constants) are only qualitatively understood.

We have found a “resistivity diagram,” similar to the band diagrams used to describe semiconductor devices, to be a useful tool in understanding the dielectric effects. The y-axis is resistivity, however, and not energy as in a band diagram. Figure 39 is a plot of resistivity as a function of distance between the metal films for a uniform dielectric material. Although the structure is a capacitor, there is some leakage and, therefore, a finite resistivity. Typically, leakage is small, so the resistivity is high. A layer of charge is present at the interface between the electrode and the dielectric. For all practical purposes, the layers of charge are infinite sheets compared to the thickness of the dielectric. The electric field from these sheets is therefore constant through the thickness (as in the standard derivation of a parallel plate capacitor).

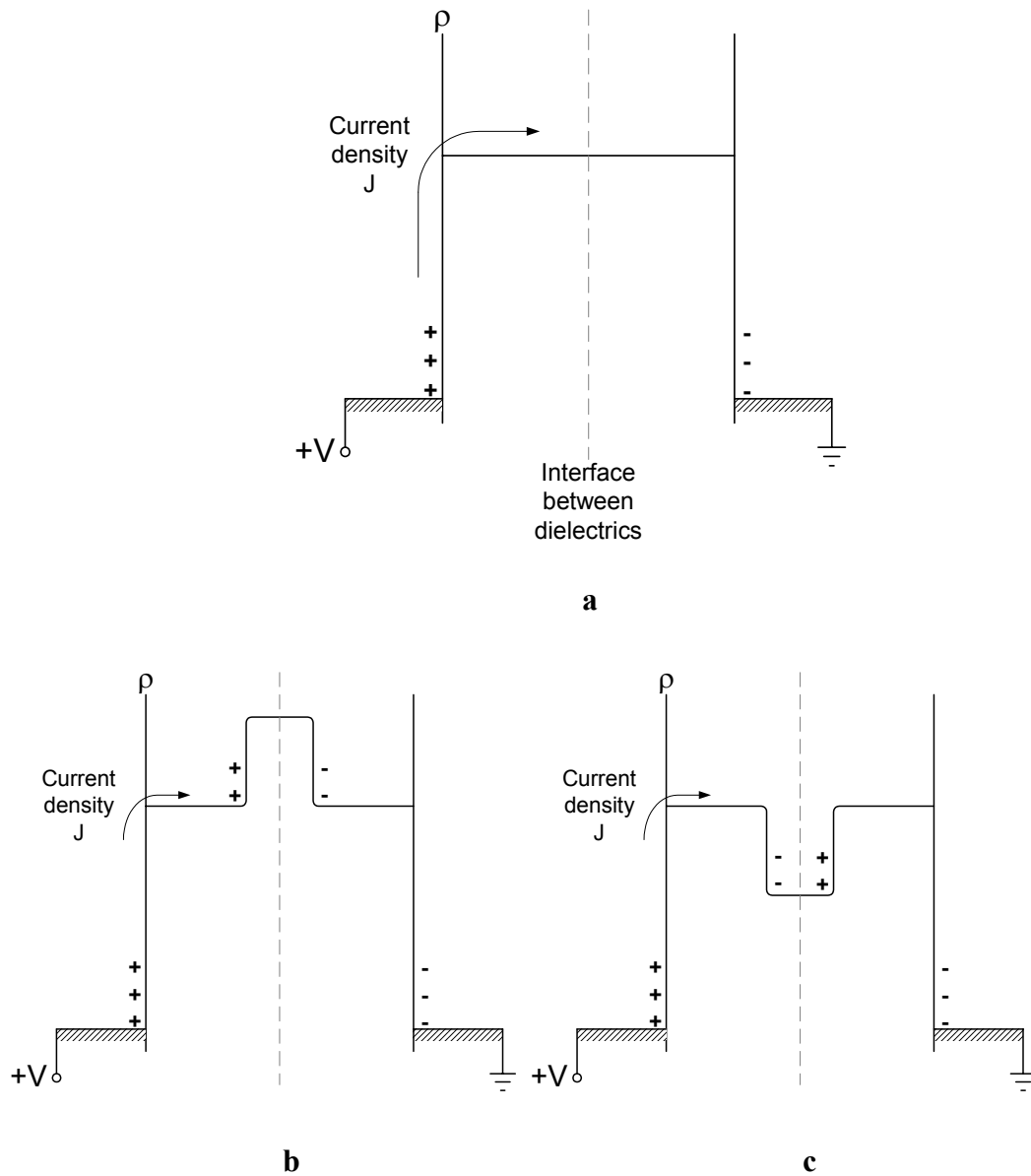


Figure 39. a. A resistivity diagram of a simple capacitor. The capacitor, in our case is formed from the two sheets of Kapton, with the thin aluminum film and the thicker dielectric layer. The interface between the two dielectrics is in the middle of the capacitor. b. A resistivity diagram for a dielectric with a high resistivity surface layer. This configuration produces stiction. c. A resistivity diagram for a dielectric with a low resistivity surface layer. This configuration produces low or no force.

Figure 39b shows the same structure as in Figure 39a, except that now a higher resistivity layer is present near the surface of each dielectric. This can result from, for example, a “skin” forming during the curing process, or from exposure to humidity or other chemicals. Figure 39c shows the same diagram for a structure with a lower resistivity surface layer. Note the layer of charge that is present at the resistivity steps. This is explained as follows.

From the basic equations for electric fields, charges and currents, we have

$$\begin{aligned}\vartheta &= \nabla \cdot D = \frac{\partial D}{\partial x} = \epsilon_o \epsilon \frac{\partial E}{\partial x} \\ &\text{and} \\ J &= \frac{E}{\rho}\end{aligned}\tag{33}$$

where E and D are the electric field and displacement, respectively, ϑ is the density of free charge, ϵ_o is the permittivity of free space, ϵ is the dielectric constant, ρ is the resistivity, and J is the current density. Taking the derivative of the second equation gives

$$\frac{\partial J}{\partial x} = \frac{1}{\rho} \frac{\partial E}{\partial x} - \frac{E}{\rho^2} \frac{\partial \rho}{\partial x}\tag{34}$$

The current density must be uniform throughout the thickness. Therefore, $\partial J / \partial x = 0$ and

$$\frac{\partial E}{\partial x} = \frac{E}{\rho} \frac{\partial \rho}{\partial x} = J \frac{\partial \rho}{\partial x}\tag{35}$$

Therefore, plugging this in to the first equation yields

$$\vartheta = \epsilon_o \epsilon J \frac{\partial \rho}{\partial x}\tag{36}$$

Since ϵ_o , ϵ and J are constants, this equation shows that if the resistivity is constant, then the charge density is zero. But if there is a change in resistivity, there is a nonzero charge density. If the resistivity change is gradual, then the charge density will be distributed over that same thickness range. However, if the resistivity change is sudden then the charge density will be a thin layer of charge. Integrating this equation quantifies the total charge per unit area, Q , at one of the resistivity steps seen in Figure 39.

$$Q = \int \vartheta dx = \epsilon_o \epsilon J \int_{\rho_1}^{\rho_2} d\rho = \epsilon_o \epsilon J (\rho_2 - \rho_1)\tag{37}$$

(An interesting sidelight of this equation is that if $\rho_1 \rightarrow 0$ as in a metal, and ρ_2 is very large as in a dielectric, then $J = E/\rho_2$ and the expression reduces to the equation for a parallel plate capacitor. That is, the equation for a capacitor can be derived from the equations for a resistor!) These equations explain the charges at the resistivity steps indicated in Figures 39b and 39c. Note that these equations are valid under equilibrium conditions. Since the structure is equivalent to a series of capacitors with parallel (leakage) resistances, each layer in the structure contributes a time constant. Therefore, “equilibrium” refers to times longer than the longest of these time constants, which can be on the order of many seconds.

These equations and diagrams can now be interpreted qualitatively. In Figure 39a, the system is a simple capacitor, and nothing unusual occurs. In Figure 39b, there is a charge buildup at the high resistivity layer near the surface. This charge is of the same sign as the charge on the electrode. Therefore, there is an unusually strong attractive force between the two sheets. When the voltage is turned off, the charge buildup bleeds off very slowly (this is dielectric absorption) and the attractive force remains, producing stiction. In Figure 39c, the low resistivity layer produces a sheet of charge opposite to that on the electrodes. This charge screens the electrode charge, weakening or eliminating the attractive force between plates. ***Thus a low resistivity surface layer results in the low/no force failure mode while a high resistivity layer results in stiction.*** Multiple surface layers are also possible, producing odd behavior that can be understood in part. A better understanding of the time dependence is needed for a complete explanation.

Since both stiction and low/no force are explained by a poorly controlled surface layer, it is obvious why removal of the layer had an effect. The reversed hysteresis observed after plasma etching implies a three layer model in each dielectric layer, as in Figure 40. The low resistivity layer, which we surmised was due to plasma damage, is probably only a few monolayers thick. As suspected, the increased stiction after baking PVdF is probably due to a new, high resistivity layer building up during the bake. PMGI did not exhibit this behavior, probably because it is a higher temperature material than PVdF.

These diagrams explain the onset of stiction, but cannot explain the long duration. Each layer of the dielectric can be modeled as a capacitor. Leakage is modeled by a resistor in parallel with each capacitor (Figure 41). The capacitor-resistor pairs create several time constants in the system, one time constant for each R-C pair. There is one time constant for each R-C pair, but the values are combinations of all the R's and C's (the derivation is straightforward, but very messy and not instructive). For reasonable resistances and capacitances, these time constants can be minutes or even a few hours, but not permanent. Therefore, there must be something else taking place to make the stiction last so long. Our assumption is that when charge builds up and resides at the resistivity steps, it has a higher probability of being trapped at those locations. Therefore, when the voltage is removed some of the charge buildup dissipates away, but some remains locked in place. Therefore the stiction remains much longer than might otherwise be expected. We have some evidence that this explanation is indeed correct. That evidence comes from charge trapped in the substrate, so it will be discussed in the following section.

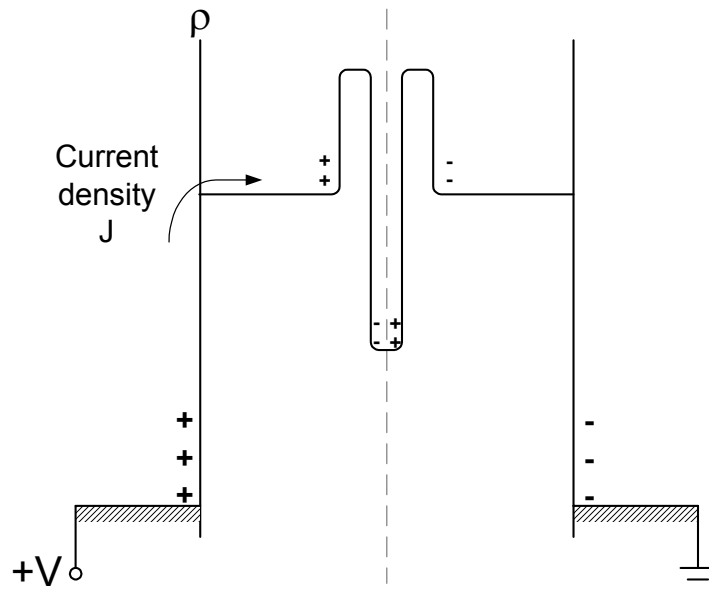


Figure 40. A resistivity diagram for the dielectric after O_2 plasma etching. Plasma etching thins the high resistivity layer, reducing stiction, but creates a very thin, low resistivity layer on the surface. The combination requires an understanding of the time constants involved in the total structure.

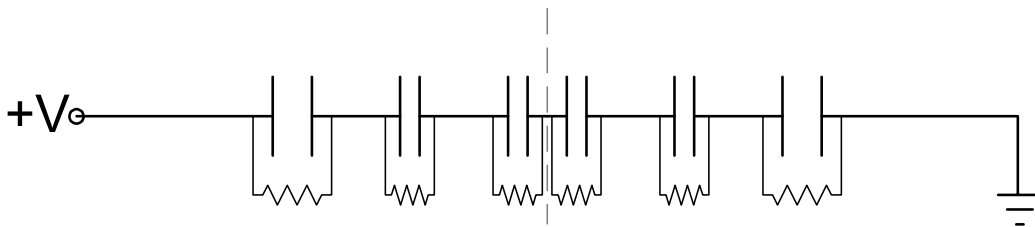


Figure 41. An equivalent circuit for the resistivity diagram of Figure 40.

Nonequilibrium effects are also due to the fact that there are time constants throughout the system. Measurement times (for example, the time between voltage steps in the C-V measurements) that are short compared to the time constants result in nonequilibrium results. To see this we measured C-V curves with a brief time delay added before measuring the capacitance. The stiction and hysteresis changed as a function of this delay time over a period of about 10-20 seconds (on the device we measured). The data imply one time constant of ~ 5 sec. for the combined high and low resistivity layers (there are two time constants for this combined system – the other one will be longer). The derivation of this is again relatively straightforward,

but messy and not instructive. Modeling with programs like SPICE would provide better insight. However, this was not critical to the contract, so we did not pursue this further.

3.3.6 Stiction Due to the Substrate

Even after removing surface layers, baking, etc. we still observed stiction. In some cases the stiction was very strong, and in others not so strong. After some time, it became evident that the key differentiator between these devices was the substrate. We used two different varieties of Kapton from several different sources. Kapton Type H and Type HN have the same chemical structure. Type HN is impregnated with a crystalline “slip additive filler” of dicalcium phosphate that improves handling of large rolls.⁷ The filler creates bumps, up to $\sim 0.2\text{ }\mu\text{m}$ high, on the Type HN surface. As long as the dielectric is $\sim 1\text{ }\mu\text{m}$ thick these bumps get planarized. Type HN material always had low to only moderate levels of stiction. Type H always had moderate to high stiction. Some of our Type H material was purchased with the Al film already applied in a web coating process. This material, which had gone through additional web processing, had particularly high stiction in all cases. As with the dielectric layers, the stiction is most likely related to trapped charge. Stiction is reduced in Type H devices if a polyimide dielectric is used. This dielectric is cured at a high temperature (400°C) which, perhaps, allows static charge in the Kapton substrate to migrate and be neutralized. There were three issues to deal with: 1) what was causing the stiction, 2) how could it be eliminated, and 3) why does charge in the substrate affect the electrostatic field between the metal films.

The third question must be answered first. Figure 42 shows the capacitor structure, including the substrate. The capacitor is formed from the metal layers and the dielectric layers, including the high and/or low resistivity surface layers. As long as the metal layers are connected to ground or an electrical power supply, they should not be affected by charges outside the metal. Therefore, the substrate should have no effect on the fields inside the capacitor. This is clearly not what we observe. A field from the substrate charge clearly penetrates into the capacitor. This could be due to the metal being very thin, or to some kind of pinhole. Figure 43 shows several types of pinholes that would allow a field to penetrate into the capacitor. If actual pinholes existed in the metal, a field could penetrate. If the pinholes were filled with oxidized aluminum the field could also penetrate. Finally, if the pinholes were filled with metallic Al, but these “islands” were electrically isolated from the surrounding Al by nonconducting, oxidized grain boundaries, then a field could again penetrate. Given that the Al layer is only $\sim 10^2\text{ }\text{\AA}$ thick on a substrate with roughness on the order of $10^2\text{--}10^3\text{ }\text{\AA}$, all three of these scenarios are possible.

⁷ When smooth webs, like Kapton Type H, are rolled up, air bubbles are trapped between sheets and the roll looks and handles poorly. The filler in Type HN is a powder that produces microscopic voids between the sheets in the roll. These voids are able to accommodate the trapped air and eliminate bubbles. Since the thickness of typical adhesives and metals in flexible circuits and most other applications is many microns, and the roughness is on the order of $0.1\text{ }\mu\text{m}$, the roughness is not a problem. In our case however, the added films can be the same thickness – and sometimes thinner – than the roughness.

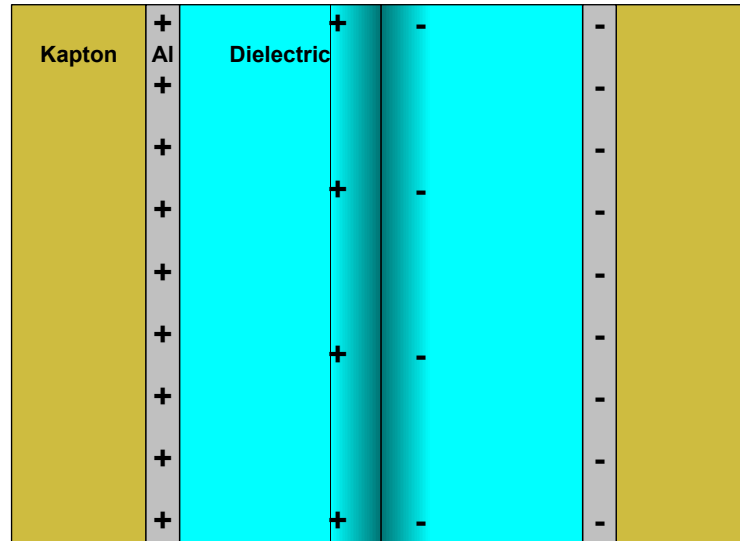


Figure 42. A diagram showing the metal, the dielectric with a surface layer, and the substrate. When the metal is connected

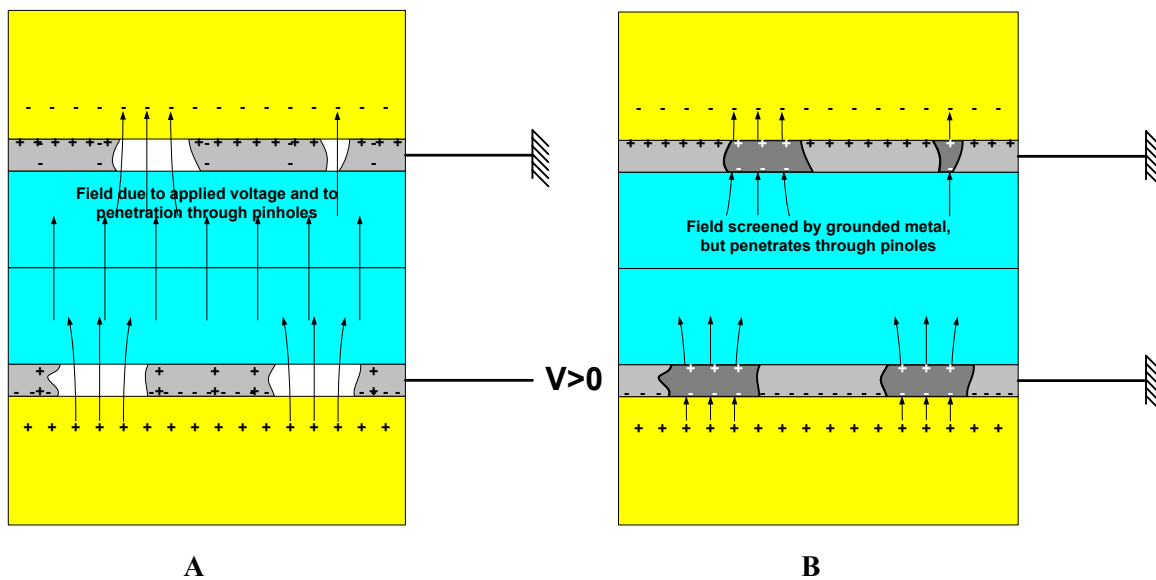


Figure 43. Two types of pinholes that would allow an electric field from the substrate charge to penetrate into the capacitor. A is actual pinholes in the metal (Alternately, this could be areas of oxidized metal. Other than a different ϵ in that region, the effect will be the same). B shows metallic islands which are electrically isolated from the surrounding metal by nonconducting, oxidized grain boundaries.

Standard theories on charging of materials usually assume the charge is on the surface and is moderately mobile. Solutions for electrostatic discharge, for example, all make this assumption.

We have verified that the charge responsible for the observed behavior is not merely surface charge. An air ionizer was positioned near devices during some measurements, and removed during others. There was no change in the behavior. Surface charge would have been easily neutralized by the ionizer.

The trapped charge must be in the bulk of the substrate. Furthermore, when current flows through the material the trapped charge is not dissipated. Although the leakage currents are small (typically a few nA) they should be sufficient to neutralize any trapped charge in seconds. Therefore, the charge must be trapped in localized areas and the current path must not intersect these local trap sites. Figure 44 is an attempt to explain the observations. Polymers are long chains formed by repeating a basic monomer molecule. The bonds along the chain are strong (often covalent) and those between chains are weak. Charge probably flows primarily along the chains. Side groups – molecules attached to the polymer base molecule, but not along the chain – would not participate in charge movement. Therefore, if an atom on one of these side groups is ionized it is less likely to be neutralized by other passing charges. An energy barrier would exist between the trap site and the current path. Baking experiments have helped quantify this. We have shown that the charge in the substrate can be removed by baking. For polyimides like Kapton, the temperature must be at or above 400°C for complete charge dissipation. A temperature of 400°C or higher implies that this barrier has a height of $\sim kT = 0.06$ eV. Furthermore, we have seen that the more web processing (processing of large rolls of plastic) a particular supply of Kapton has been through, the more trapped charge there is. The sliding of polymer sheets over rollers and other polymers can create high electrostatic potentials. If charge was injected into a 25 μm thick Kapton sheet, over an 0.06 eV energy barrier, the potential must have been ~ 3 kV. This is easily within the range of voltages that can be generated by friction.

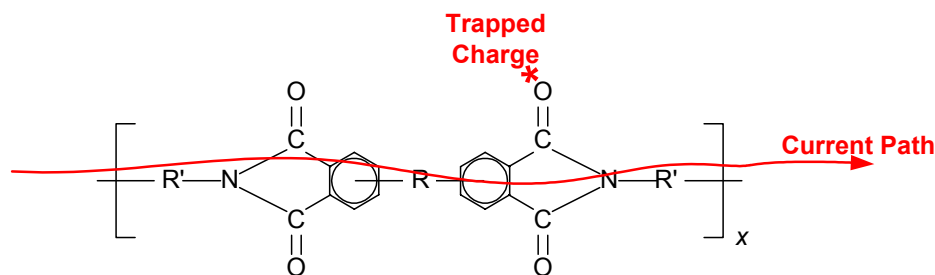


Figure 44. The base molecule of polyimide. Assuming that current passes long the chain and charge is trapped on side groups may explain our substrate charging observations.

Baking of the substrate is therefore a possible way to eliminate trapped charge. The Type H Kapton would have been preferred because it had Al already deposited on it. The deposition process, however, was the source of the friction and charge buildup. Therefore, for demonstration of the PolyMEMS actuator concept on this contract it was easiest to use the Type HN Kapton without the metalization, even though this meant depositing our own metal and using

slightly thicker dielectrics. We could consistently yield low stiction devices by using material from the proper Kapton rolls.

3.3.7 Cutting Structures Out of the Substrate

At some point in the process the structure has to be cut out of the substrate sheet. In flexible circuit manufacturing this is usually done using a die that punches the desired shape out. The die is a wood or metal block with a razor sharp, curved, knife embedded in the surface. Each shape requires a new die. There are limits to how small the radius of curvature can be for these die, and the PolyMEMS structures typically were beyond these limits. Therefore, we used laser cutting. Both IR and UV laser cutting systems were used. UV lasers produced less debris, but some cleaning was required after either. If the dielectric had sufficient stress it could cause curling of the structure. This is unwanted since it adds mechanical stiffness in directions other than the operational direction. Breaking a long cut into a series of short lines or holes (Figure 45) produced clean, flat cuts.



Figure 45. Long slits cut in a polymer sheet, showing the distortion near the slit edges. Rows of laser-cut holes eliminate the distortion. These devices were assembled using the technique shown in Figure 47A, appropriate for single layer actuators.

3.3.8 Assembly and Bonding

The final step in the process is taking multiple sheets of patterned polymer and bonding them together to form the array. As shown previously, the bond must not add any gap between the electrode surfaces. Thickness control is not so critical on the back sides of the substrate (see Figure 46) since there are no electrostatic forces working there. Three different bonding approaches, shown in Figure 47, were studied. The first involved simply placing tape or glue over the cuts in one layer so that it contacted the other layer. This crude approach was suitable for demonstrating single unit cells, but cannot be scaled to larger arrays. In the second approach, which we used most, adhesive is deposited and patterned into a trench in the substrate. The trench and adhesive dimensions are chosen to eliminate the gap. The third approach was demonstrated to work, but is more complicated and was not used much. Each sheet is actually three laminated layers of material. The outer layers are Kapton and the central layer is a sheet adhesive. The adhesive is exposed locally. During the bonding process, the adhesive flows enough to contact and bond to the adjacent sheet. This approach may have advantages in certain circumstances.

In both of these approaches the adhesive must be a thermoplastic. That is, it can be heated up to a point where it will either melt or soften enough to flow a little. The greatest difficulty is that it has to be patternable. Typical methods of patterning will either remove all of the adhesive or will attack the dielectric layers. This is one advantage of the trilayer approach – the adhesive is a sheet and needs no patterning. Although not perfect, we found common photoresist to be an adequate adhesive. The great advantage of PR is that it is easily patterned by photolithography, unlike most other adhesives. For this contract, PR had sufficient strength. It is likely that another adhesive will be needed however. PR may not be strong enough for some applications, and it may not stand up to some environments. Figure 48 shows a photoresist bond line in a trench before and after bonding. Before bonding, the PR is narrower than the trench but is thicker than the trench depth. The volume of the PR line (length times width times height) is slightly less than the volume of the trench (length times width times depth). After alignment the PR lines on opposing sheets come into contact. When the PR is then heated above $\sim 130^{\circ}\text{C}$, it melts and flows, filling the trench without overflowing. Since the initial volume of PR is less than the trench volume, the surfaces of the sheets are pulled into intimate contact without and gap.

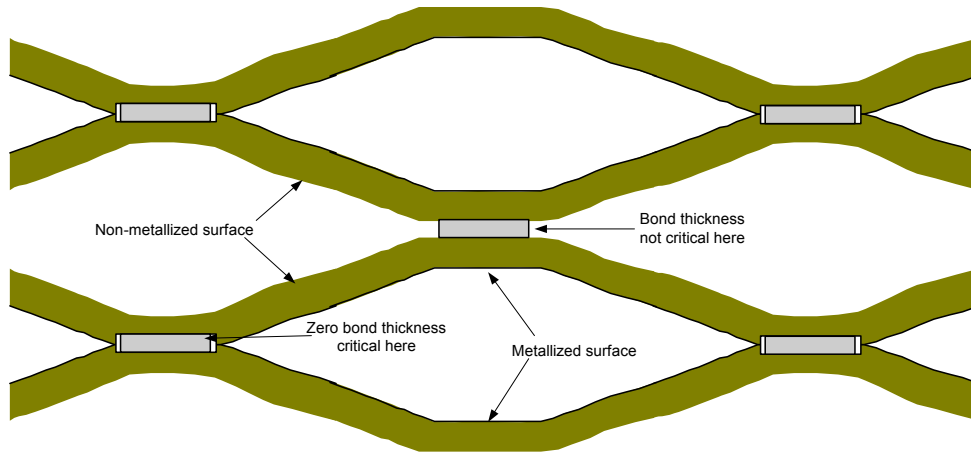
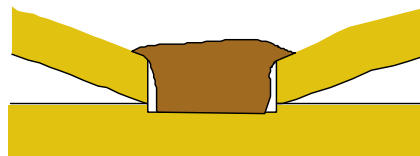
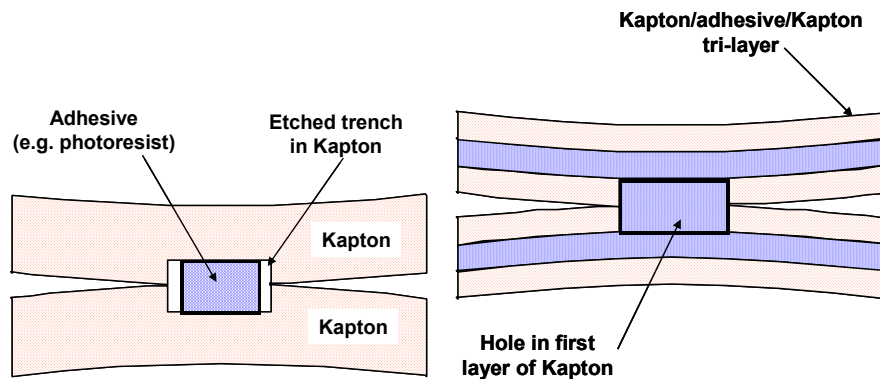


Figure 46. Conceptual sketch of the two bond regions.



A.



B.

C.

Figure 47. Three different bonding methods. A. Tape or glue extruded through slots in one sheet bonds with the opposite sheet. In B, adhesive is deposited in a trench to guarantee that no extra gap results from this step. In C, a central, adhesive layer is exposed locally for bonding.

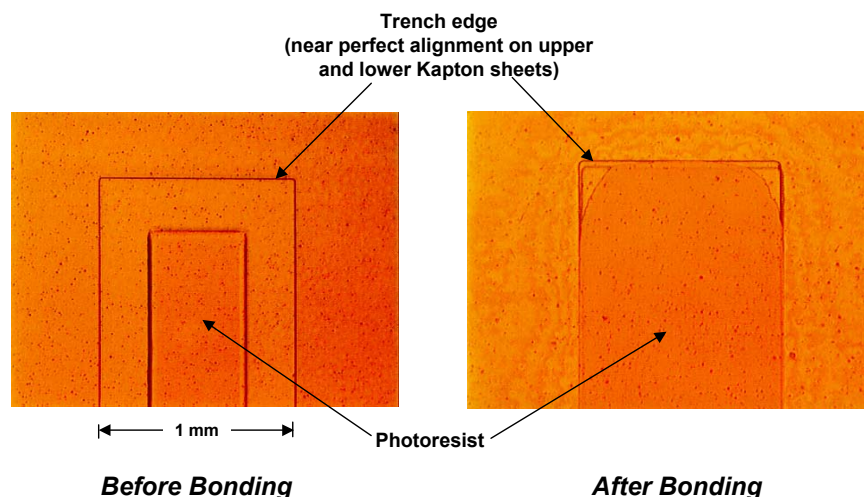


Figure 48. Photographs of a trench, with photoresist adhesive, before and after bonding. Excellent alignment between sheets was achieved. The PR flowed to fill the majority of the trench without spreading beyond the edges.

The early actuators were one, two or three layers of unit cells, and were made using the bonding technique of Figure 47A. Since they were assembled by hand, it became difficult to build devices with more layers. Devices with large numbers of layers required a batch or bonding process. Folding is a process that cannot be applied to silicon, but can be used in plastics. As shown in Figure 49, individual layers are laid out on the mask as usual, but are connected by thin bridges. After fabrication, the entire row of cells is cut and folded in an alignment fixture. Pressure and heat activates the adhesive, bonding all layers together at once. Electrical interconnects can be patterned onto the bridges, significantly reducing the complexity of making contact to the layers. Figure 50 shows the complete assembly sequence of the final actuator design.

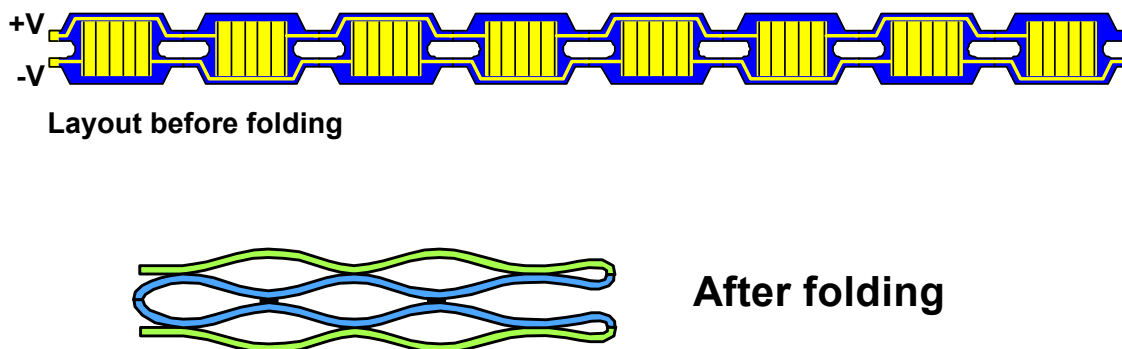


Figure 49. The top drawing shows the structure as laid out on the wafer. Two adjacent units form a layer of unit cells. After folding in an alignment fixture, heat and pressure are applied to activate

the adhesive. The result is the folded structure in the bottom drawing. Only one set of interconnects is required.

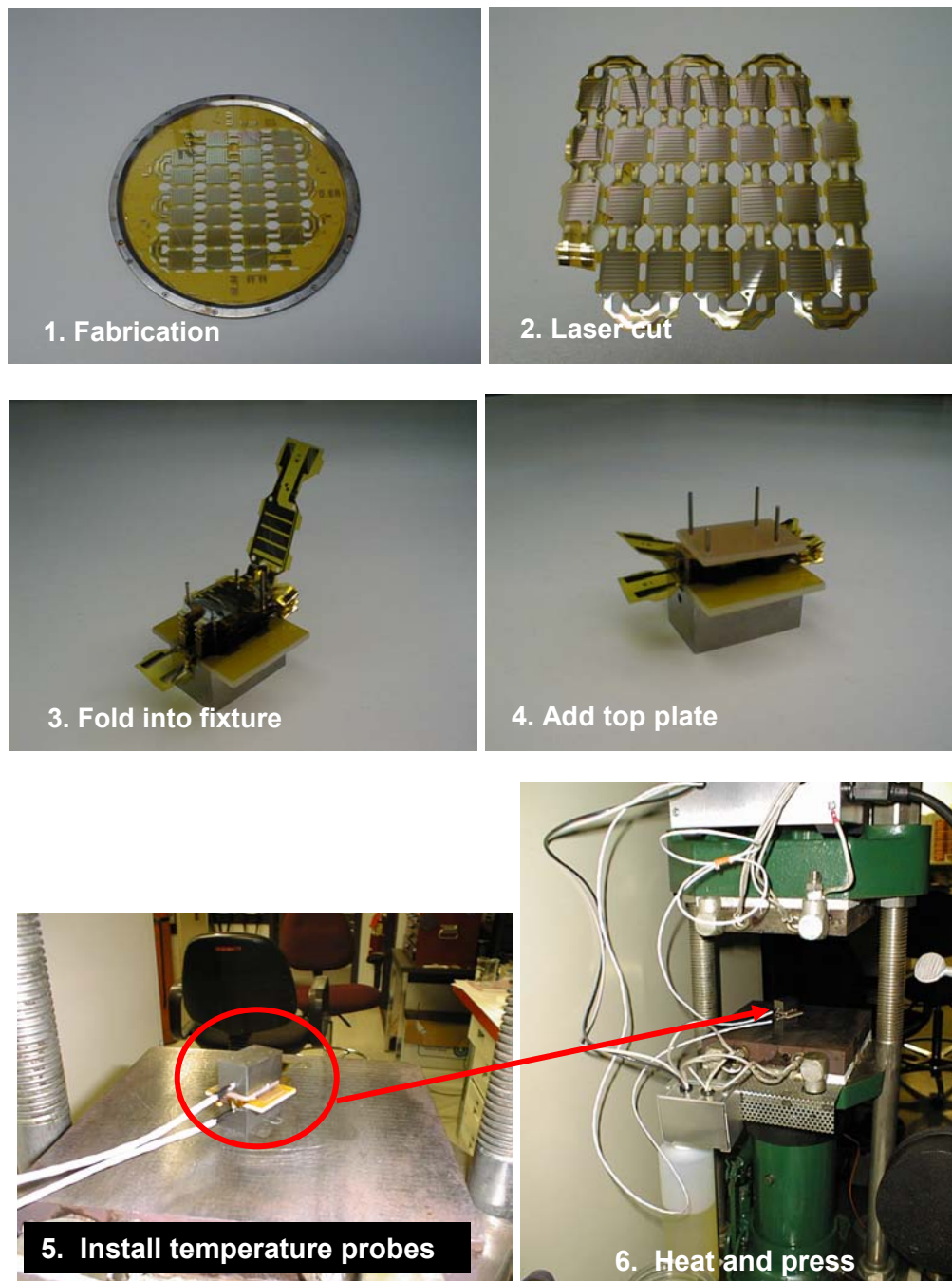


Figure 50. A sequence of photos showing the assembly process of the folded actuator. 1. Actuator features, including the adhesive, are patterned onto a Kapton “wafer.” The features are cut out of the wafer using a UV laser cutting system, but small bridges hold the structure in the wafer. 2. The bridges are cut, releasing the actuator from the wafer. 3. Alignment holes in the structure are

threaded onto pins in a specially built alignment jig. 4. A top cover plate is added to the stack, followed by the top block in the jig. 5&6. The jig is installed in a heated press which melts the adhesive allowing it to reflow and bond all surfaces together simultaneously.

3.3.9 Actuator Characterization

Testing was done in two ways. Electrically, the primary tool was C-V measurements, which have already been described. A test system was built for mechanical and electromechanical testing. The system consists of a base for mounting actuators, an adjustable lever for applying a constant force, a laser displacement sensor, and an 8 channel power supply. A video camera allowed visual observation of the actuator.

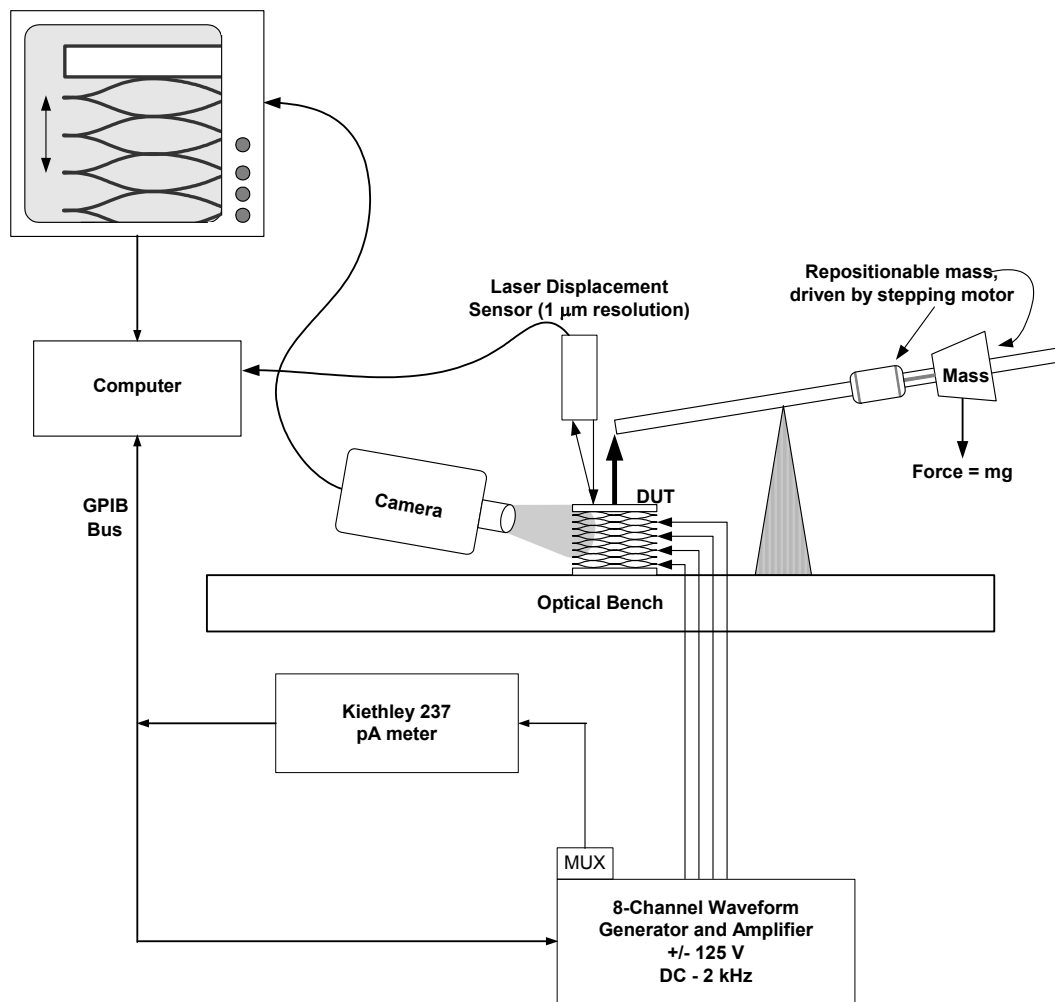


Figure 51. Schematic of the PolyMEMS Test Station.

4.0 Results and Discussion

4.1 1st and 2nd Generation Devices

The fabrication evolved through two generations of device design, shown in Figures 52 and 53. All devices used the linear unit cell. Generation 1 consisted of simple structures that were assembled by hand. The unit cells tended to be large: $\sim 2 - 10$ mm wide. Generation 2 consisted of devices with the integrated adhesive which were designed for the automatic assembly using folding. Gen. 2 devices had smaller unit cells, designed for larger forces. One mask set was made for 1, 2 and 3 layer arrays. The second mask set was made for 13 layer arrays.

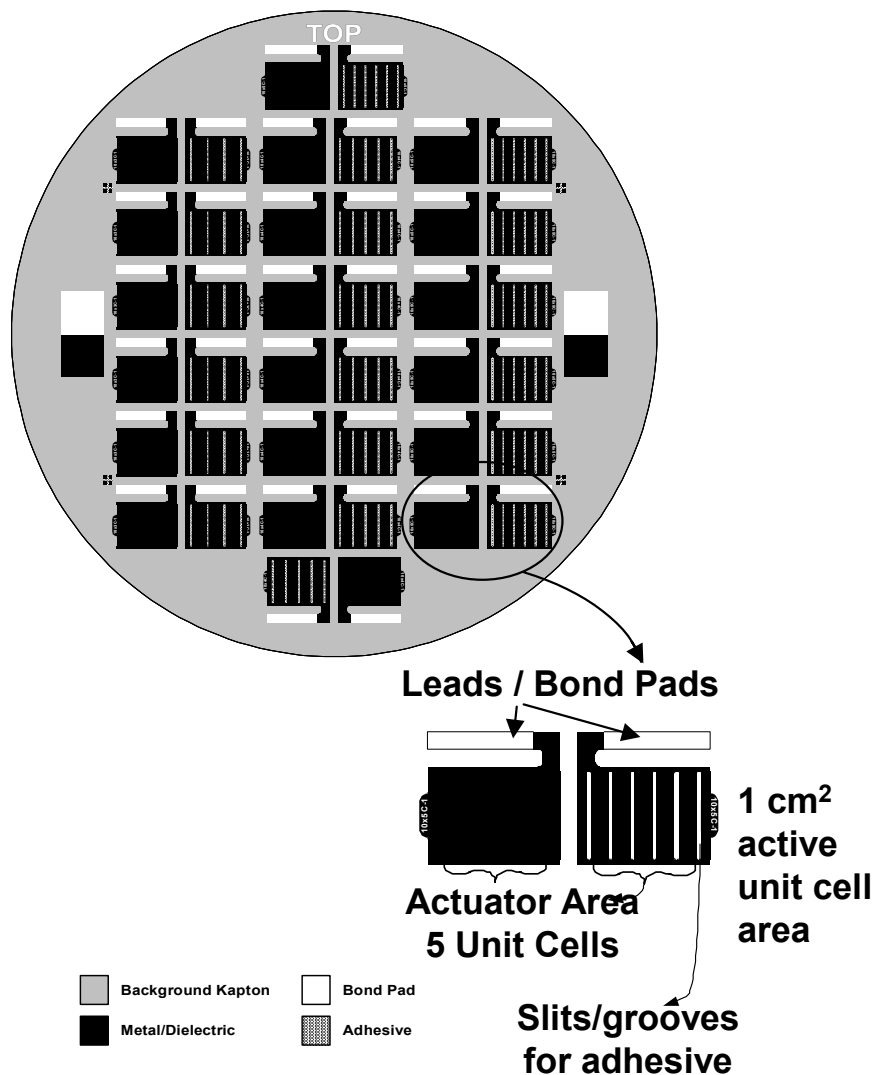


Figure 52. Generation 1 mask layout.

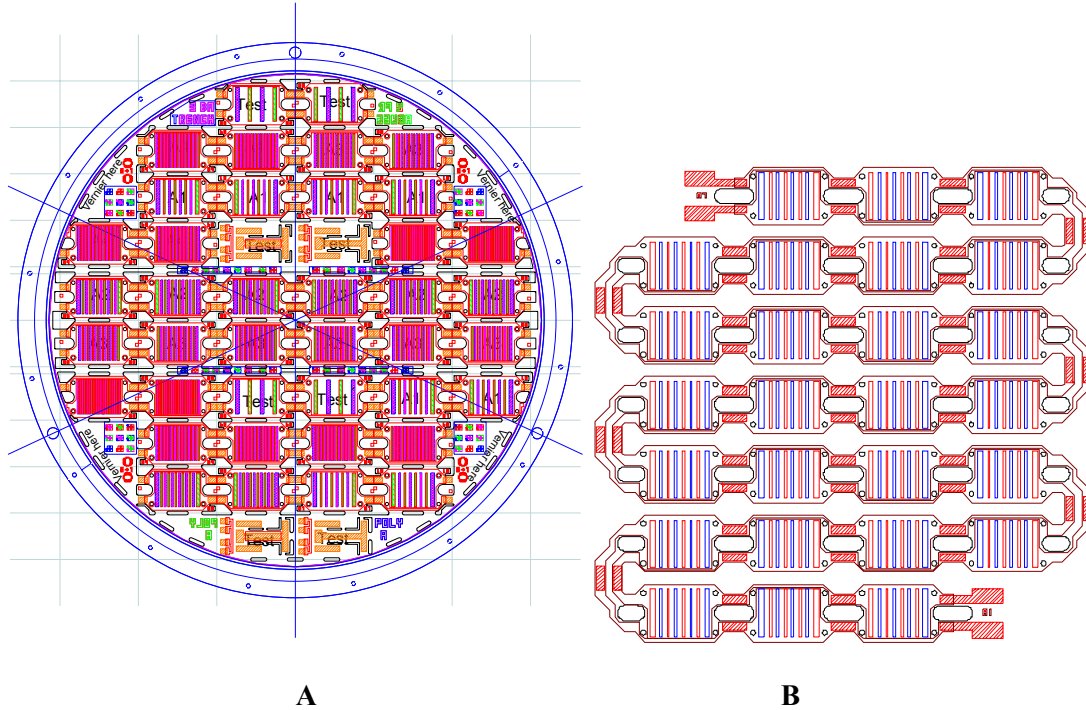


Figure 53. A. An early Generation 2 mask layout, containing 1, 2, and 3-layer arrays. B. Later Generation 2 layout of the 13-layer array, shown as it is after cutting the structure out of the wafer.

4.2 Actuation Test Results

Figure 54 shows test results from some of the early Generation 1 actuators. The earliest actuators worked poorly, having pull-in voltages ~ 100 V higher than predicted. Improvements in the assembly process yielded actuators with pull-in voltages that were only 20-30 V too high, but the slope of V_{PI} vs. the external force paralleled the theoretical prediction. Deformation is the most probable reason for the disagreement between theory and experiment. Because the early devices used large unit cells, small deformations at the cell edges were only a small perturbation to the overall shape of the unit cell. The deformations, therefore, exerted less of a spring force, and the pull-in tended to be relatively sharp. As we migrated to smaller unit cells, we typically observed a soft pull-in, as seen in Figure 55. Because these cells were smaller, the small deformation area near the laser cuts became a more significant fraction of the total unit cell area. The deformation, therefore, had a more noticeable effect. More careful alignment and assembly resulted in improvements, sometimes to a stepwise pull-in (Figure 56) and sometimes to the desired, sharp pull-in (Figure 57). More often than not, the pull-in was soft or stepwise, rather than sharp, and pull-in voltages were higher than predicted (Figure 58). Hand assembly lacked the precision and repeatability that was needed to get consistent results. This was one motivation for the Generation 2 approach.

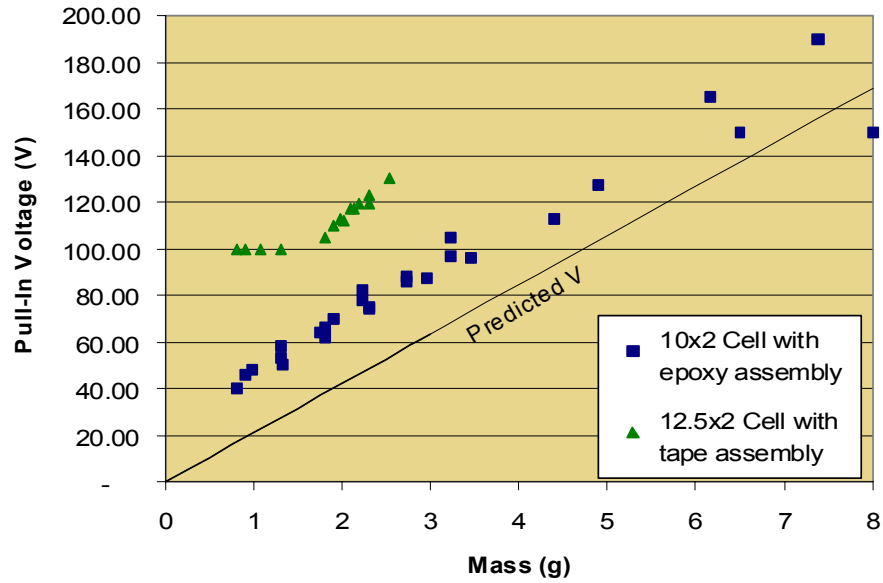


Figure 54. Pull-in voltages for early Generation 1 actuators.

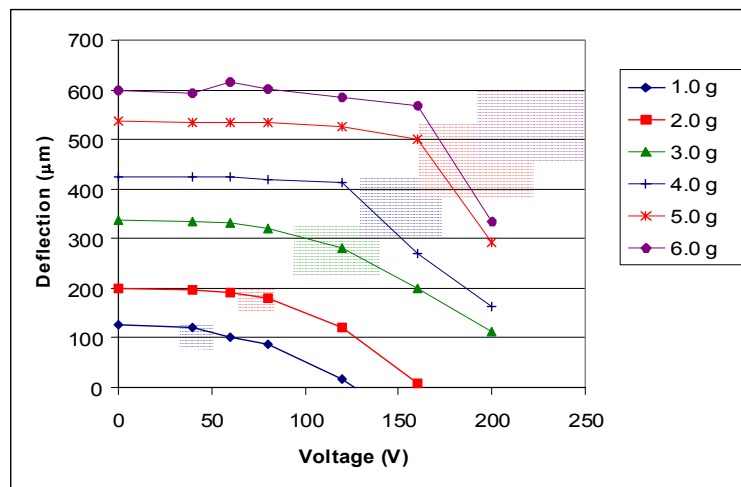


Figure 55. Displacement as a function of the applied voltage for various applied forces. Pull-in was soft, but was occurring at approximately the predicted value (the shaded areas). This soft pull-in was seen very commonly on Gen. 1 actuators.

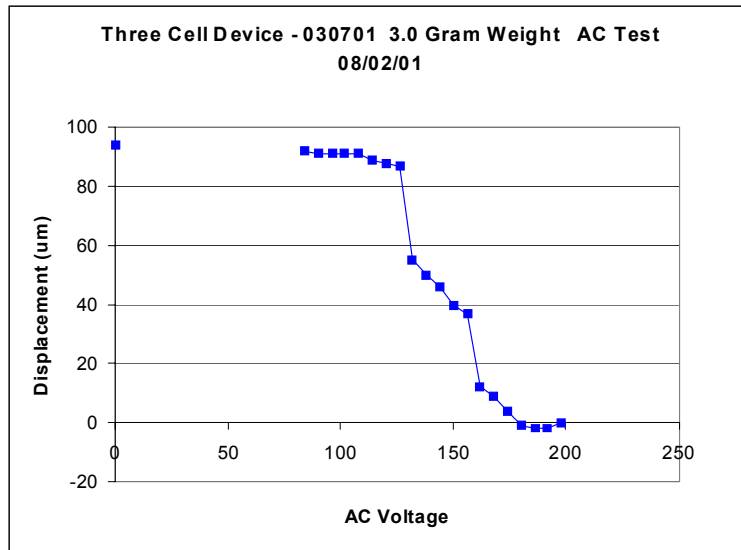


Figure 56. An example of stepwise pull-in. This actuator consisted of three unit cells lying side-by-side in a single layer. Each of the three cells had a fairly sharp pull-in, but each one at different voltages, producing the stepwise behavior. With careful viewing we could see the individual cells pulling in.

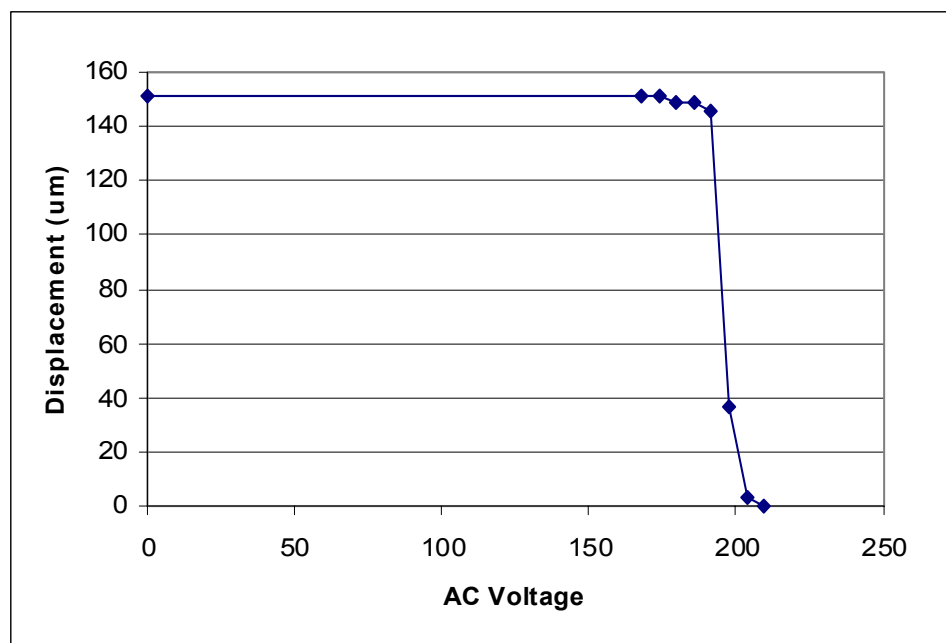


Figure 57. The desired sharp pull-in. Very careful alignment and assembly was required to get this behavior.

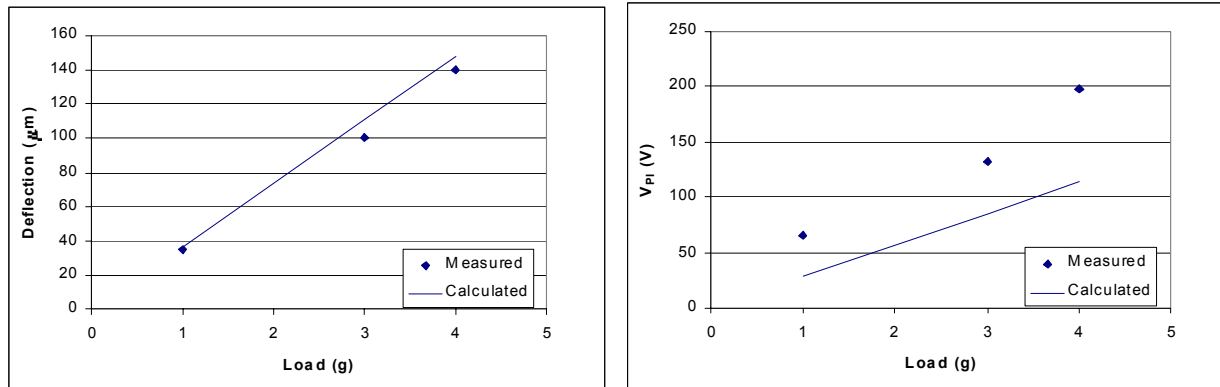


Figure 58. Typical force-displacement (left) and pull-in voltage vs. force (right) plots for small unit cells from Gen. 1. The purely mechanical behavior agreed well with the model predictions, but the pull-in voltage was larger than predicted. Hand assembly is not precise enough to avoid the deformations that lead to this.

Figure 59 shows typical data for Generation 2 actuators with a small number of layers. The pull-in was consistently better than Gen. 1 actuators, although still not as sharp as desired. Some pull-ins were slightly soft, some stepwise and some reasonably sharp. This implies that slight nonuniformities may still be present. The folds in this actuator may also contribute to the deformation force. Since the behavior is close to the expected behavior, it can be assumed that whatever deformation is present is relatively small. Another important indicator of this is seen in Figure 60. If the voltages in Figure 59, at which pull-in is complete, are plotted against the external force, the data matches well with theory. This demonstrates that, aside from the small deformations, the actuator is working as it is supposed to.

The PolyMEMS actuator concept is fully validated by this data.

Some of the measurements in Figure 60 are substantially below the calculated values. This is probably the difference between the model and the real structures, which obviously still have some deformity. The fact that pull-in (Fig. 59) typically started at a lower voltage than predicted suggests that the deformation was probably pulling the unit cell in rather than pushing it apart.

Generation 2 devices with 13 layers of unit cells were also fabricated, but these worked poorly. The force-displacement measurements (Figure 61) yielded a straight line, as you would expect. However, the slope was approximately a factor of 2 smaller than predicted. No pull-in was observed up to 220 V, even when no external force was applied. The folds (refer to Figures 49 and 53 – the folds are in the center of the bridges connecting the various links of the chain) were observed to exert a very strong deformation force on the actuator, pushing it open. Squeezing the actuator would cause it to close, but the folds pushed it open as soon as the actuator was released. If the actuator was squeezed and a voltage was applied, weak clamping

was observed, but even this did not hold well. Therefore, although the actuator concept is validated, there are some practical details that must still be worked out to reach a force of 1 N.

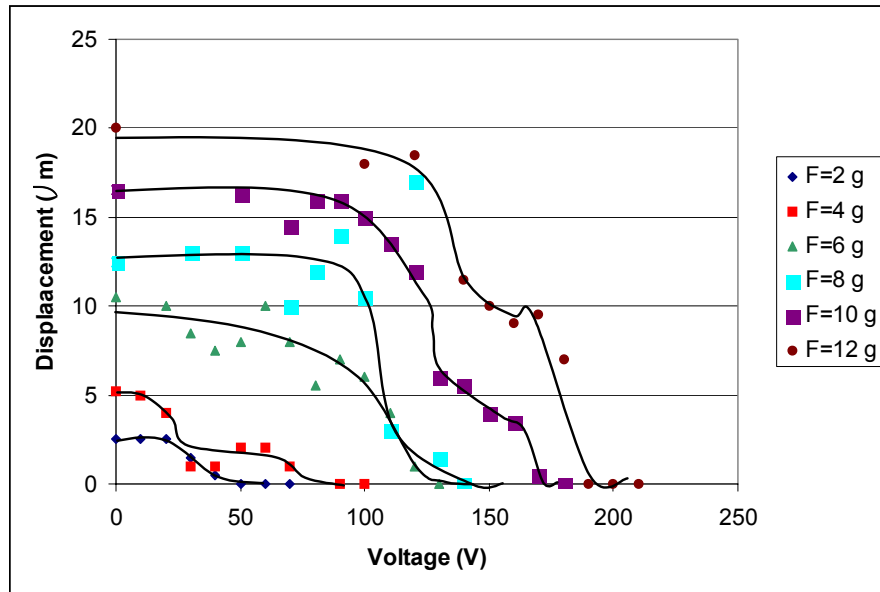


Figure 59. Typical data from a Generation 2 actuator with a small number of layers.

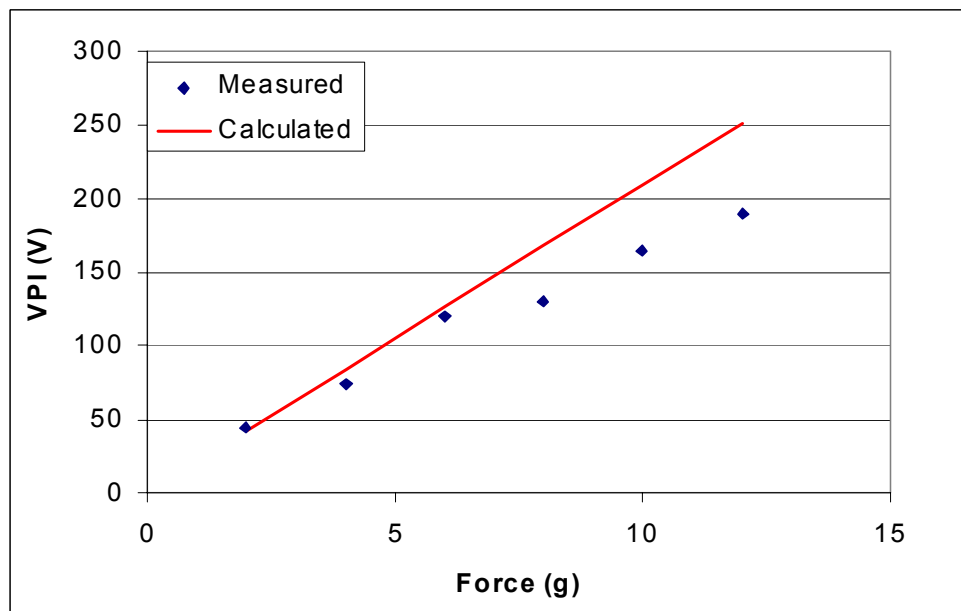


Figure 60. Pull-in voltage vs. applied force for the data in Fig. 59. The measured data agrees well with the predictions of the analytical model.

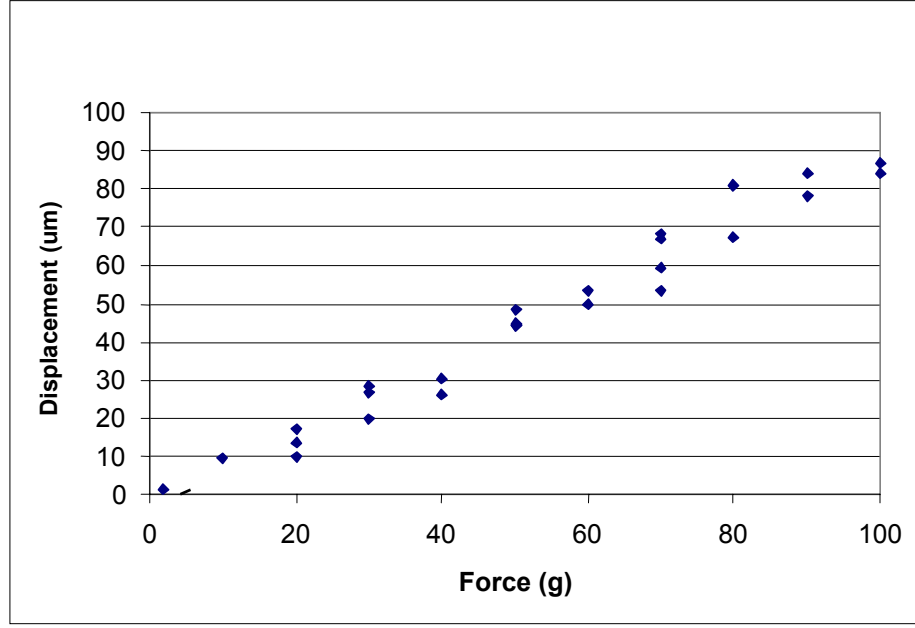


Figure 61. Force-displacement data from a 13-layer Gen. 2 actuator. The straight-line behavior is as expected, but the slope is approximately a factor of 2 off.

4.3 Power Consumption

The PolyMEMS actuator accomplishes its task using incredibly small amounts of power.

4.3.1 Energy and Efficiency

Efficiency, η , is defined as the ratio of the mechanical work performed to the electrical energy provided by the power source. The work for one unit cell is simply $W = F_{ext}\delta$. The electrical energy supplied comes from calculating

$$U_p = \oint dU = \oint VdQ, \quad (38)$$

where the integration is over the entire actuation cycle. Figure 11 (which is reproduced below for convenience) helps accomplish this. The cell starts out fully closed, an external force is applied, and the cell opens, following arrow 2, to the displacement labeled 3. This is all purely mechanical and no electrical energy is expended. At 3, the voltage is turned on and increased up to V_{PI} . No motion occurs during this voltage ramp, so the displacement and capacitance stay constant. Therefore,

$$U_1 = \frac{1}{C_o} \int QdQ = \frac{1}{2} C_o V_{PI}^2, \quad (39)$$

where C_o is the (very small) capacitance of the open cell. At pull-in, the force and displacement snap shut along the green curve indicated by arrow 4. Along this curve V is constant, so

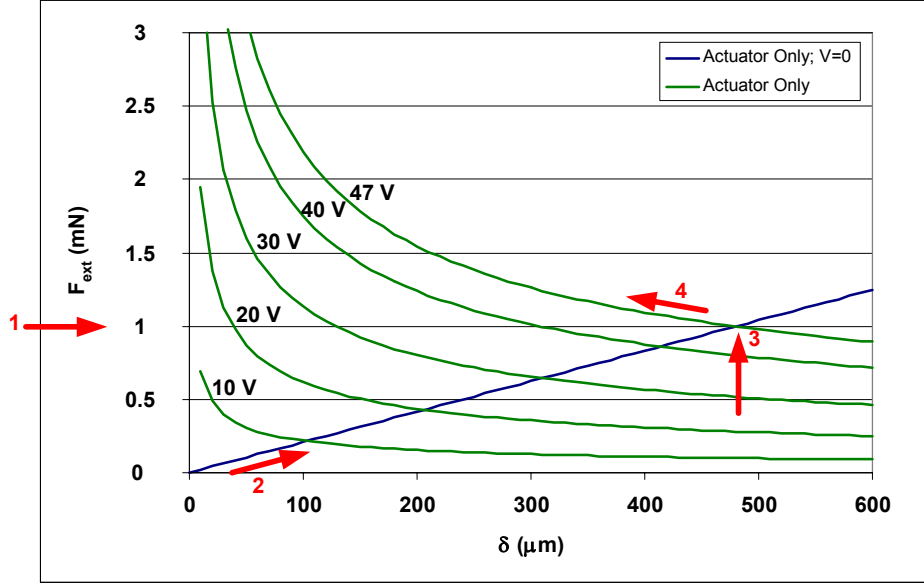


Figure 11. Force versus displacement from equations 5 and 10.

$$U_2 = V_{PI}^2 \int_2 dC = V_{PI}^2 (C - C_o). \quad (40)$$

where C is the capacitance of the fully closed unit cell. Therefore, the total energy delivered by the power supply to the capacitor is therefore,

$$U_P = U_1 + U_2 = CV_{PI}^2 - \frac{1}{2}C_oV_{PI}^2 \cong CV_{PI}^2. \quad (41)$$

since $C_o \ll C$.

From equations (3), (10) and (11) for the linear unit cell we can calculate the mechanical energy along path 4 as

$$W_4 = \int_{\delta}^0 F_{actuator} d\delta = \frac{2}{3} CV_{PI}^2 \quad (42)$$

However, this is not the same as the work done on the external load. The external load is a constant force F_{ext} , so the work done to it is simply

$$W_4' = \int_{\delta}^0 F_{ext} d\delta = \frac{1}{3} CV_{PI}^2 \quad (43)$$

Therefore the efficiency of the linear unit cell is

$$\eta_{linear} = \frac{W_4'}{U_P} = \frac{1}{3}. \quad (44)$$

The actuator force that is needed to pull in the external force is constant at F_{ext} . However, as can be seen from equation (10) and Figure 11, the actuator force is increasing during pull-in. The difference between the actuator force and the external force causes the external load to accelerate during pull-in, generating kinetic energy. When pull-in is complete, all motion stops and the kinetic energy is lost as heat. Theoretically, the available efficiency could be as large as $W_4/U_P=2/3$. To reach this, the voltage would have to be ramped down as the unit cell pulled in. In reality, this is not likely to be implemented. The feedback and circuitry required to do it would probably cost as much (in energy) as would be gained, so the scheme would not be effective.

The circular unit cell is an interesting comparison. This cell pulls in adiabatically. That is, the force of the unit cell is equal to F_{ext} all along path 4 in Figure 18. Therefore, no kinetic energy is generated. Using the equations for the circular cell, we can calculate the work and efficiency as

$$W_4 = F_{ext} \int_{\delta}^0 d\delta = CV_{PI}^2 \quad (45)$$

and

$$\eta_{circular} = \frac{W_4}{U_P} = 1. \quad (46)$$

The circular unit cell is the ideal shape. In reality, of course, neither of these efficiencies would be achieved. The applied voltage will always be at least a little larger than V_{PI} , and other imperfections will result in energy loss (e.g., leakage current), so these equations only provide an upper bound.

4.3.2 Power Consumption Estimate

Regardless of the unit cell, the power consumption is incredibly small. Consider, for example, a 1 cm^2 layer of unit cells with a $1 \text{ }\mu\text{m}$ thick PMGI dielectric ($\epsilon=3$) on each surface, so that $C=1.3 \text{ nF}$. For a multilayer actuator, this must be multiplied by the number of layers. If we assume it is operating at a maximum load, and was designed to pull the maximum load at $V_{PI}=200 \text{ V}$, and if it is operating continuously at $f \sim 1 \text{ Hz}$, then the power output of the battery is only

$$P = CV^2 f \approx 50 \mu W .$$

Energy is expended in two other parts of the actuator system. First, there are leakage currents in the capacitor. When the cell is open, these are negligible. When the cell is snapped closed, the current density is very small, on the order of 10 nA/cm^2 . Therefore, I^2R power dissipation is on the order of $2 \text{ }\mu\text{W}$ for a 1 cm^2 layer. Second, if the actuator is powered by a battery (a likely scenario) there will be a power and control circuit that dissipates some amount of power. Figure 62 shows the circuit we used. While this circuit is by no means optimized, it is representative. The DC-DC converter, which boosts the battery voltage up to the operating voltage of the actuator, consumes the most power. In our circuit, the DC-DC converter used $\sim 80 \text{ }\mu\text{W}$ for the same operating conditions as used in the other estimates. The power consumption of the converter is a function of the load that it is powering, so its power consumption will increase in proportion to the number of layers of the actuator. While the actuator uses power only while it is moving, the converter uses power whenever the voltage is applied, even if the actuator is not moving (for example, if the actuator is clamped shut, or if the applied voltage is less than the pull-in voltage). Therefore, the worst case power consumption for a single layer is $\sim 130 \text{ }\mu\text{W}$. A realistic actuator may need 100-200 layers to achieve large displacements.

Therefore, the power consumption for a complete actuator, operating continuously at maximum load, will only be on the order of 25 mW!

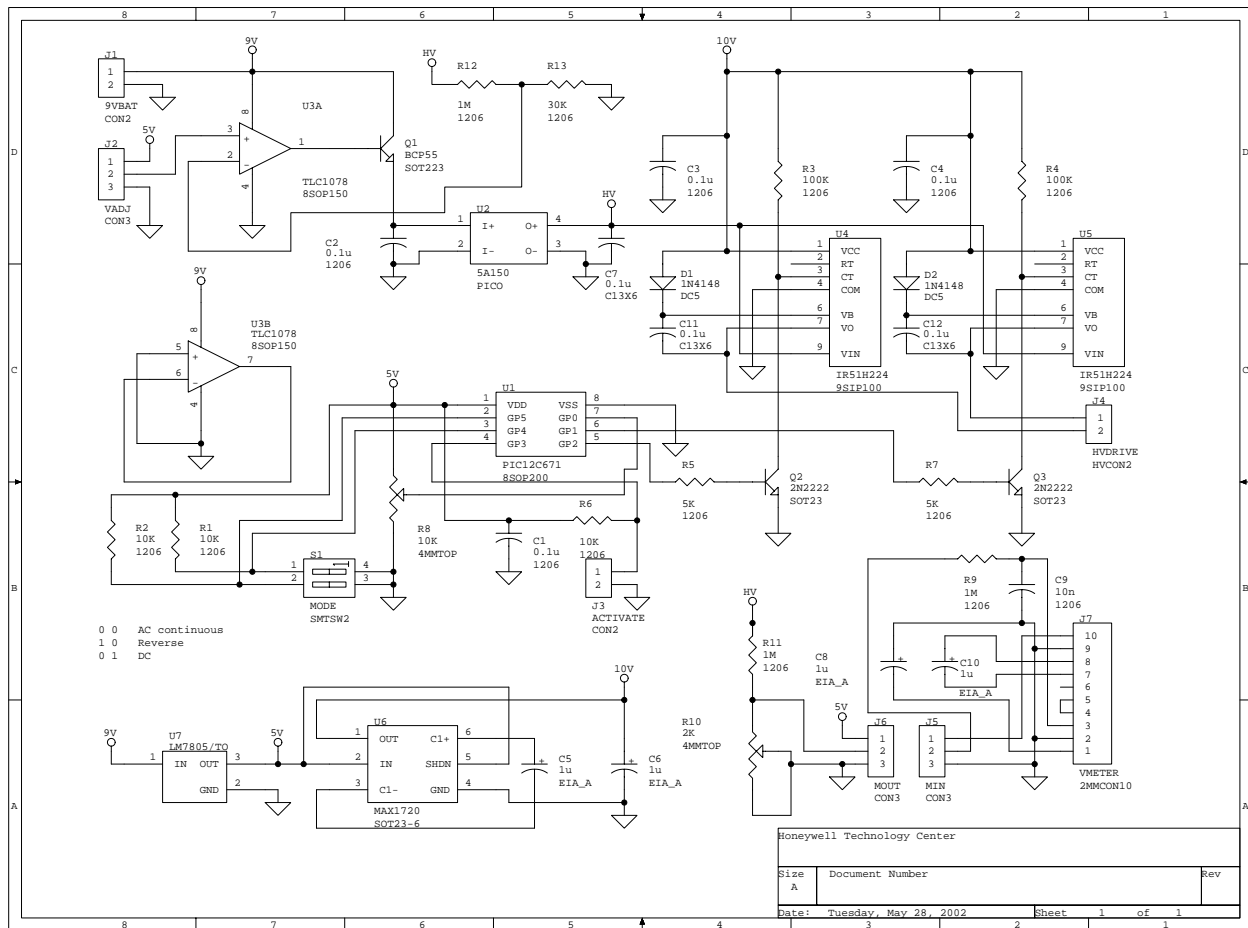


Figure 62. A representative control circuit for powering a PolyMEMS actuator from a battery. The DC-DC converter (lower left corner) uses the most power in this circuit.

5.0 Conclusions

- **The PolyMEMS Actuator Concept was validated.** When assembled properly, measurements of force, displacement and pull-in voltage are in agreement with the theoretical predictions. Although we did not reach the program goals of 1 N/cm^2 with 3 mm displacement, there is no reason why this cannot be achieved.
- **Further work is needed on assembly.** Assembly of individual layers must be done carefully in order to get theoretical performance, since small deformations obviously degraded performance. Assembly of multiple layers requires routing of power to the various layers. We used a folding procedure to accomplish this, but the folds introduced a strong, unwanted, internal force in the actuator. This must be eliminated in order to reach large forces and displacements, such as 1 N/cm^2 with 3 mm displacement.

- **The analytical model worked extremely well both as a design tool and an analysis tool.** The model could be modified with relative ease, so that many different situations could be studied. While finite element modeling is a powerful tool, the analytical model was shown to be more versatile for practical use.
- **The PolyMEMS Actuator is efficient, and uses very low power.** An actuator operating at full power should only consume ~25 mW of power. This includes the power used by the ancillary circuitry. These low values make the actuator very attractive for applications where power is limited, such as autonomous robotics or space applications.
- **A circular unit cell has potential for reducing assembly problems and reducing power consumption even further.** The circular cell can simultaneously achieve large force and displacement without having to stack large numbers of layers on top of each other. Therefore, the assembly problems caused by stacking will be reduced or eliminated.
- **Fabrication should be done on a flexible printed circuit line.** We fabricated our actuators on 6" "wafers," but a better approach would be to use a flexible printed circuit fabrication line. Dedicated chemical baths, etc. would need to be set up in order to avoid contamination of copper plating baths.

6.0 Recommendations

The conclusions point to four areas that should be explored further. The first three deal with design, fabrication and assembly: the circular unit cell should receive serious attention, the assembly of multiple layers requires further work, and fabrication should be done on a flex circuit line.

The final recommendation is an application of PolyMEMS actuators. Figure 63 illustrates the strong similarity between PolyMEMS actuators and muscle tissue. Muscle tissue is an array of sarcomere "unit cells." Many sarcomeres are arrayed side by side in a plane, to achieve large forces. These planes of cells are stacked end to end to generate large displacements. The PolyMEMS actuator does the same. Muscles generate force only by contracting. PolyMEMS actuators do the same. Both muscles and PolyMEMS, therefore, require antagonistic pairs to achieve bidirectional motion. Muscles are very energy efficient since their power source must be carried with them. PolyMEMS actuators are not required to carry a power source. However, if a source of unlimited power is available (e.g., by plugging in to a wall outlet) then there are plenty of existing actuators that could be used on a given application. However, if the power source must be carried by the actuator, then an extremely efficient actuator is required. PolyMEMS actuators fit this requirement.

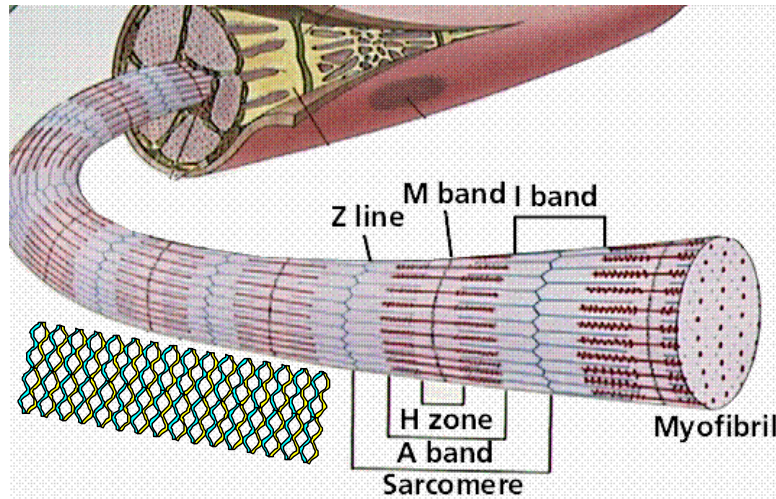


Figure 63. An artists rendition of muscle myofibril, an array “unit cells” configured side by side to generate large forces, and stacked end to end to generate large displacements.

Biomimetic robotics derive their size, shape, and modes of operation, at least in part, by copying from biological creatures. One example, the “RoboLobster” shown in Figure 64, under development by Dr. Joseph Ayers of Northeastern University, provides an excellent means of comparison between PolyMEMS artificial muscles and other technologies. Table 1 compares many different artificial muscle technologies with each other and with the requirements for “lobster-sized” biomimetic robots. The two columns on the right are virtually never seen in comparisons of different actuators, but they are critical for autonomous vehicles such as a robot. An autonomous robot must carry all of its power (usually batteries) and all of its power distribution and control circuitry along with it. The table clearly shows that few technologies meet even two of the four requirements, whereas PolyMEMS meets all four.

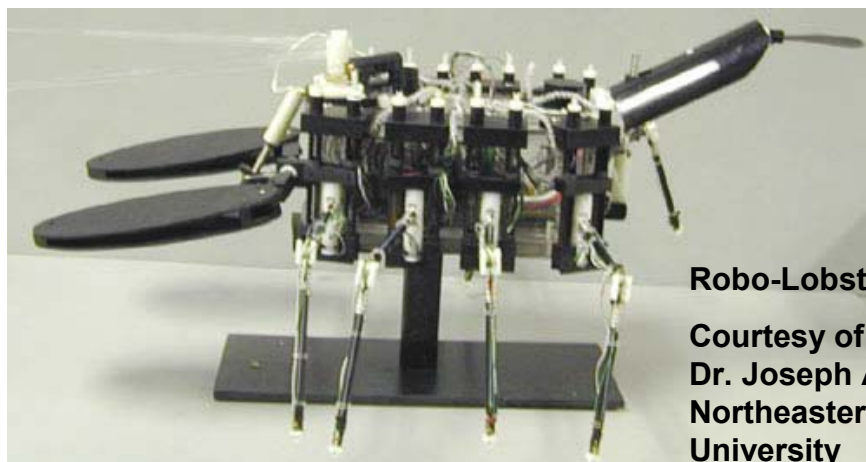


Figure 64. The Robolobster of Northeastern University.

Table 1. A comparison of artificial muscle requirements for biomimetic robots with the various available technologies. PolyMEMS is the only technology that can meet all requirements.

Technology	Force (N)	Displacement (mm)	Size/Weight of Ancillary Components	Energy Cost of Ancillary Components
Desired	Moderate	Moderate	Low	Low
Electromagnetic	Moderate	High	Moderate	Moderate
Hydraulic	High	High	High	Moderate
Pneumatic	High	High	High	Moderate
Shape Memory Alloy	Moderate	Moderate	Moderate	Moderate
Electrostrictive	Moderate	Low	Moderate	Moderate
Piezoelectric	High	Low	Moderate	Moderate
Magnetostrictive	Moderate	Low	High	High
Contractile Polymer	Moderate	Low	Moderate	Moderate
Single Crystal PZN:PT	High	Low	Moderate	Moderate
PolyMEMS Artificial Muscle (Proposed)	Moderate	Moderate	Low	Low

As an example, consider the requirements of the Robolobster. A maximum force of ~ 10 N, with a strain of 3-5% and total displacement of ~ 2 mm is needed. Based on our analytical model, Figure 65 shows that this is possible if the Kapton thickness is increased to ~ 75 μm (3 mils). The Robolobster uses TiNi shape memory alloys (SMAs) as muscles. Current running through the TiNi wires heats them up, causing them to change length. Six muscles are needed for each of the eight legs. Roughly half of them are in use at any one moment. Even so, approximately 80 W of power are consumed. Robolobster can operate only in water because 1) water cooling of the SMAs is needed to prevent melting, and 2) the buoyancy in the water is needed to be able to lift the heavy batteries. The maximum mission life of Robolobster is ~ 50 minutes. By comparison, a PolyMEMS actuator designed for this application (1 cm^2 area, 156 layers, with a 1 μm thick PVdF dielectric, at 200 V, operating at 2 Hz or less) requires ≤ 14 mW of power. With half of the 48 muscles operating at one time, the total power consumed is ~ 340 mW. If the control circuitry consumes twice as much power as the actuator, **the total power requirement is only ~ 1 W!** Therefore, a factor of 80X is gained simply by switching actuators. If we assumed a 1 kg Li-ion battery, which has an energy density of 100-150 Whr/kg (this is substantially smaller than the battery load currently used), the mission life would be 100-150 hrs (4-6 days!) operating continuously. If operation is stopped for part of the mission – for example, for surveillance, chemical monitoring, etc. – the mission would be even longer. The smaller battery load allows an increased payload, or smaller actuators (which require less power). In addition, PolyMEMS muscles do not need cooling, so the robot could operate on land.

PolyMEMS artificial muscles could be an enabling technology that makes biomimetic robots practical.

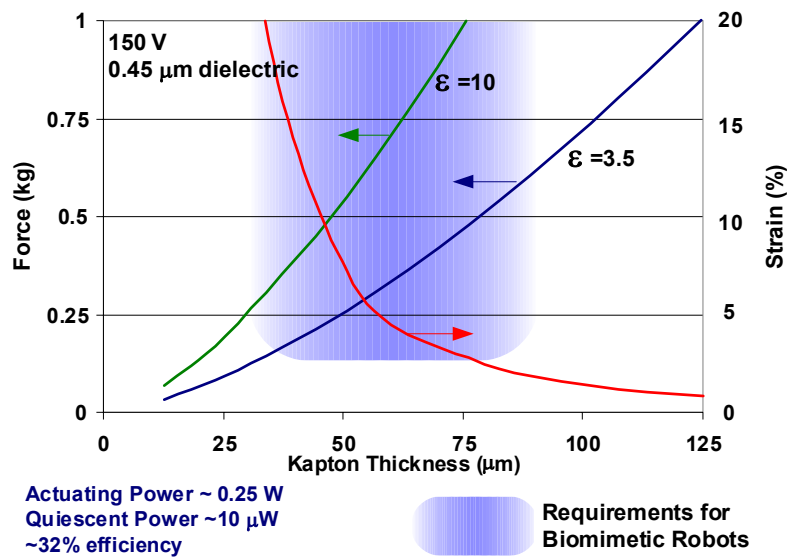


Figure 65. Analytical model calculations show that the increased force required for a Robolobster robot can be achieved in a PolyMEMS actuator if the Kapton thickness is increased to ~ 75 mm.

7.0 Publications

Robert Horning and Burgess Johnson, "Polymer-Based MEMS Actuators for Biomimetics." Published in *The Proceedings of Neurotechnology for Biomimetic Robots*, Nahant, MA, 14-16 May 2000. MIT Press. In press.

8.0 Patents

U.S. Patent #6,184,608. "Polymer Microactuator Array with Macroscopic Force and Displacement." Cleopatra Cabuz, Robert Horning, William Herb. Issued 6 Feb. 2001.

U.S. Patent #6,255,758. "Polymer Microactuator Array with Macroscopic Force and Displacement." Cleopatra Cabuz, Robert Horning, William Herb. Issued 3 July 2001.

U.S. Patent #6,411,013. "Microactuator Array with Integrally Formed Package." Robert Horning. Issued 25 June 2002. (Note: This patent was conceived prior to the award of the PolyMEMS contract, and was not reduced to practice under the contract. It remains Honeywell intellectual property.)

U.S. Patent #6,404,099. "MEMS Actuator with Lower Power Consumption and Lower Cost Simplified Fabrication." Robert Horning and Burgess Johnson. Issued 11 June 2002.